Inferring the Magnetization effect in high density CCRF Discharges- an Electrical Approach

By

JOSHI JAY KIRTIKUMAR

ENGG06201504005

Institute for Plasma Research, Gandhinagar

A thesis submitted to the

Board of Studies in Engineering Sciences

In partial fulfillment of requirements

For the Degree of

DOCTOR OF PHILOSOPHY

of

HOMI BHABHA NATIONAL INSTITUTE

Jan, 2020

Homi Bhabha National Institute

Recommendations of the Viva Voce Board

As members of the Viva Voce Board, we certify that we have read the dissertation prepared by JOSHI JAY KIRTIKUMAR entitled "Inferring the Magnetization effect in high density CCRF Discharges - an Electrical Approach" and recommend that it maybe accepted as fulfilling the dissertation requirement for the Degree of Doctor of Philosophy.

________________________________ Date: 15-07-2020

Chairman - Dr. P.K. Sharma

________________________________ Date: 15-07-2020

Guide/Convener - Dr. S.K. Karkari

________________________________ Date: 15/7/20

External Examiner - Prof. A.Ganguli

________________________________ Date: 15-07-2020

Member 1 - Dr. M. Bandyopadhyay

________________________________ Date: 15/07/2020

Member 2 - Dr. G. Ravi

________________________________ Date: 15/07/2020

Technical Advisor - Mr. Sunil Kumar

Final approval and acceptance of this dissertation is contingent upon the candidate's submission of the final copies of the dissertation to HBNI.

I hereby certify that I have read this dissertation prepared under my direction and recommend that it may be accepted as fulfilling the dissertation requirement.

Date: 15-07-2020

Place: Gandhinagar

Guide

STATEMENT BY AUTHOR

DECLARATION

I, hereby declare that the investigation presented in the thesis has been carried out by me. The work is original and has not been submitted earlier as a whole or in part for a degree/diploma at this or any other Institution / University.

Joshi Jay Kirtikumar

CERTIFICATION ON ACADEMIC INTEGRITY

1. I Joshi Jay Kirtikumar HBNI Enrolment No. ENGG06201504005 hereby undertake that, the Thesis titled "***Inferring the Magnetization effect in high density CCRF Discharges- an Electrical Approach***" is prepared by me and is the original work undertaken by me and free of any plagiarism. That the document has been duly checked through a plagiarism detection tool and the document is plagiarism free.

2. I am aware and undertake that if plagiarism is detected in my thesis at any stage in future, suitable penatlty will be imposed as per the applicable guidelines of the Institute/UGC.

Jay Joshi

Signature of Student

Endorsed by the thesis Supervisor:

(I certify that the work done by the Researcher is plagiarism free)

Signature

Name: Dr. S.K. Karkari

Designation: Asso. Professor - F

Department/Centre: Head, Magnetized Plasma Development Section

Name of CI/OCC: Institute for Plasma Research, Gandhinagar

List of Publications from this thesis

a) Journal Publications

1. **Joshi, J. K.**, Binwal, S., Karkari, S. K., & Kumar, S. (2018). Electron series resonance in a magnetized 13.56 MHz symmetric capacitive coupled discharge. Journal of Applied Physics, 123(11), 113301.

2. Binwal, S., **Joshi, J. K.**, Karkari, S. K., Kaw, P. K., & Nair, L. (2018). Passive inference of collision frequency in magnetized capacitive argon discharge. Physics of Plasmas, 25(3), 033506.

3. **Joshi, J. K.**, Binwal, S., Karkari, S. K., & Kumar, S. (2018). A hybrid probe system for quantifying plasma parameters in a 13.56 MHz capacitive coupled magnetized plasma. Review of Scientific Instruments, 89(11), 113503.

4. **Joshi, J. K.**, Karkari, S. K., & Kumar, S. (2019). Effect of Magnetization on Impedance Characteristics of a Capacitive Discharge Using Push-Pull Driven Cylindrical Electrodes. IEEE Transactions on Plasma Science, 47(12), 5291-5298.

b) Other Publications : Conferences/Symposium

1. **J.K. Joshi et al.**, RF power measurement by phase calibration technique for a magnetized CCP discharge - Poster presentation at National conference of Plasma Science Society of India (2017).

2. **J.K. Joshi et al.**, Impedance characteristics of a magnetized 13.56 MHz capacitive discharge - Poster presentation at the 45th EPS conference on plasma physics (2018).

3. **J.K. Joshi et al.**, Experimental investigation of Power Coupling by RF Antenna into Plasmas in Presence of Magnetized Ions - Poster presentation at the 27th IAEA Fusion Energy Conference (2018).

4. **J.K. Joshi et al.**, Axial characterization of a segmented cylindrical capacitively coupled plasma source by triple Langmuir probe - Poster presentation at National conference of Plasma Science Society of India (2017).

5. **Joshi, J.**, Binwal, S., Karkari, S., & Kumar, S. (2019). Observation of electron series resonance in transversely magnetized 13.56 MHz CCP discharge. Bulletin of the American Physical Society.

ACKNOWLEDGEMENTS

Foremost, I would like to show my gratitude to my thesis supervisor Dr. S.K. Karkari, without whose guidance, vision and encouragement at crucial times my research experience would have been unfulfilling. His most important contribution to my life however; will always be the lesson to remain humble to learn more.

I am also very much grateful to my technical advisor Mr. Sunil Kumar whose ever helpful nature with indomitable spirit will always motivate me. I would also like to acknowledge my doctoral committee members Dr. P.K. Sharma, Dr. Mainak Bandyopadhyay and Dr. G.Ravi for their timely insightful comments and suggestions on the progress and direction of the research.

This acknowledgement would be incomplete without the mention of my Lab mates Montu, Shikha, Avnish, Satadal, Dhrumil, Hasmukh and Yashshri Madam all of whom have broadened my horizons with perpetually interesting discussions about physics, engineering and life. I consider myself fortunate, to have all of you as my Lab mates. A special mention to my roommate and friend Montu; as he always stood with me as I grappled with research and personal problems over the past 4.5 years.

Mr. Vijay Patel of Workshop; Drafting Section, Electronics Section, Computer Section, IPR stores too many people to mention here; all have played their role in this work and deserves a worthy mention in this acknowledgement. My Batch mates Bhumi, Yogesh, Chinmoy, Arnab, Arun, Neeraj, Garima, Deepshikha, Mayank, Priti, Srimanta all have made my time at IPR full of happy memories. My interactions with Pawandeep, Swati and Chirag have been brief but still worthy of a mention here. A shout out to all my teachers who have made me the person, I am today. My final acknowledgement must go to my family; my parents, my brother Rushi his wife Payal and their kids Mohit and Reyansh for their unconditional love, support and moments of sheer joy. I ask for compassion, if I forgot to mention anyone who have contributed in any way to this work.

ABSTRACT

The past few decades have witnessed significant advancements in the field of Capacitively Coupled Radio-Frequency (CCRF) discharges due to wide range of applications in plasma processing industries, particularly in reactive ion etching. The process engineers are constantly envisioning various ways to tailor the performance of commercial CCRF sources and ways to externally control/quantify the plasma properties in these plasma reactors. The role of an external magnetic field to control the plasma properties is relatively a new concept; and is yet to be adequately explored. Additionally robust non-invasive diagnostic techniques are relentlessly researched and developed to efficiently monitor the plasma processes. These techniques are meant to not only monitor/control the plasma processing but are also driven towards reducing the plasma processing costs. The thesis is primarily motivated towards investigating the effect of external magnetic field on the performance of CCRF discharges; and inferring its characteristics by means of non-invasive electrical/impedance measurements that are external to the plasma environment. Two important aspects that has emerged from this study is the phenomena of electron series resonance (ESR) in magnetized plasma and magnetically enhanced power mode transitions (PMT) which apparently causes a shift in power coupling channels to the electron heating in the bulk from ion heating in the sheaths. These phenomena have been observed through detail analysis of calibrated RF power measurements in the devices. Additionally the role of ion mass on the nature of sheaths at the RF driven electrodes has been studied. The externally measured impedance measurements of the CCRF plasma source are also supported by direct measurements of plasma properties inside the bulk plasma with the help of a newly developed hybrid probe system comprising of an emissive and a double probe. The above mentioned results have been comprehended in two experimental systems with different electrode geometries and B-Field orientations each with different motivations;

1. Parallel plate setup: The parallel plate electrode configuration is devoted towards understanding the effect of transverse B-field on an industry relevant electrode con-

figuration in which flat substrates lying on the electrodes becomes part of the discharge circuit as well as the fundamental aspects of non-local heating in capacitive sheaths induced by the crossed electric and magnetic fields.

2. Cylindrical CCRF plasma setup: This has been developed with the objective to create an elongated plasma column. The role of axial B-field in a system with azimuthally closed $\vec{E} \times \vec{B}$ drift to sustain a long/uniform plasma column has been comprehended. Long plasma column in an axial magnetic field has been aimed for multi-disciplinary physics experiments in linear plasma device.

In conclusion, this experimental investigation backed up with theoretical models; reveals the intrinsic effects of introducing a B-Field in a CCRF plasma discharge. Moreover, this research also provides certain inputs to designers of magnetized plasma systems for the effective range of B-field to influence the plasma dynamics.

Contents

List of Figures

List of Tables

Chapter 1

Introduction

In the past few decades, plasma processing technologies are rapidly evolving to meet the growing requirement from the industries involved in manufacturing of solar photo-voltaic cells to bio-medical applications like plasma treatment of surgical equipments and food grains by low temperature plasmas. Capacitive Coupled Radio-Frequency (CCRF) discharges are extensively used in such processes. The CCRF plasma has also significance in laboratory plasma experiments which are generally operated at low working pressure [1]. In multi-billion dollar semi-conductor industries, efficient plasma tools are in a high demand for achieving greater production rate with very high precision. Independent controlling of plasma parameters such as plasma density, electron temperature and substrate voltage is a key requirement particularly in industrial processing application. Besides fundamental understanding of a CCRF discharge can help in developing advanced plasma reactors with reliable control and scalability.

In a CCRF discharge, the electrons respond instantaneously to the time varying RF electric field/potential inside the bulk plasma, whereas positive ions respond only to the time-averaged DC potential inside the sheaths. Therefore, RF power is predominantly coupled to the plasma electrons, whereas the positive ions gain energy inside the sheaths. The sheath is a non-neutral region near the material surfaces having strong electric field. This electric field accelerates the positive ions from the sheath boundary towards the material electrode and on impacting the electrode surface it results in the atomic scale modification on the substrates. The CCRF discharge is therefore a very unique device for plasma processing, since the substrate itself is the part of the discharge circuit. The applied RF power is primarily coupled to the electrons inside the bulk and also under certain operating conditions a significant fraction of RF power can be coupled to the positive ions in the sheaths. It has been reported that the dominant power coupling in a given CCRF discharge can shift from electrons to positive ions as the RF power levels increases [2]. This shift in power coupling is directly linked to the change in electrical impedance of the discharge circuit. The power/impedance measurements performed externally is therefore helpful in quantifying the nature of the dominant power coupling mechanism taking place within a given discharge setup. This insightful information is necessary for the design optimization of a plasma reactor as well as for improving the discharge performance.

In CCRF plasma reactor, the plasma/process parameters are primarily controlled by varying the frequency and amplitude of the applied RF voltage and background pressure in the discharge chamber. A number of familiar techniques have been adopted in a CCRF discharge such as application of multiple RF frequency [3] and tailored voltage wave-form [4] etc for controlling the plasma parameters independently. One such method could be introduction of magnetic field to control the plasma parameter. Some of the effects of magnetic field are well-known such as confinement of the particles to increase the discharge efficiency; enhanced power deposition, introduction of different charge particle drifts etc. However, application of an external magnetic field to control the plasma properties such as ion flux/energy or electron temperature T_e is relatively a new concept that hasn't been adequately explored. Recent works by You.et.al [5] [6] and Sharma et.al [7] have proposed magnetic field based control of a CCRF plasma with some experimental and simulation results. However, extensive experimental work on the magnetized CCRF plasma discharge has not been performed to validate the effectiveness of B-field as a control mechanism.

Electrical impedance measurement is a useful non-intrusive technique to characterize an RF discharge. In this technique the external measurement of RF Voltage, Current and Phase can provide useful information about the discharge properties. This technique is routinely used in semiconductor industries for monitoring the plasma tool health, end point detection and predicting process anomaly [8]. Electrical measurements with feedback techniques can be used for parametric changes during plasma processing [9]. The non-invasive nature of this technique is particularly useful for application in magnetized CCRF discharge.

This thesis is motivated towards comprehending the behavior of magnetized CCRF discharge by means of inferring the electrical characteristics through non-invasive electrical measurements. A brief overview of RF plasma is presented in the following section.

1.1 Plasma

1.1.1 Plasma State

The plasma is a state of matter which is simply an ionized gas comprising of electrons, positive and/or negative ions, neutral atoms and molecules that becomes strongly electrically conductive such that the long-range electric/magnetic forces dominates its behaviour [10]. In presence of an external electric field, the motion of the charge particles constitutes a net current flowing through the plasma. The internal currents can also generate magnetic field, which can twist and turn the orbits/ trajectories of other charge particle. The plasma as a whole exhibits collective behaviour due to which the motion of the charge particles inside the plasma is governed by long range electromagnetic forces due to collection of other charge species present inside the plasma. Therefore, the plasma self-organizes against externally imposed electric potential by shielding it over a tiny distance as compared to the plasma dimension. Debye length, one of the characteristic length inside plasma; is the distance over which the potential due to thermal fluctuation of charge species inside is screened. In plasma medium charge particles namely electrons and positive ions are characterized by their natural frequency of oscillation/time scales $\omega_{pe} = (\frac{n_e e^2}{m_e \epsilon_0})^{1/2}$ – electron plasma frequency and $\omega_{pi} = (\frac{n_i e^2}{m_i \epsilon_0})^{1/2}$ – ion plasma frequency which are dependent of their respective mass and plasma density.

1.1.2 Dielectric Property of Plasma

The plasma is a dispersive medium and hence, its response to a RF potential fluctuation varies as a function of the frequency. This is due to the fact that the charge particles inside plasma can be polarized as the charge particles namely electrons and ions react at a different rate to the applied potential. Therefore the dynamics of charges inside plasma will be dependent on the frequency of the applied field. The intrinsic electric field so generated can counter the applied electric field. This behavior of plasma could be understood by considering a dielectric constant of the plasma as a function of the frequency $\epsilon_p(\omega)$.

Consider a uniform plasma driven by a small RF electric field $\tilde{E_x}(t) = \tilde{E_x} cos\omega t = Re\tilde{E_x}e^{j\omega t}$. For a case of non-responsive ions ($\omega_{rf} > \omega_{pi}$); and assuming all quantities have a sinusoidal variation; the force equation on electrons is written as [11];

$$m\frac{\partial u_x}{\partial t} = -eE_x - m\nu u_x \tag{1.1}$$

where ν is the electron collision frequency

Substituting $E_x = \tilde{E_x} cos\omega t$ in Eq. 1.1 and solving for the velocity u_x; we get

$$\tilde{u_x} = -\frac{e}{m}\frac{1}{(j\omega + \nu)}\tilde{E_x} \tag{1.2}$$

Now, the total current through a plasma dielectric is given from the maxwell's equation;

i.e.

$$J_{tx} = \epsilon_0 \frac{\partial E_x}{\partial t} + J_x \tag{1.3}$$

Where, J_x is due to motion of electrons; while $\epsilon_0 \frac{\partial E_x}{\partial t}$ corresponds to the displacement current.

In the cold plasma approximation we have; $J_x = -en_0\tilde{u_x}$ and we also have $\frac{\partial E_x}{\partial t} = Re j\omega\tilde{E}_x cos\omega t$ Therefore, the total J_t is

$$\tilde{J}_{tx} = j\omega\epsilon_0\tilde{E}_x - en_0\tilde{u_x} \tag{1.4}$$

Substituting u_x from Eq: 1.2 in Eq: 1.4 we get;

$$\tilde{J}_{tx} = j\omega\epsilon_0[1 - \frac{\omega_{pe}^2}{\omega(\omega - j\nu)}] = j\omega\epsilon_p\tilde{E}_x \tag{1.5}$$

Where; ϵ_p is the complex plasma dielectric given by;

$$\epsilon_p = \epsilon_0[1 - \frac{\omega_{pe}^2}{\omega(\omega - j\nu)}] \tag{1.6}$$

This equation could also be written in terms of the plasma conductivity as

$$\tilde{J}_{tx} = (\sigma_p + j\omega\epsilon_0)\tilde{E}_x \tag{1.7}$$

where RF conductivity of plasma is given as;

$$\sigma_p = \frac{\epsilon_0{\omega_{pe}}^2}{j\omega + \nu} \tag{1.8}$$

1.2 RF plasma discharges

Radio frequency plasmas are often created using generators operating at harmonics of 13.56 MHz, which are specially allocated RF frequency for scientific and industrial use.

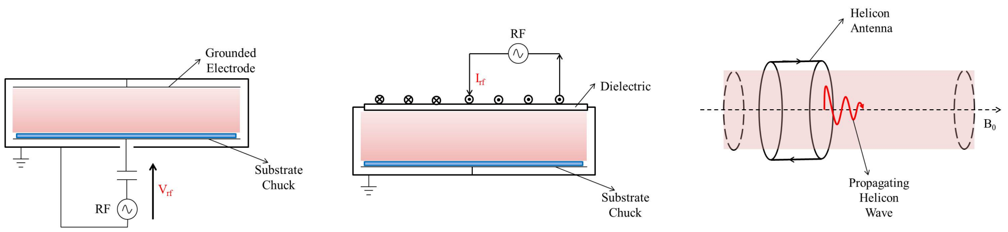

(a) Capacitive plasma (b) Inductive plasma (c) Wave-heated plasma

Figure 1.1: Types of RF discharges

For many industrially relevant plasma systems the 13.56 MHz drive frequency falls between the ion and electron plasma frequencies ($\omega_{pi} < \omega_{rf} << \omega_{pe}$); hence the plasma electrons can respond instantly to the RF potentials/fields, while the heavier positive ions respond to the time averaged potentials, which are commonly referred to as the "DC potentials".

There are primarily three different categories in which the RF discharge can be classified; a) Capacitive coupled b) Inductive coupled and c) Wave-heated type. In Capacitive RF discharge; plasma is created by applying sinusoidal RF voltages across a set of electrodes as shown in Fig 1.1a. In the inductive type, the plasma is created by a transformer action. The RF power to the discharge is coupled through electromagnetic induction from a closed loop coil/antenna separated from plasma by a dielectric as shown in Fig 1.1b. In a wave heated plasma, the electro-magnetic waves are excited to deliver RF power by closed looped antenna systems in presence of magnetic fields as seen in Fig 1.1c. The different mechanism of creating discharges leads to unique characteristics of the plasma and therefore each are used as per process requirements. The primary objective of the present study is focused on the capacitively coupled RF plasmas; as it will be introduced in detail in the next section.

1.2.1 Introduction to CCRF plasma discharges

Fig 1.2 shows a typical capacitively coupled plasma setup. The discharge is sustained by passing RF current between the two electrodes inside a vacuum chamber. Conventionally, one of the electrodes is kept grounded; while the RF power is provided to the powered electrode. An impedance matching unit is required to achieve maximum transfer condition to the plasma load.

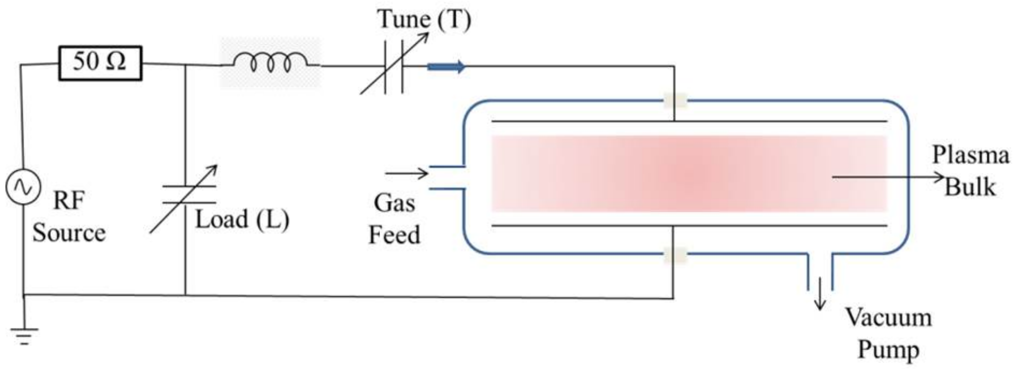

Figure 1.2: Schematic of a typical capacitively coupled plasma system

As the positive ions and electrons respond at different time scales in plasma; it leads to formation of plasma sheaths at both the electrodes to shield the excess loss of one type of charge species over the other; The quasi-neutral plasma region is maintained between the two sheaths at the opposing electrodes. The sheaths also shield the plasma from the external RF potential on the electrodes. Consequently, the sheath width (/shielding) is a function of the RF potential on the electrode that results in an oscillating sheath width s (t) over an average DC value. Over the RF cycle; the sheath electric field is unidirectional (pointing from plasma to electrodes) and hence a time averaged DC potential is developed in the sheaths.

The sheath electric field repels the plasma electrons; while accelerates the positive ions to the time averaged DC potentials developed in the sheaths. As mentioned earlier, the accelerated positive ions bombarding the electrode/substrate is the basis of plasma processing on the substrate. The discharge power ($P_{dis} = I_{dis}^2 R_{dis}$; I_{dis}- RF discharge current and R_{dis}- Total discharge Resistance) delivered to the capacitive discharge is dissipated in primarily two independent modes a) electron heating mode in the bulk plasma and b) the ion heating mode in the sheaths. Therefore, the total discharge resistance Rdis is made up of different dissipative processes occurring in sheaths (R_{sh}) and the bulk plasma (R_p)

each adding up to the total power dissipation i.e. $R_{dis} = R_p + R_{sh}$. In the coming sections, we will further refine the R_p and R_{sh} to include distinct dissipative processes. The two regions 1) RF sheaths and 2) Plasma Bulk are discussed separately in the later sections.

1.2.2 Sustenance of plasma in CCRF discharge

The primary mechanism for sustaining the discharge is through electron impact ionization by the energetic electrons excited by the RF potential applied to the discharge plates. For ionization of argon a 15.76 eV electron is needed. The ionization mean free path $\lambda_i = \frac{1}{n_g \sigma_i}$; where n_g-neutral gas density and σ_i- ionization cross-section determines the length at which the probability of ionizing collision is maximum. Thus λ_i is an important parameter to understand the different heating mechanisms briefly discussed below;

1) Sheath/Stochastic heating (Collision-less)

In a low pressure CCRF discharge, λ_i the ionization mean free path is almost comparable or even larger than the gap length - d ($\lambda_i > d$); As a result the ionizing collisions are rare within the plasma bulk leading to minimal collisional heating by RF excited electrons inside the plasma volume. Incidentally, it was found that the oscillating sheath plays a major role in heating the plasma electrons locally near the discharge plates [12]; hence the RF power is utilized in energizing the plasma electrons near the sheaths. These energetic electrons can then help in sustaining the plasma. The interactions of electrons with the oscillating RF sheath constitute a columbic collision; wherein the intense sheath electric field interacts with the plasma electrons.The power coupled to electrons in this mode is considered to be dissipated through a resistance R_{stoc}. Although the electron interacts with the sheaths in this mode, the power coupling helps sustain the plasma bulk.

The transfer of energy in this heating mode happens by accelerating the plasma electrons during the expanding phase of RF sheath. During the shrinking or collapsing phase, no energy being transferred from the RF to the electrons sheath. It has found with help of

Kinetic simulations that overall effect of this mechanism leads to a net gain of energy [13]. Simplest model to describe this mechanism is a hard wall model; which depicts the mechanisms with a ball bouncing elastically between two rigid moving walls [1] [14] [15]. Since, the electron interacts with the sheaths and not with particles in the plasma; this collisional heating is also known as collision-less heating or stochastic heating due to nature of interaction of electrons with sheaths.

Fully collision-less plasma models have been developed by Goedde et.al [12]; which showed that plasma with only collision-less heating would have pD < 10 mtorr.cm for a 13.56 MHz frequency discharge. Moreover, it is also known that the for operating pressure below 20 Pa in etching plasma; collision-less heating is the dominant mechanism for plasma sustenance [16]. Since in this study we operate the plasma at low pressures of 1.0 Pa (7.6 mTorr) and gap of 8.0 cm in parallel plate. It is considered to be the dominant heating mechanism.

2) Ohmic heating – (α mode) In the pressure regime where $\lambda_i < d$. The ionizing collisions occur in the bulk plasma and are the primary source of plasma heating. This is the heating mechanism seen in a DC discharge. This is called the ohmic heating as the collisional heating is equivalent to a joule heating of a resistor I^2R to sustain the plasma discharge. Since, the mechanism is dependent on the ionizing collisions occurring inside the bulk plasma it is associated to the first townsends co-efficient ($\alpha = 1/\lambda_i$; the inverse of the ionization mean free path) [11] and hence is also called α-mode of heating. Since, this is a collisional power transfer to electrons in the bulk; the power dissipation in this mode is through resistance R_p.

3) γ mode – (Secondary electron driven) At even higher pressures λ_i is comparable to the sheath width s ; when the RF power level is increased the time averaged DC voltage across the sheaths also increases leading to a secondary breakdown in the sheaths. This marks a transition from the α to the γ – mode of power coupling. Not only positive ions bombarding the electrode surface lead to secondary electron emission, but the ionization

inside the sheath itself can create electrons within the sheaths, which can gain acceleration in the sheath electric field and ionize the background gas while traversing through the bulk plasma. This mechanism then becomes the primary power coupling mechanism.As this process depends on second townsends co-efficient (γ - number of secondary electrons emitted from the electrode per positive ion bombardment) it is called γ -mode of heating [11]. The secondary electron emissions (γ) are always present in CCRF plasma discharge; even at low pressures. However their effect is only realized for higher pressure discharges; since at lower pressures they are lost from the system without any ionizing collisions.

The shift from α to the γ – mode can be visibly seen in the discharge as the plasma suddenly intensifies and shrinks in area [1]. The shrinking occurs as the RF generator cannot immediately supply the required current to sustain the higher current density across the whole electrode. The discharge covers the whole electrode again as RF power is increased further.

All the three modes discussed above couples RF power to sustain the plasma. The plasma self-organizes creating electron temperature T_e, a plasma potential V_p and a DC bias in the sheaths V_{dc} such that the plasma is at steady-state. The ions are accelerated in the time average DC (V_{dc}) field in the sheaths and hence a time-independent constant ion flux is lost from the plasma. Therefore, a part of power ($P_{ion} = I_{i,flux}V_{dc}$) is dissipated by the ions and delivered to the surface of electrodes. A resistor R_i accounts for this power dissipation such that $P_{ion} = I_{i,flux}V_{dc} = I_{dis}^2 R_i$. Apart from the power coupling to ions in the sheaths under the influence of V_{dc}; it is also possible for an electron to undergo a collision inside the sheaths; which is also a power dissipative mode through dissipative resistor $R_{ohm,sh}$. The electron collision inside the sheaths is typically ignored for low pressure plasma discharge considering collision-less sheaths and hence this power dissipation may also be ignored.

1.2.3 RF Sheaths at electrodes

The non-neutral sheaths is region which offers significant impedance to the flow of RF current through the bulk plasma. Electrons, the primarily conducting species in the plasma move into/out-of sheath with the change in differential-voltage between electrode and plasma. This lack of electrons in the sheaths leads to current continuity largely maintained by the displacement current. The sheath therefore resembles a capacitor with one side at the plasma potential and other side at the electrode potential. As seen before, a constant ion flux leaves plasma through the sheaths which corresponds to the conduction current in the sheaths; which is balanced by the loss of electrons from the plasma due to its temperature T_e. This electron loss from the plasma appears for a very short period in an RF cycle when the potential difference between the electrode and the plasma goes to zero. The current continuity through the sheaths could be better understood from an electrical analogy of the sheaths

Electrical analogy of the sheaths

As mentioned above, the dominant displacement current passes through the sheath capacitor C_{sh}; while the conduction current due to ion acceleration remains constant. This electrical analogy resembles a capacitor in parallel with constant current source. The sheath electric field repels the plasma electrons away from the electrode over most of the RF cycle. However, to balance the constant loss of positive ions to the electrode, an equivalent loss of electrons from the plasma must also take place. This is achieved by a momentary loss of electrons; when the RF potential on the electrode reaches to the plasma potential value i.e. Sheath vanishes. This mechanism is analogous to a forward bias diode allowing current conduction to one direction alone. Therefore, the equivalent circuit of two RF sheath is as shown in Fig 1.3. If the two electrodes are of same area, then the CCRF discharge is of a symmetric type; the oscillations in RF sheath width s (t) at the opposing electrodes are 180^0 out of phase. Hence, the combined sheath width of both the electrodes is independent of time. Consequently, in the analogy; combined sheath capac-

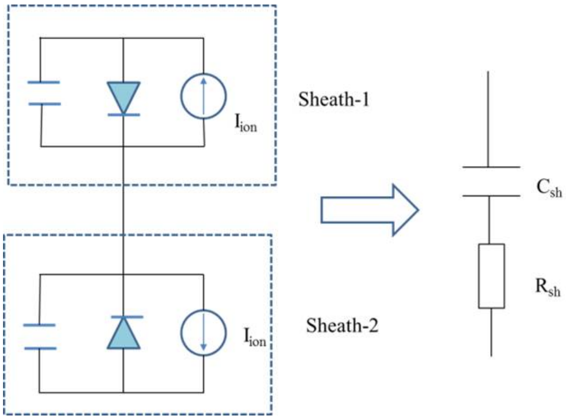

Figure 1.3: Electrical analogy for the sheath

itance of $C_{sh} = \epsilon_0 A/2s$ is used. Moreover, as discussed in the previous section; there are different power dissipative mechanisms in the sheaths; which correspond to a combined sheath resistance of $R_{sh} = R_i + R_{stoc} + R_{ohm,sh}$

1.2.4 Plasma Bulk

The quasi-neutral region of the discharge can be defined as Plasma. The plasma electrons constitute the RF current i.e. conduction current through the bulk plasma and dominates over the displacement current passing through the vacuum capacitance $C_0 = \epsilon_0 A/d$ of the plasma bulk. The dominant conduction current due to highly responsive electrons provides the Plasma heating via the electrons collision with the background neutrals. Plasma bulk could also be understood in terms of its electrical equivalent circuit.

Electrical analogy of bulk plasma

Since the plasma is a complex plasma dielectric $\epsilon_p(t)$ which has been shown by Eq:1.6;

$$\epsilon_p = \epsilon_0[1 - \frac{\omega_{pe}^2}{\omega(\omega - j\nu)}] \tag{1.9}$$

In a CCRF plasma $\omega << \omega_{pe}$ therefore from the Eq:1.9 the value of ϵ_p is negative. The reactive impedance provided by the plasma dielectric is therefore inductive (+ve reactance). This result can be arrived from Eq:1.9 by considering the dielectric for a plasma bulk of length d and cross-sectional area A; the plasma admittance Y_p can be calculated as follows [11];

$$Y_p = \frac{1}{Z_p} = j\omega C_0 + \frac{1}{j\omega L_p + R_p} \tag{1.10}$$

Where; Z_p = bulk plasma impedance; $C_0 = \epsilon_0 A/d$ is the vacuum capacitance for a slab of length d and cross-sectional area A; $L_p = {\omega_{pe}}^{-2} {C_0}^{-1}$ is the bulk plasma inductance and $R_p = \nu_m L_p$ is the bulk plasma resistance [16].

The resistor R_p represents the collisional power dissipation by electrons in the plasma bulk; while the L_p is the inductance caused due to electron inertia i.e. for a fraction of a time after the electric field direction has changed; the electron do not change its direction causing an effect of self-inductance in the bulk plasma.

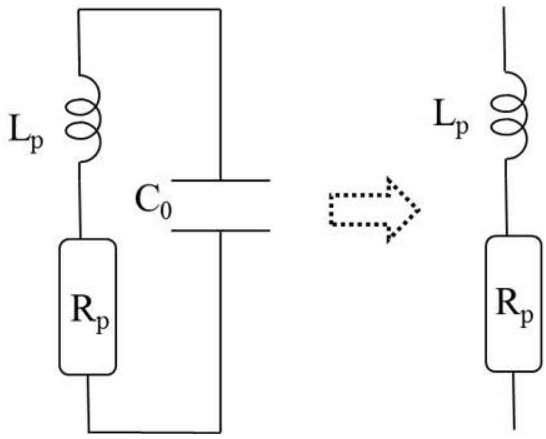

Figure 1.4: Electrical analogy for the bulk plasma

By inspecting Eq:1.10 ; it can be concluded that the electrical analogy of the plasma bulk is a vacuum capacitor C_0 in parallel to plasma inductance L_p and the plasma resistance R_p in series as seen in Fig 1.4. Since, in the bulk plasma the conduction current dominates over the displacement current; the reactive impedance due to bulk plasma capacitor C_0 which appears in parallel to the plasma bulk can be ignored. Therefore the overall plasma is simply represented by a resistor R_p in series with an inductor L_p.

1.2.5 Electrical analogy of the CCRF plasma discharge

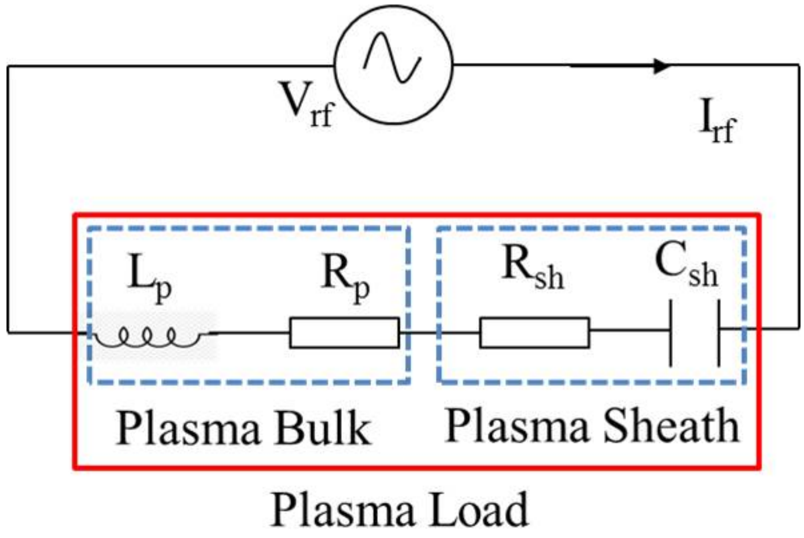

Figure 1.5: Electrical analogy for a symmetric CCRF plasma

Fig 1.5 shows the complete equivalent circuit of a CCRF discharge. The sheath resistance R_{sh} and the sheath capacitance C_{sh} are in series with the resistor R_p and the inductor L_p of the plasma bulk. As per Fig 1.5, the CCRF discharge circuit is essentially an R-L-C series circuit constituting of bulk plasma inductance and the sheath capacitance in series. A resonance condition can be observed if the capacitive sheath (-ve) reactance and the inductive (+ve) reactance of the bulk plasma cancels each other. Under the resonance condition, the plasma load will behave as a purely resistive load [17].

1.3 Fundamental limitation of a CCRF plasma in processing

Plasma substrate processing is ultimately dependent on two parameters 1) Bombarding Ion energy and 2) Bombarding Ion Flux. In CCRF plasma; the time averaged DC potentials in the sheaths determine the first parameter; while the electron loss (\plasma density) from the plasma controls the second parameter. As the RF power is increased;

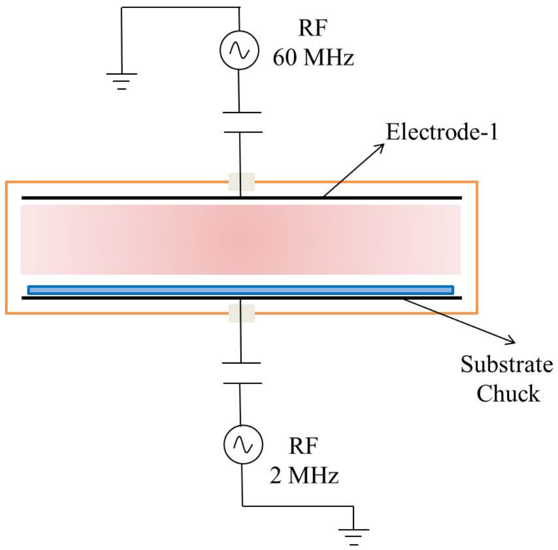

Figure 1.6: Dual-Frequency CCRF plasma reactor

it is seen that the DC potentials in the sheaths increases along with the bulk plasma density. Therefore the ion energy as well as the ion flux increases simultaneously and hence CCRF plasma discharge struggles to provide an independent control of ion flux and energy on to the processing substrate. To overcome this limitation different methods have been adopted. These are discussed in the next subsection.

1.3.1 Dual/Multiple Frequency CCRF discharge

As seen in Fig 1.6; in this technique, the two parallel plate electrodes are driven by two disparate (2/60 MHz) frequency power supplies simultaneously. Since, the capacitive sheath reactance $X_{sh} = 1/f_{rf}$ is inversely proportional to the driving frequency; it is possible to drive higher current through the plasma at higher RF frequency. On the other-hand if the frequency is low then, the DC potential drop across the sheath increases with RF power level. The dual frequency CCRF plasma system combines the two effects by powering one electrode with high frequency RF power and other with the low frequency RF power as shown in the Fig 1.6. The plasma density (Electron/ion flux) in the plasma reactor could be modified by increasing or decreasing the RF power level of higher frequency (usually 60 MHz); while the lower frequency is applied to the electrode which is attached to the substrate ; The potential drop across the sheath (ion energy) by changing RF power level provides a controlling mechanism for positive ion bombarding energy at the substrate. This method has been extensively researched and been applied on a commercial scale for plasma processing. Moreover, similar concept has also been used to control plasma by powering the same electrode with two disparate frequency power source [3].

1.3.2 Tailored waveform to create CCRF discharge

This is a novel technique to control the ion flux and ion energy onto the processing substrates by using single/dual frequency pulsed voltage waveforms. PIC (Particle-in-cell) simulations were used to demonstrate different capabilities of pulsed voltage waveforms to control the ion flux/energy. It was shown that by reducing the pulse widths of the voltage waveform; plasma density and power deposition can be increased [18] [19]; it was also predicted that average ion energy could be kept constant for increasing ion flux to the electrodes. Additionally, PIC simulations by different group showed that by changing the phase between 2 or more voltage harmonics in dual frequency CCRF plasma, the ion flux could be kept constant for increasing ion energy onto the substrate [20] [21]. This technique was experimentally validated by Lafleur et.al [4] to obtain control of the ion flux/energy by using a tailored waveform.

The tailoring of the RF power waveform modifies the sheath expansion and contraction corresponding to the potential on the electrodes. This indirectly affects the stochastic heating of the electrons as collision with sheath changes to control the plasma density (\ion flux); while it also changes the capacitive reactance of the sheaths which gives indirect control on the ion energy.

1.3.3 External Magnetic field to control plasma

Fundamentally, when a magnetic field in introduced in a plasma; charge particles undergoes two simultaneous motions a) a gyrating motion around the axis of B-field and b) a guiding center motion of particles in $\vec{E} \times \vec{B}$ direction. The gyrating motion is governed by the gyro/cyclotron frequency ($\Omega_c = |q|B/m$) and gyro radius ($r_L = mV_\perp/|q|B$) of the charged particles; where m=mass of particle, q – charge of particle and $V_\perp$ velocity of particle in plane perpendicular to the B-field. For the present experimental investigation; only the lighter plasma electrons are magnetized in a partially magnetized plasma. The guiding centre velocity of these magnetized electrons are then given by $v_e = (\vec{E} \times \vec{B})/B^2$; which for a case when $\vec{E} \perp \vec{B}$ becomes $v_e = E/B$. As the plasma electrons exhibit this drift creating to flow in the plasma; which drastically changes the plasma In a bounded laboratory plasma; this drift current cannot flow unimpeded and therefore; plasma rearranges itself to hold these electrons from escaping the system. Although ions are not magnetized in partially magnetized plasma; it is indirectly affected by the electron motion. As charge build up in a localized plasma region cannot occur to maintain quasi-neutrality. This rearrangement in plasma creates $\vec{E} \times \vec{B}$ induced inhomogeneity in the plasma It also follows that when, different forces act upon ions and electrons; then electrons and ions transport rates would also be different by diffusion. If such a condition of differential transport has a divergence, it would lead to charge density build up. This charge build up will alter the transport of the charge species again such that they become equal which is the condition of ambipolar diffusion in plasma [10].

As discussed above introduction of an external magnetic field into a plasma; changes the plasma dynamics and effects the intrinsic plasma parameters; therefore its use to control the CCRF plasma is an exciting topic of research; with numerous efforts to harness the potential of magnetic field as a controlling mechanism.

You et. al [6] [5] recently showed that a transverse magnetic field can control the RF power coupling to individual species (electrons/ions).In that work, with the help of EEPF (Electron Energy Probability Function) measurements it was also reported that increment in magnetic field at lower pressures leads to preferential heating of the low electron energy group; while at the intermediate pressures of ($\approx 40.00Pa$) the low electron energy electrons are cooled. A recent simulation study [7] also presents the feasibility of the magnetic field to control the power coupling into individual species. The fundamental reason for this ability of magnetic field is due to its dissimilar effects on the two species magnetized electrons and the un-magnetized heavy ions. The inherent response of the ions and the electrons to the introduction of the magnetic field could be exploited to control the ion flux/energy to the electrodes. Despite these efforts, B-field effects on CCRF plasma have not been extensively studied experimentally. This thesis therefore attempts to comprehend the effect of external magnetic field on the RF power coupling to individual plasma species and the overall plasma dynamics although; some of the effects of introducing a magnetic field to a plasma discharge are well known such as [11];

1. B-field reduces the non-ambipolar losses of charge particles from the plasma system. Thus relatively a higher plasma density at a given RF power can be achieved.

2. A B-field introduced transverse to the sheath electric field can enhance the stochastic electron heating inside the oscillating RF sheath. The gyrating electrons around the magnetic field can encounter multiple collisions with the expanding/collapsing sheaths.

3. B-field also increases the effective collisions inside the bulk plasma. Therefore, effectively a high pressure scenario can be reached at low operating pressures, with enhanced ohmic heating in the bulk. The concept of effective pressure due to magnetic field has been introduced to account for the increases in collisions [5].

4. The magnetic field also reduces the overall effective loss area of the discharge and also directs a greater fraction of the escaping plasma to the powered electrode, increasing the ion flux.

These effects of B-field have been used to design commercial parallel plate plasma processing reactors such as a Magnetized Enhanced Reactive Ion Etchers (MERIE). MERIE reactors introduce a transverse magnetic field to capacitive coupled plasma such that a $\vec{E} \times \vec{B}$ drift is as shown in the Fig 1.7 Although such improvements are achieved by intro-

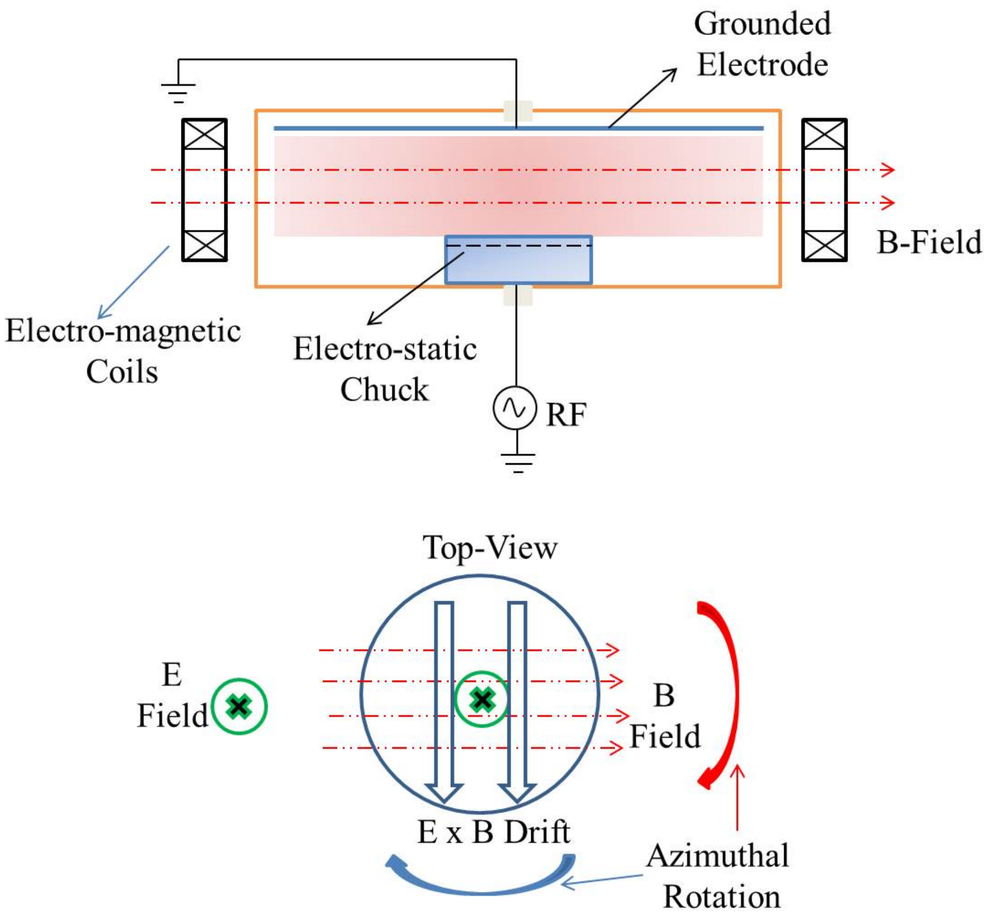

Figure 1.7: MERIE reactor

duction of magnetic fields; however it also introduces plasma non-uniformity due to$\vec{E} \times \vec{B}$ drifts, which limits their applicability for substrate processing. These drifts can bring process non-uniformity over the electrode. To reduce the azimuthally non-uniformity magnetic fields are rotated (0.5 Hz) on the plasma electrode axis [11].

1.4 Outline of the thesis

The thesis is organized as follows. Chapter-1 provides an introduction to capacitive discharges with their applications, limitations, control mechanisms along with magnetization as a proposed control parameter. Chapter-2 details the experimental setups (Parallel Plate/Cylindrical) along with the Langmuir probe diagnostics techniques used in the thesis. Chapter-3 details of the various RF power delivery schemes, RF grounding schemes and the matching networks used in the experiments along with the Voltage/Current probe calibration techniques for impedance measurements. Chapter-4 relates to the power mode transitions seen in a CCRF discharge. This chapter discusses the effect of transverse magnetic field and ion mass on the power coupling through the magnetized sheaths for both the experimental setups. Chapter-5 confers to electron series resonances (ESR) in a capacitive discharge in presence of transverse magnetization and effects of pressure on ESR; in conjunction with experimental and theoretical results. Chapter-6 interprets the impedance measurements of the cylindrical CCRF setup and relates them to the plasma parameters measured by the hybrid triple langmuir probe besides also discussing the effect of closing the $\vec{E} \times \vec{B}$ drift on the radial uniformity of the plasma. The summary/conclusions of the experimental work and the proposed future work are finally presented in Chapter-7 of this thesis.

Chapter 2

Experimental Setups and Diagnostics

The first part of this chapter presents the details of the experimental setup designed for investigating the magnetization effects on a CCRF plasma discharge including a brief motivation. Specifically, two types of electrode configurations have been investigated; 1) Parallel Plate and 2) Cylindrical electrode system. The experiment performed with parallel plate electrode configuration is conducted in a cylindrical glass vacuum chamber; whereas magnetized CCRF using cylindrical electrode configuration is conducted in a linear plasma device called BEAM (**B**asic **E**xperiments in **A**xial **M**agnetic field) Device. The second part of the chapter devotes to the theory and application of different type of electrical probes that have been applied for plasma diagnostics.

2.1 Experimental setups

2.1.1 Magnetized CCRF with planar electrode

This experiment was originally motivated to study the effects of introducing a uniform magnetic field in parallel plate electrode configuration, and to carry experimental studies on RF plasma interaction with an oblique magnetic field. Parallel plate CCRF configuration is also widely used in plasma processing industries. Previous papers on magnetized CCRF discharges were conducted using circular electrode plates with the magnetic field being parallel to the electrode surface [22]. It was found that the interaction of the RF electric fields and a static magnetic field gave rise to inhomogeneous plasma density between the circular plates. This primarily occurred due to cross-field drift of electrons in a particular direction perpendicular to both the electric and magnetic field.

The present experimental setup as seen in Fig: 2.1, consists of a pair of SS-304 rectangular electrode plates having length of L=420 mm and width w=100 mm. The plates were separated by a gap (g) of 80 mm. The electrode length (L) is therefore 5 times the spacing (g) between the top and the bottom electrodes. Therefore one may ignore the edge effects along the length of the discharge plates. The magnetic field is produced externally by a pair of electromagnet coils and it points along the width of the discharge plates. The electrode configuration is suitable for benchmarking 1-D/2-D simulation studies of magnetized CCRF discharge.

In the experiment, argon discharge is created for a range of neutral gas pressure (1.0 - 5.0 Pa); while the magnetic field is produced with a pair of electromagnetic coils. Concurrently, similar set-up has been simulated by Particle-In-Cell simulation code in Ref [23]. This simplistic configuration of magnetized CCRF discharge can be useful in simulating RF electron dynamics in presence of magnetic field. RF plasma interaction with external magnetic field in the near field region of an ICRF antenna used for plasma heating in tokomaks pose several challenges due to anomalous drifts of charge particles resulting in hot spots/ localized heating of the surface [24]. The parallel plate setup is also relevant from an industrial application stand point such as MERIE [Fig1.7, chapter-1]; wherein flat substrates constitute the discharge circuit.

Fig 2.1 shows the photo-graph of the planar CCRF electrode assembly. The top and the bottom electrodes are powered in push-pull configuration such that the RF voltage at each electrode is 180 degree out of phase. In order to confine the discharge between the inner

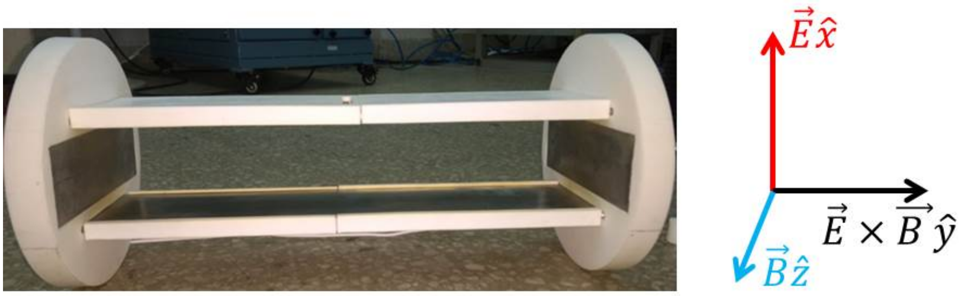

Figure 2.1: Electrode assembly with the axis notations

regions, the outer surface of the electrode is covered by a Teflon dielectric; a pair of Teflon support discs holds the two electrode assembly against the inner bore of the glass vacuum chamber. Also there are two floating S.S. plates (11.0 × 6.0 cm); which are flush mounted on the supporting teflon discs. These electrodes are shorted by a Teflon insulated copper wire (shown in Fig 2.2 by red dotted lines).

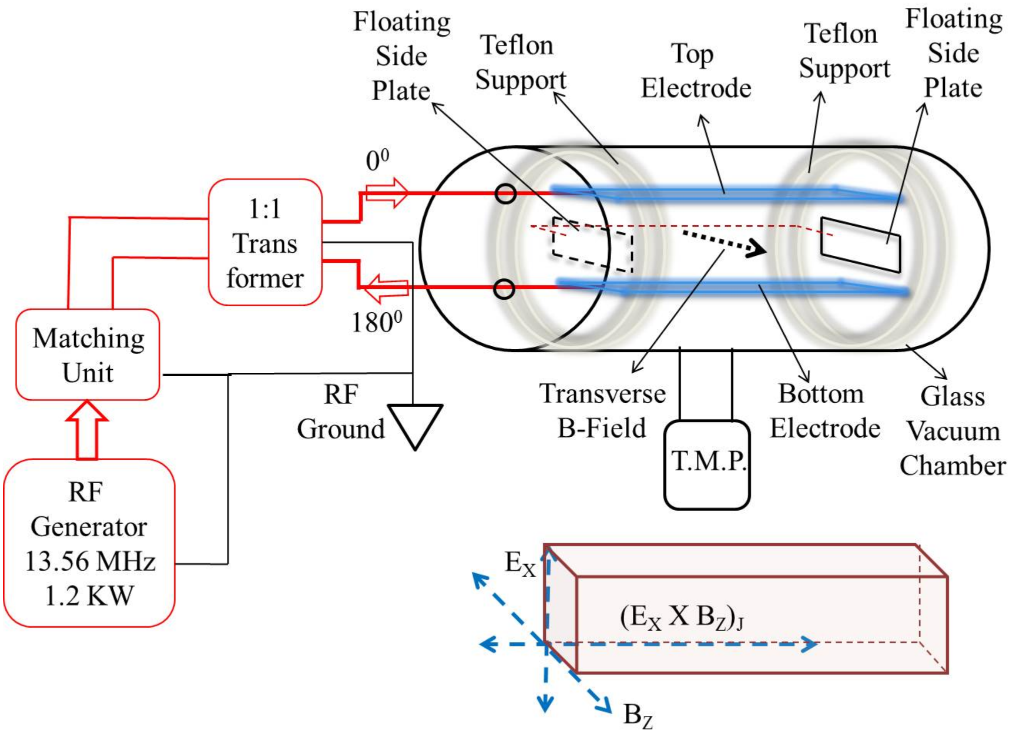

Figure 2.2: Schematic of the parallel plate experimental setup with Axis

The electrode assembly is introduced inside a cylindrical glass vacuum chamber as shown in Fig: 2.2. The glass chamber is 100 cm in length and inner diameter of 21.5 cm. A base pressure of 10^{-5} mbar can be rapidly achieved inside the chamber with help of a turbo-

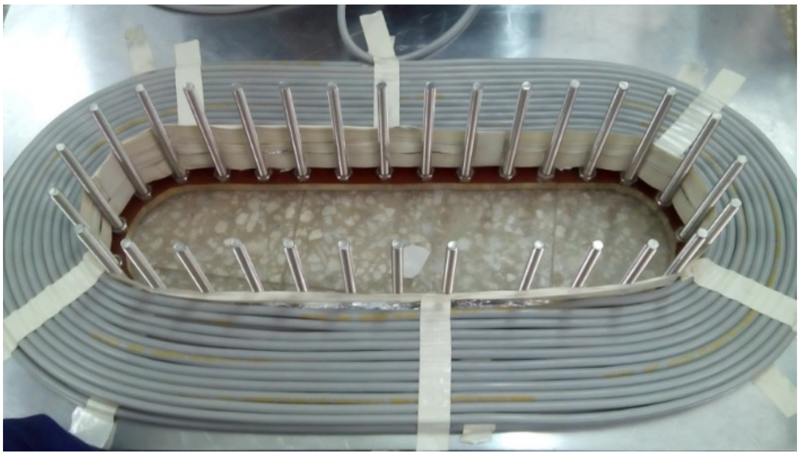

Figure 2.3: Race-track shaped electromagnetic coil

molecular /Rotary backing pump. The magnetic field is produced by a pair of race track shaped electromagnet coils as shown in Fig 2.4. The coil windings are shown in Fig 2.3. The coils are placed outside the glass chamber producing magnetic field pointing along the z-axis (p.c. Fig 2.1). The maximum of 7.0 mT steady state magnetic field can be achieved by passing 40 A current through the coils.

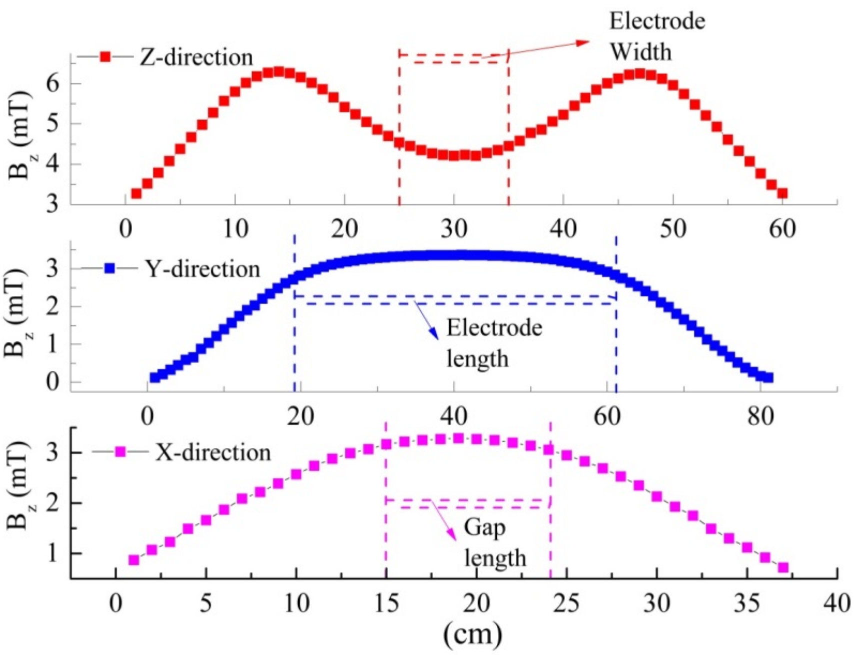

Figure 2.4: Field mapping of B_z in all three directions

Fig 2.4 shows the B_z component of the magnetic field along all the three axis. The magnetic field data corresponds to 20.0 A DC current passed through the coils. The B_z can be considered to be almost uniform over the volume of the electrodes.

2.1.2 Magnetized CCRF with cylindrical electrode

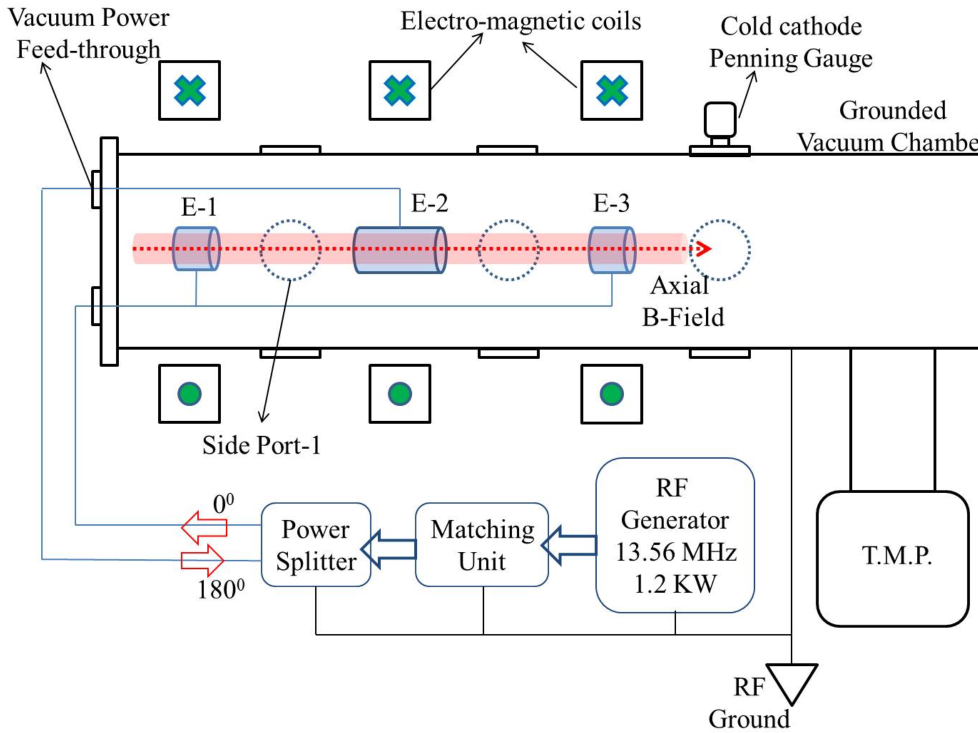

Figure 2.5: Schematic of the cylindrical CCP setup

The magnetized CCRF system with cylindrical electrodes consists of three hollow cylinders (E1, E2 and E3) and center to center gap of 27.0 cm as shown in Fig 2.5 such that they are aligned with the three external Electromagnetic Coils. The inner diameters of all the three electrodes are 6.5 cm; while the length of the cylinders E1 and E2 is same and their sum total is equal to the length of the cylinder E3 which is 10 cm. This is designed to create a geometrically symmetric CCRF plasma discharge by driving the electrodes E1 and E2 with respect to the electrode E3 in push pull configuration. Experiments in this setup are conducted in argon and helium at neutral gas pressures of 1.0 Pa.

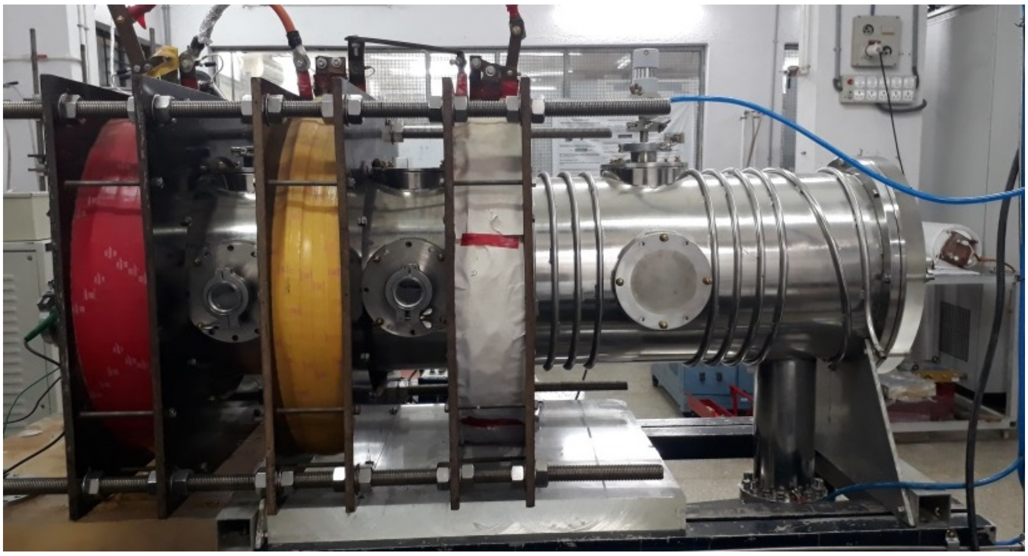

Figure 2.6: BEAM Setup

The electrode assembly is introduced in the BEAM experimental setup which consists of three electromagnetic coils in modified Helmholtz configuration placed at a gap of 27.0 cm between them. The configuration gives a peak axial magnetic field of 28.6 mT at 100A current, which is uniform radially.

A plot of axial magnetic field is shown in Fig 2.7. The cylindrical electrode configuration is suitable for sustaining uniform plasma column in the BEAM setup. Linear devices are generally used for various fundamental studies as briefly outlined in chapter-6 of the thesis.

The linear experimental chamber is a 1.2 m cylindrical vacuum chamber having inner diameter of 0.3 m made of SS-304. The vacuum chamber can be evacuated to a base pressure of 10^{-5} mbar with a Turbo-molecular/Rotary pump set. The vacuum chamber has sufficient 40 KF ports [p.c. 2.6] for inserting electrical probes at various location for the diagnostic of magnetized plasma column. The chamber is electrically grounded to a dedicated earth-pit.

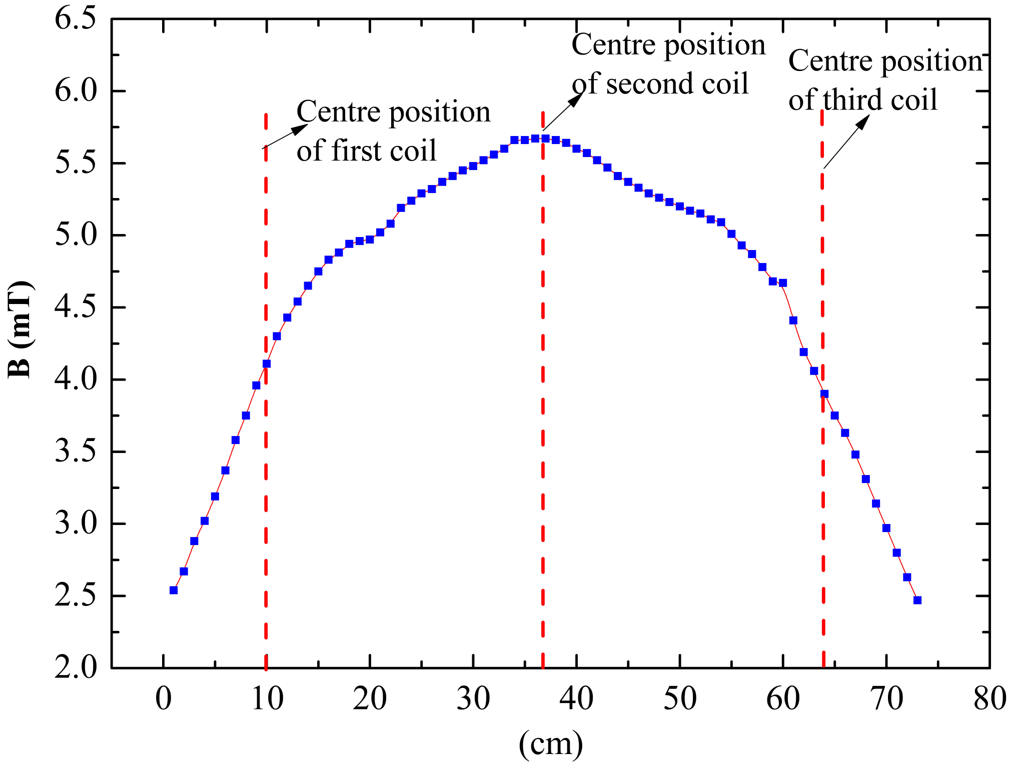

Figure 2.7: Axial field map of BEAM setup at 20A DC current

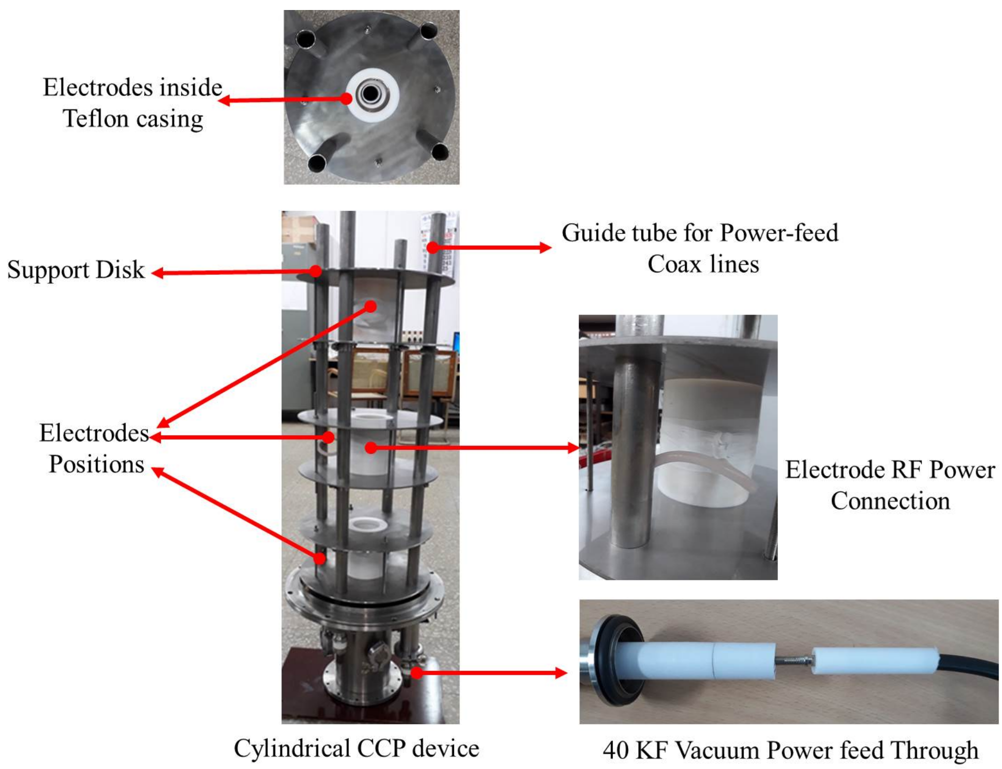

Figure 2.8: Cylindrical CCRF source with support structure

In order to house the RF electrode assembly inside the experimental chamber, a special structure has been designed as shown in Fig 2.8. The support structure consists of three pair of annular SS 304 plates for holding the respective E1, E2 and E3 RF electrodes. These electrodes are inserted in Teflon tube which isolates them from the annular plates. The plates are aligned using 4 guide tubes through which the PTFE sheilded RF electrical cables are also taken out from the individual electrodes. The SS tubes are grounded therefore it reduce the RF radiations and restrict the discharge to occur only between electrodes. A special 40 KF vacuum feed-through for RF power connection is used to supply the RF to these individual electrodes. The connections to the copper feed-throughs are encapsulated by teflon sleeves [p.c. Fig 2.8] inside the vacuum chamber. The final connection to the electrodes is through the teflon casings which is also shown in Fig 2.8. Finally the entire supporting structure is mechanically attached to the end flange of the BEAM experimental setup.

2.2 Plasma Diagnostics

Electrical probes have been used in the experiment for measuring the intrinsic plasma parameters inside the magnetized CCRF discharge. Three main types of probes have been developed and applied in the experiment. An RF compensated Langmuir probe and emissive probe was initially designed, however a straightforward method to determine the plasma density and electron temperature using hybrid probe was developed. The obtained plasma density using this new technique has been benchmarked against a resonance hairpin probe, which is a well known method for determining electron density inside the discharge. This section briefly describes the theory and application of different probes, with more emphasis on the performance of the hybrid probe as all the experimental results presented in the subsequent chapters have been carried using the hybrid probe technique.

2.2.1 RF compensated Langmuir probe

The Langmuir probe is a well known technique for determining plasma parameters, namely the plasma density (n_0), electron temperature (T_e), floating (V_f) and plasma (V_p) potentials. These quantities can be readily obtained from the plots of current-voltage characteristic of the probe inserted inside the plasma. Elegant literatures on the probe are available which explains the methodology for determine the plasma parameters from the Ampere-Voltage characteristics inside a plasma [25] [26].

Fig 2.9 presents a typical characteristic of electron current collection by the Langmuir probe in a RF Plasma. The non-linear curve showing electron saturation current at higher voltages is generally observed in a DC plasma, in which the plasma potential V_p remains fixed at a certain positive value above the reference grounded electrode. However in RF plasma, this characteristic shifts due to sinusoidal oscillation in plasma potential V_p. As a result the electron current characteristic (green curve) traces an average of the two characteristics, giving a distorted Langmuir probe characteristic in RF plasmas.

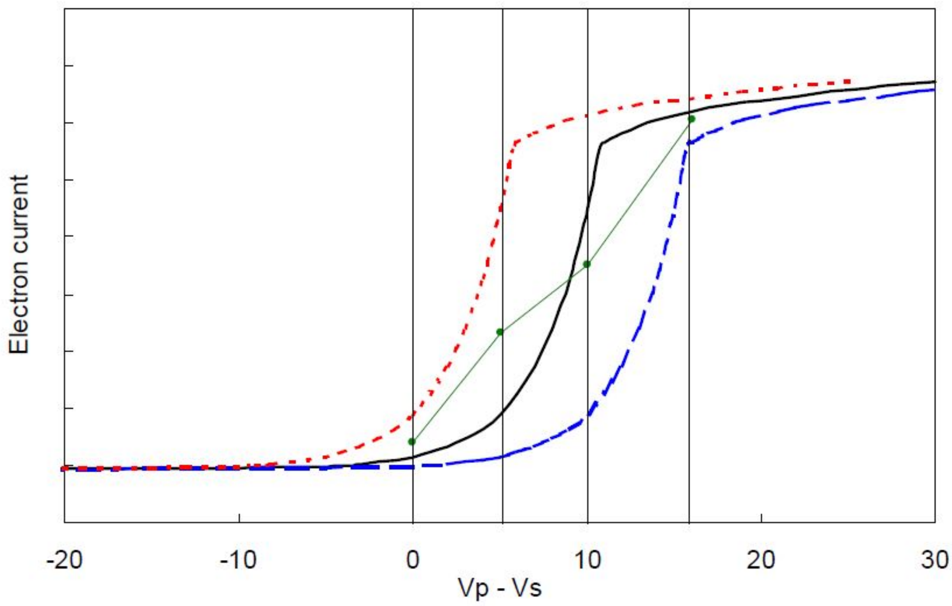

Figure 2.9: Center Black curve is the actual characteristic, while the Red and Blue are +/- 5V shifted curves. The vertical lines show the averaged electron current of the Red and Blue curves; which is different from the black curve. Picture Courtesy: FF Chen Lecture Notes [27]

The above problem is addressed by introducing a tank circuit in the vicinity of the probe tip, which offers very high impedance to the RF probe current up to 3rd order harmonics. Fig 2.10 shows the schematic of this circuit which is also popularly known as passive compensation circuit [27]. As shown in the Fig 2.10, the auxiliary probe is necessary since the primary condition for RF compensation of Z_{ch} (tank circuit impedance)»Z_{sh}(sheath impedance) is very difficult to achieve at 13.56 MHz [27]. The auxiliary probe with bigger surface area have a much lower sheath impedance and short circuits the RF fluctuations to the probe tip through the capacitor. Therefore, the probe tip is AC/RF biased from the plasma. Excellent reviews on the use of RF compensation have been given by various authors [27].

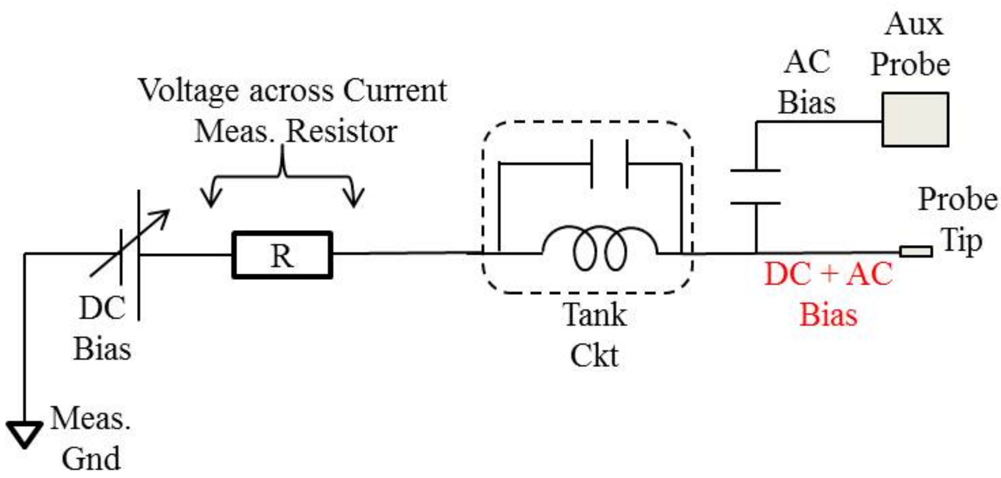

Figure 2.10: Schematic of the passive RF compensated Langmuir probe.

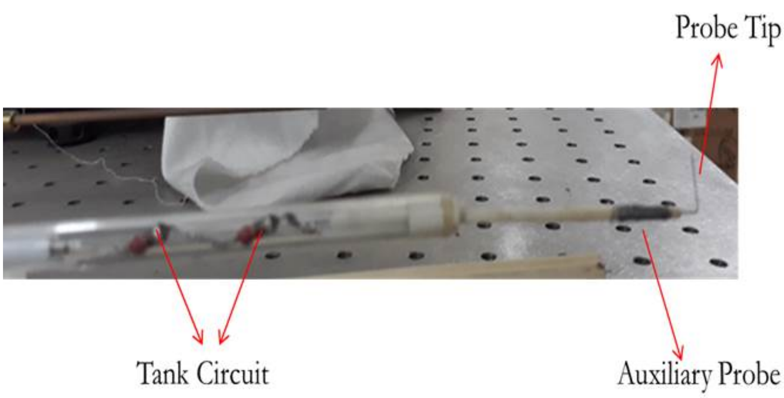

Figure 2.11: RF compensated probe.

A typical RF compensated Langmuir probe designed in-house for application in the present experiments at the beginning is shown in Fig 2.11. The probe is made of tungsten cylindrical tip (6.0 mm long with diameter of 0.2 mm) taken out of ceramic capillaries, housed inside a glass tube. This whole assembly is less than 10.0 cm in length. The pair of inductors had self-resonating frequency (SRF) of 13 MHz. The auxiliary probe of surface area around 60 mm^2 is made by tungsten wire wound on a ceramic tube. The auxiliary probe is connected to the main probe through a ceramic capacitor of 10.0 μF. The inductors offer impedance of $\approx 35k\Omega$ at 13.56 MHz while the reactive impedance at the sheath is estimated to be around $\approx 10\Omega$. Therefore, the condition for RF compensation $Z_{ch} >> Z_{sh}$ is satisfied for 13.56 MHz.

2.2.2 Plasma potential measurement by Emissive probe

For obtaining direct measure of the plasma potential, an emissive probe had been designed and introduced inside the discharge. This method has been widely used in DC/ pulse-dc magnetron discharges and in RF plasmas [28] to tokomaks [29].While one may heat the loop/tip with help of a laser [30]; typically, joule heating is preferred; due to convenience and affordability of the method. Essentially this probe consists of a conducting loop of wire which is made to thermionically emit electrons [31] by passing DC/AC current from a centre tap transformer as done in our case. As the probe is heated to emit electrons, its floating potential tends to shift towards the plasma potential and saturates above a critical saturation emission from the probe surface. Then the flux balance between the electrons and positive ions is modified and the potential on the surface starts to shift towards the plasma potential. Hobbs and Wesson derived this equation by including the electron emission flux to obtain the below relation [32];

$$V_f - V_p = -\frac{T_e}{e} ln(\frac{1-\Gamma}{\sqrt{\frac{2\pi m_e}{m_i}}}) \tag{2.1}$$

Where, Γ is the ratio of emitted electron flux to the collected electron flux. They also found that once Γ reaches a critical value of $\Gamma_c = 1 - 8.3\sqrt{\frac{m_e}{m_i}}$; the floating potential (V_f) saturates $\approx T_e/e$ V below the plasma potential (V_p).

The above method of determining the plasma potential is commonly known as floating point technique [33]. Besides the inflection point in the limit of zero emission [34] and 3) and the separation point method [35] [36] are also used to determine the plasma potential using an emissive probe. Elegant review on the emissive probe was done by Sheehan and Hershkowitz [37].

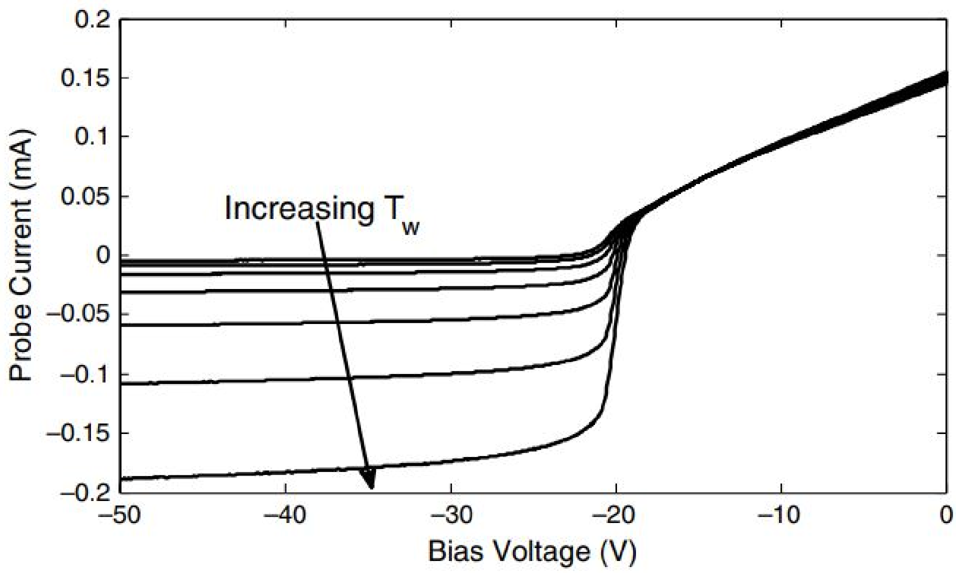

Figure 2.12: Sample I-V plots for increasing temperature (/emission) on the probe. ©IOP publishing. Reproduced with permission [37]

A topical review of emissive probes by Sheehan and Hershkowitz [37] plots the complete I-V characteristics of plasma for increasing probe tip temperatures T_w (\ electron emission) as seen in Fig 2.12. In this plot of I-V characteristics as a function of temperature of floating loop (probe); it is seen that as the temperature T_w is increased, emission increases and the I-V shifts lowers bringing the floating potential closer to the plasma potential $\approx -21V$. As the emission increases, the potential on the probe saturates. This method is particularly useful for RF plasma as complete I-V trace is not required for determining the V_p.

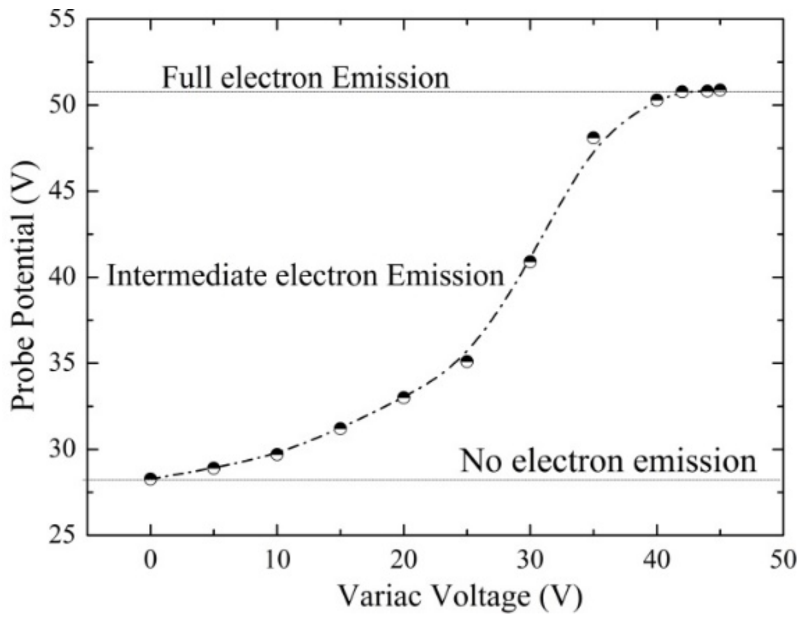

Figure 2.13: Sample floating potential V_f measured with increasing electron emission

The emissive probe circuit shown in Fig 2.14 consists of a centre-tap, toroidal step-down (12.7:1) transformer used for joule heating the probe [31] [37]; The variac is used to vary the 230V, 50 Hz, AC mains supply to the input side of the toroidal transformer. The secondary of the toroidal transformer is connected to the emissive probe loop and heated to emission. The floating potential is measured at the centre-tap with respect to the measurement ground used in the Digital Storage Oscilloscope (DSO). Suitable probe vacuum-feed-through and electrical connections have been constructed for this experiment.

For electropositive plasma, the electron temperature T_e is associated to the floating and plasma potential through a relation given by [11];

$$V_p - V_f = \frac{T_e}{e} ln(\sqrt{\frac{m_i}{2\pi m_e}}) = \delta T_e \tag{2.2}$$

Where, T_e is in eV and $\delta = 5.19$ for argon and 4.02 for helium. Thus, emissive probe can measure electron temperature T_e with the error in the measurement of the order of T_e/e [38].

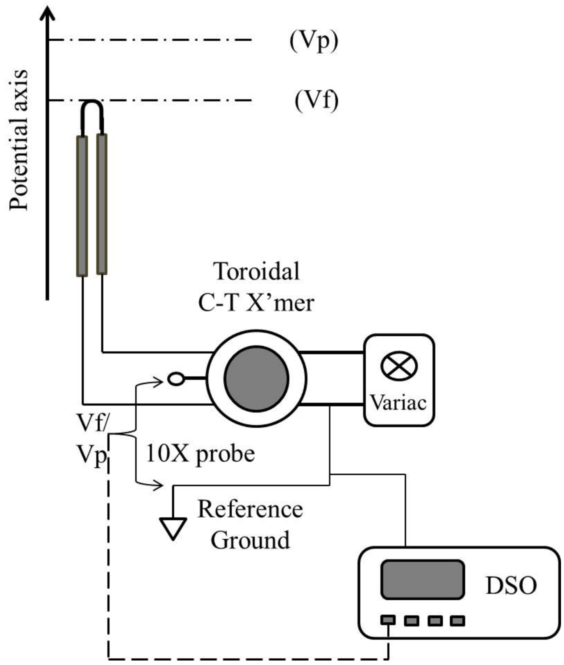

Figure 2.14: Schematic of the Emissive probe circuit used in the experiment

2.2.3 Floating hairpin probe technique for electron density measurement

The hairpin probe is an elegant method for determining electron density n_e in a low pressure discharge [39]. In the past two decades, it has been extensively used for application in wide range of plasmas including industrial RF plasma systems [40], electronegative discharges [41] as well as in magnetized plasma systems [42]. Some variation of this technique has also attracted attention such as cut-off probe which had been applied for determining the collision frequency [43]. In the present study, the hairpin probe has been applied for benchmarking plasma parameter by other probing techniques.

Essentially the hairpin probe is a quarter-wave transmission line introduced inside the plasma medium [39]. A quarter-wave transmission line exhibits resonance when excited at a frequency$f_r = c/4l\sqrt{\epsilon_r}$; [39] where c-speed of light, l is the length of transmission line and ϵ_r is the permittivity of the medium. Since plasma is a dielectric medium with relative dielectric constant ϵ_p;

$$\epsilon_p = 1 - \frac{\omega_{pe}^2}{\omega^2} \tag{2.3}$$

where, $\omega_{pe}^2 = 4\pi^2 f_{pe}^2 = \frac{n_e e^2}{\epsilon_0 m_e}$; while $\omega^2 = 4\pi^2 f_r^2$

ϵ_p can be introduced in the formula for f_r to obtain an expression for determining the electron density inside the discharge; which is given by [39];

$$n_e = \frac{f_r^2 - f_0^2}{0.81} \times 10^{16} m^{-3} \tag{2.4}$$

Here, f_0 and f_r are in GHz and corresponds to the resonance observed in plasma and in vacuum.

A typical waveform of probes resonance signal verses microwave frequency obtained from a voltage controlled YIG-oscillator is plotted in Fig: 2.15. The resonance signal corresponds to the rms value of the reflected signal obtained by a schottkey diode, and relates to the variable frequency supplied to the hairpin.

At the resonance frequency, the reflected signal falls to a minimal value and the corresponding frequency can be interpreted as the probes resonance condition obtained with/without plasma as displayed in the Fig 2.15. The measurement and data acquisition circuit for the heirpin probe is shown in Fig 2.16a

The hairpin probe can be constructed by folding a piece of tungsten wire 0.15 mm diameter, and a length of 27 mm, in to the shape of a hairpin such that the pins are separated by a gap of 3 mm. A small loop antenna is placed adjacent to the short-circuited end of the hairpin and it is used to inductively couple the microwave to the hairpin as shown in Fig 2.16c.

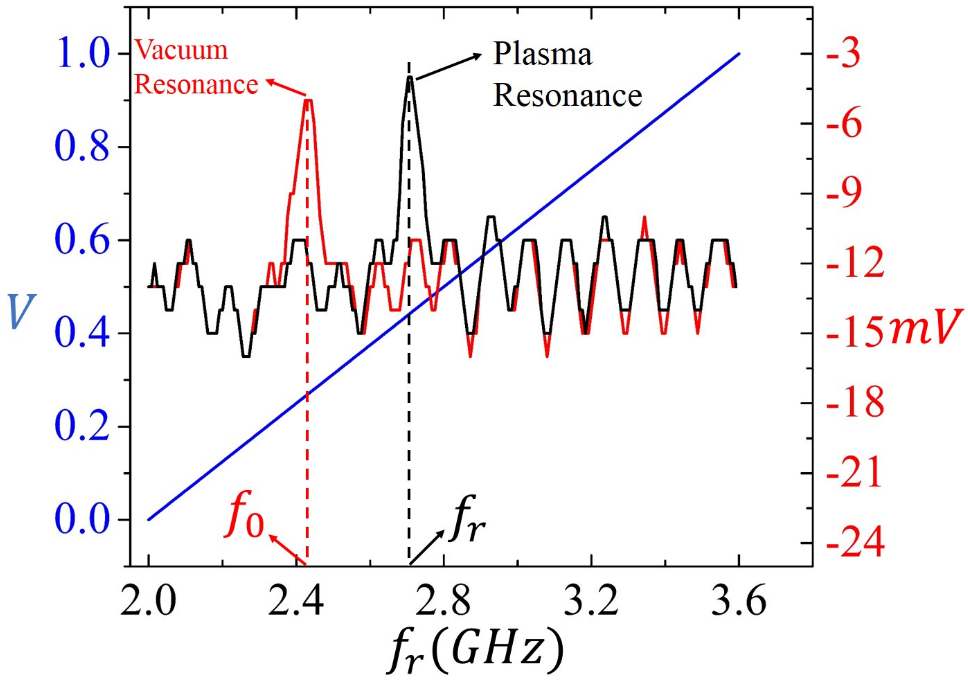

Figure 2.15: Shift in Resonance from Vacuum to Plasma

In a magnetized plasma, Gogna et.al [42], derived an equation which approximates the plasma dielectric to magnetized dielectric of the plasma $\kappa_{\perp} = [1 - \frac{f_{pe}^2}{f_r^2 - f_{ce}^2}]$

$$n_e = \frac{f_r^2 - f_0^2}{0.81}[1 - \frac{f_{ce}^2}{f_r^2}] \times 10^{16} m^{-3} \tag{2.5}$$

Where, f_0 – Vacuum Resonance Freq. f_r – Plasma Resonance Freq. and f_{ce} is the electron cyclotron frequency. In the experiments we conducted the measured value of $f_0 = 2.65GHz$; while the theoretical value is 2.77 GHz.

For all density calculations we use the measured value of the vacuum resonance. Fig 2.16b shows the orientation of the probe to be used in magnetized plasma.

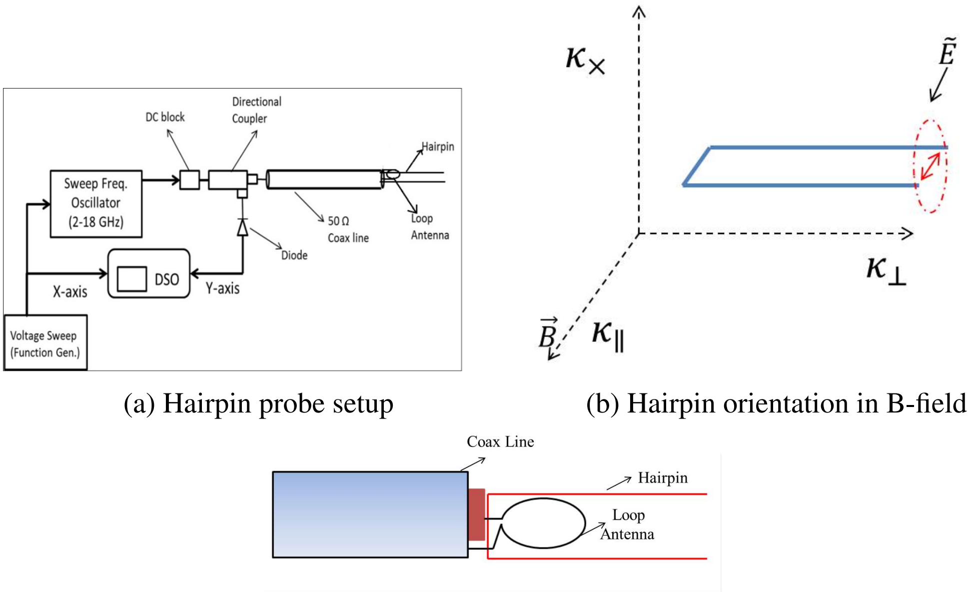

(a) Hairpin probe setup (b) Hairpin orientation in B-field

(c) Hairpin Probe

Figure 2.16: Schematic of hairpin Probe its setup and orientation to B-field

2.2.4 Hybrid triple langmuir probe

The hybrid probe is a concept derived from the application of a triple probe and an emissive probe. This technique is developed specifically for application in magnetized RF discharge by elegantly constructing the emissive and double Langmuir probe in the same probe feed-thru. The emissive probe directly measures the plasma potential V_p and the electron temperature T_e; while the ion saturation current is measured by applying a fixed potential between the double probe tips using a DC battery.

The construction of the hybrid probe is shown in Fig 2.17. The cylindrical probes P1 and P2 and a the emissive probe P3 is constructed on two dual bore ceramic capillary tubes.

The probes P1 and P2 identical are made of 0.2 mm diameter tungsten wires having individual length 6.0 mm. The emissive probe P3 is made with a 0.15 mm thoriated tungsten wire loop of diameter 3.0 mm loop. The probe tips P1 and P2 are separated by a distance of 2.5 mm, while P3 is at a distance of 3.0 mm from P1 and P2. All the probes are close enough to measure the same plasma conditions. The bunched ceramic capillaries

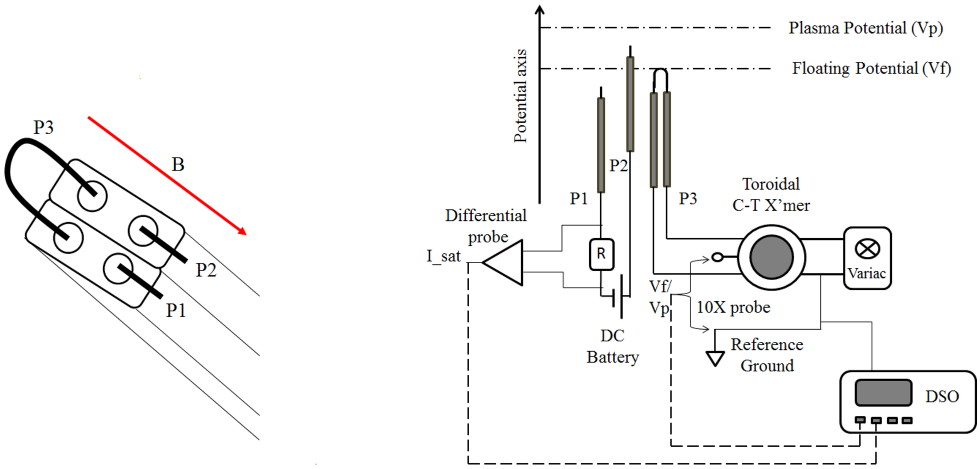

(a) Hybrid probe (b) Hybrid probe circuit

Figure 2.17: Schematic of hybrid probe and orientation to B-field

are less than 5.0 mm in dimension, with ceramic capillaries extending 3.0 cm out of the stainless-steel feed-through. The probe pins P1 and P2 are oriented such that the axis of the probe remains along the magnetic field. This configuration ensures homogeneous current collection on the probe surface [44]. Connections are taken out through purpose built hermetically sealed vacuum probe feed-throughs.

As shown in Fig 2.17b; a DC battery $V_{dc} = 50.0V$ is connected between probe P1 and P2; with P2 connected to the positive terminal of the battery. A current measuring resistor R is also connected in series to the two probes. With increasing the potential difference between the probe pins P1 and P2, the DC potential shifts with respect to the floating potential; The potential of the probe P2 shifts higher than the local floating potential, whereas the probe P1 shifts below the floating potential. As P1 and P2 are in series the current passing through them is controlled by probe P1; which can only collect the ion saturation current if $V_{dc} = 50V >> T_e/e$. This is a basic assumption applied in triple Langmuir probe operated in voltage mode [45] which has been notably applied to determine plasma parameters in the SOL (Scrape-off layer) regions in tokomak [35] [46]. Since, the hybrid probe is a variation on the conventional voltage mode triple Langmuir probe (TLP). TLP is briefly discussed.

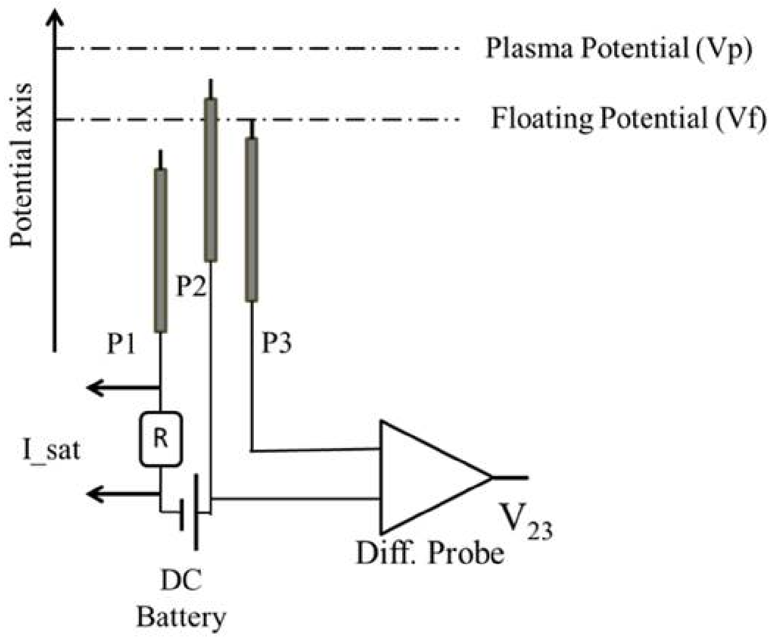

Figure 2.18: Voltage mode triple Langmuir probe

In a triple Langmuir probe (TLP) all the three probe pins (P1, P2 and P3) are identical and situated in the same plasma region, without interfering each other. Fig 2.18 shows the electrical circuit diagram of the TLP operated in voltage mode. The ion saturation current in the above circuit is measured across the resistor R. A differential voltage probe is used for measuring the potential between the positively biased probe P2 and the floating probe P3 which are required for calculating the electron temperature.

From the current balance at each probe; it can be derived that for $V_{dc} >> T_e/e$; the electron temperature could be given as;

$$KT_e = \frac{e(V_2 - V_3)}{ln2} = \frac{eV_{23}}{ln2} \tag{2.6}$$

While the current through the resistor R can be approximated to ion saturation current to estimate the positive ion density.

$$n_0 \approx \frac{I_{sat}}{\alpha A e U_b} \tag{2.7}$$

Detailed derivations for the voltage-mode triple Langmuir probe are available in literature and are not presented here [45]

2.3 Performance of TLP and Hybrid probe

Unlike a Single Langmuir probe, both TLP and Hybrid probe technique requires only a fixed value of DC bias voltage applied for measuring plasma parameters. Both the techniques can provide time resolved measurements in the frequency regime of few 10's of KHz [35]. TLP has been also recently applied in a HiPIMS plasma discharges [47]. However there is drawback in the application of TLP in an RF plasma which can give ambiguous results [48]. This is caused by the voltage measuring probes which are required to monitor the potential of the individual probe pins. However these probes introduces capacitive loading between the individual probes (P1, P2 and P3) during differential voltage measurements. This effect has been addressed in our publication also and presented here. Fig 2.19 shows the three possible configuration for measuring positive ion saturation current.

In Fig 2.19, the voltage drop across the current measuring resistor R provides the ion saturation current. This is obtained by a differential voltage probe (Siglent DPB5150) connected across the resistor and the signal is acquired in a digital storage oscilloscope - DSO (Tektronix 3034C).

1. In Fig 2.19a; the positive ion current is measured across resistor R with P3 floating and completely isolated from the measurement circuit with no measuring circuit connected to it.

2. In Fig 2.19b, which is the hybrid probe configuration; probe P3 is connected to the centre tap transformer, and a 10X high voltage probe is used to measure the floating and plasma potentials for Cold/Hot probe P3. While the ion saturation current is

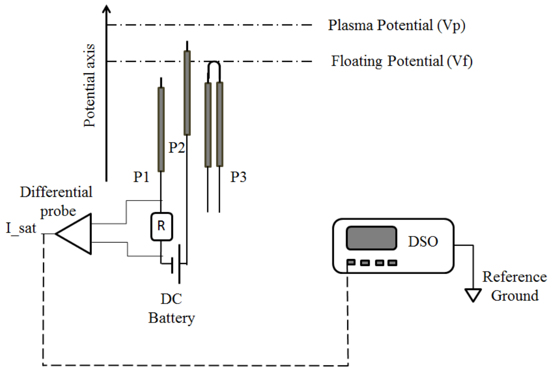

(a) P3 isolated

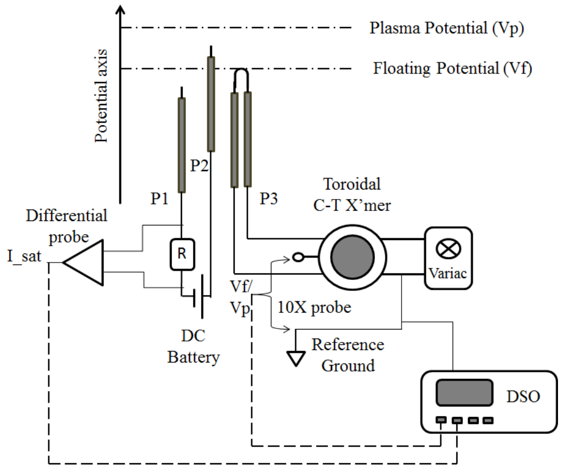

(b) Hybrid probe

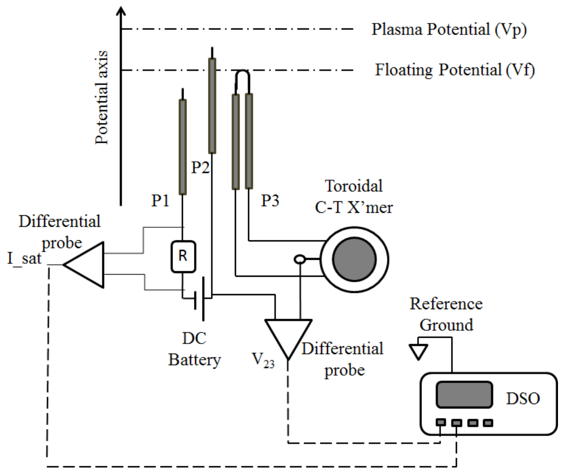

(c) TLP

Figure 2.19: Ion saturation measurement in 3 different Electrical configurations

measured across resistor R.

3. Finally, in the setup shown in Fig 2.19c; the voltage variac is removed from the circuit and the probe P3 is kept floating; while a differential probe (Siglent DPB5150) is connected between probes P2 and centre tap (Floating Potential – P3). Since the probe P3 is non-emitting, hence this configuration resembles a conventional triple Langmuir Probe (TLP) operated in voltage mode.

The ion saturation current obtained in all the three configurations for argon plasma column are shown below. This experiment was carried in the cylindrical electrode setup for a constant RF power at 60 W at 1.0 Pa while varying the axial B-field. Here the data shown in the figure are at the radial center of the plasma column with probe inserted between electrodes E1 and E2 from side port-1 as seen from 2.5.

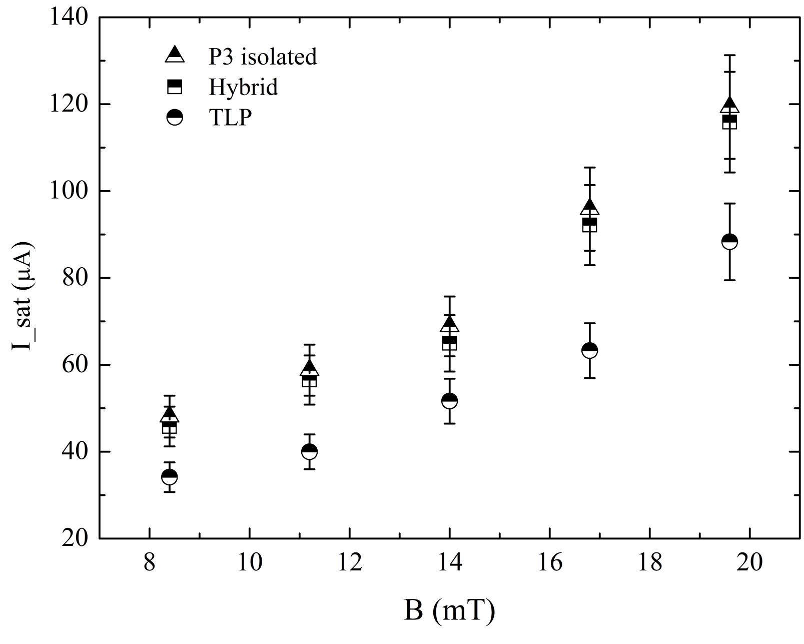

Figure 2.20: Ion saturation current variation with increasing magnetic field for different probe configuration at 60W Set RF Power

The ion saturation current obtained using conventional TLP measuring setup [c.f Fig 2.19c] gives a consistently underestimated plasma density. With the setup 2.19a on isolating the P3, the I_{sat} matches quite well with the ones obtained using the hybrid probe setup 2.19b. The mismatch in ion saturation current by the setups 2.19b and 2.19a is 5 % which is relatively smaller as compared 30 % difference observed with setup in Fig 2.19c. This result concurs with the observation by Eckman et.al [48] that the triple Langmuir probe is prone to have significant errors in RF plasma.

2.3.1 Benchmarking Experiments: The Hybrid Probe with Resonance Hairpin probe

To benchmark the plasma density measured from the hybrid probe; we independently measure the electron density at the same location with the help of a hairpin probe. The two densities are compared in the Fig 2.21 for various set RF power levels and axial magnetic fields for argon discharge at 1.0 Pa. From the Fig 2.21 it is seen that the plasma density increases almost linearly with increase in axial magnetic field; while it only increases marginally with rise in RF power levels. The reasons for such trends in plasma density and electron temperature are discussed in detail in Chapter-6.

It is also noted that the density measurements tend to show excellent convergence for magnetic field strengths below 5.6 mT. Conversely, as the magnetic field increases the measurements by the two probes deviates significantly. To quantify this deviation as a function of axial B-field; the ratios of the two densities $N = n_{hybrid}/n_{hairpin}$ are plotted in Fig 2.22

It is seen that the ratio N tends to grow as the magnetic field increases. To understand this aspect, we must consider the influence of B-field on the performance of both the probes. In the case of the hairpin, if the sheath correction factor [49] is ignored; then the effect of B-field is already included in the Eq 2.6 for calculating the electron density. Therefore, we consider the hairpin density as the reference to comprehend the effect of B-field on the hybrid probe plotted in Fig 2.22 .

The plasma density from the hybrid probe is given from the positive ion saturation current

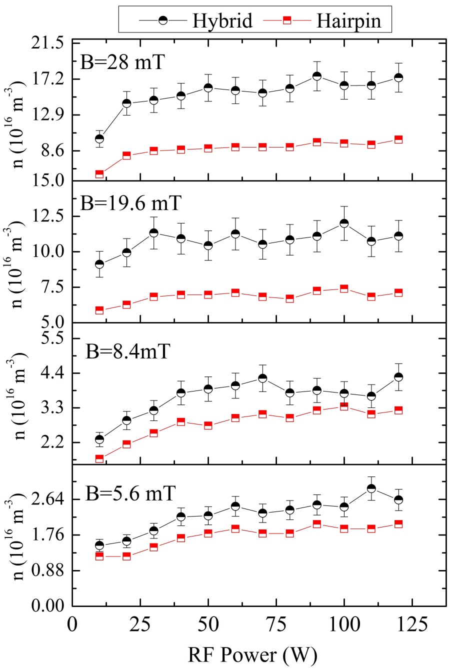

(a) Plasma density with increasing RF power

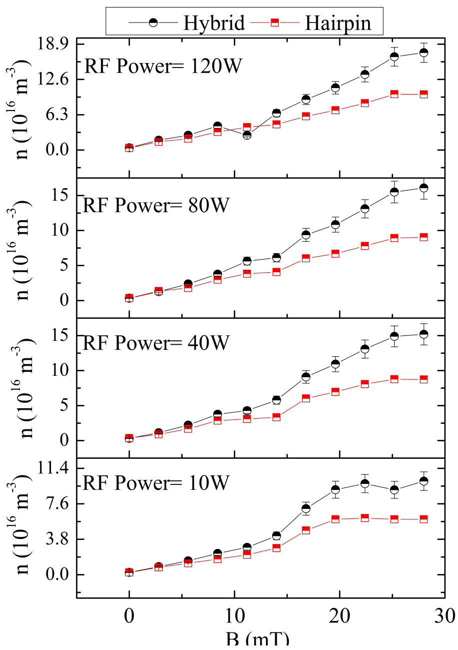

(b) Plasma density with increasing magnetic field

Figure 2.21: Plasma density by hybrid and hairpin probe

as;

$$n_0 = \frac{I_{sat}}{\alpha A e U_b}$$

From, this equation the measured plasma density depends inversely on the following three parameters

1. Parameter α

2. Probe Area, $A = 2\pi R_p L_p$; where R_p is the probe radius and L_p is the probe length.

3. Bohm velocity U_b

It was shown theoretically by Chodura [50] that for partially magnetized plasma the positive ion tends to enter the sheath at bohm velocity; while the potential drop in the sheath is also indifferent to the applied B-field as well as its angle of inclination. Therefore, the product αU_b is expected to remain constant. Similar results were also obtained by Kim

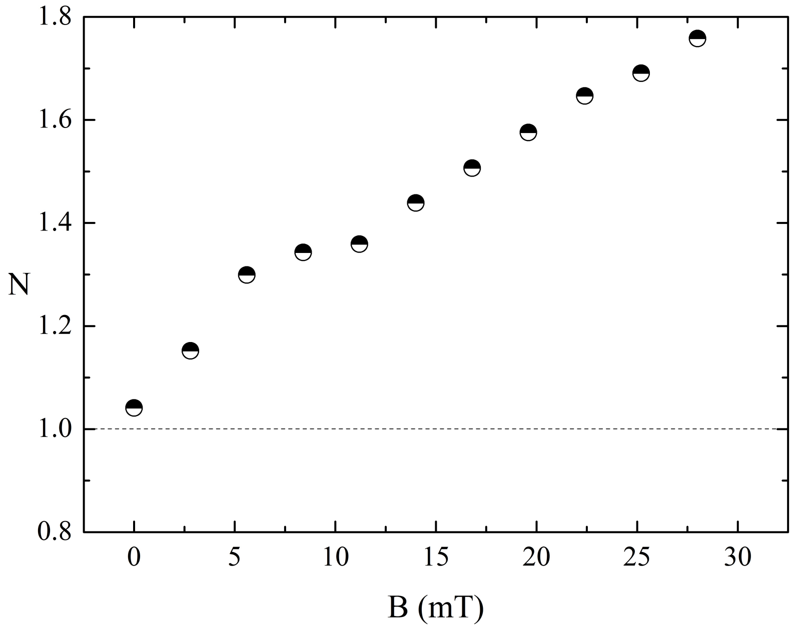

Figure 2.22: Density Ratio N Vs B-field. The Ratio N is averaged over 12 RF power levels

et.al [51]. However, contrary to the aforementioned results, Coulette and Manfreid [52] using kinetic simulations obtained that the Bohm velocity can be subsonic; whereas the α tends to increase because of lower space charge density near the wall. Thus if we assume that the product αU_b is independent of B-field; then it becomes evident that the increasing discrepancy in N-factor with B-field is due to error in current collection area of the cylindrical probe A.

To obtain the plasma density from Eq.2.8; the area A is taken as a constant under thin-sheath approximation with radius of the probe R_p used to calculate the Area A. However, if the sheath width around the probe tends to increase with B-field; then we would be underestimating the actual current collection area leading to over-estimation in the plasma density. Consequently, the estimated sheath width for the magnetized plasma at 28.0 mT may be about 1.75 times the un-magnetized sheath width. While, we have not explicitly quantified the effect of B-field on the sheath widths; which is in itself an involved study, nevertheless the experimental data in many experimental works [51] [53] [54] shows that the sheath width indeed increases with B-field.

Ultimately, we can state that the hybrid probe can be conveniently used to diagnose the RF plasmas in the Cylindrical CCP system and it has been used as a primary diagnostics tool in the Chapter-6.

2.4 Summary

To summarize this chapter, we discussed the two plasma systems (a) parallel plate setup and (b) cylindrical electrode geometry, designed for investigating the magnetization effects on a CCRF plasma discharge intended for specific applications. In both the systems the magnetic field remains tangential to the electrode surface. This can give rise to the $\vec{E} \times \vec{B}$ drifts in the systems. A detail description of the plasma diagnostic, particularly the hybrid probe technique applied in the present experiment has been subsequently provided. These techniques will be used in combination with the non-invasive electrical impedance measurements for the comprehensive understanding of the plasma systems.

Chapter 3

RF Power coupling, Impedance Matching and measurements

This chapter presents in detail the peripheral circuitry to transfer the RF power from the generator to the discharge electrodes. The primary objective of this circuit is to operate the plasma in a symmetric push-pull configuration to study the magnetization effect through impedance measurement. Hence, the power is coupled via a 1:1 isolation transformer or a commercial power splitter. The detail configurations of circuits are discussed in the subsequent sections.

The chapter also discusses the impedance matching for maximum power transfer to the plasma load; which is an important consideration for any RF discharge. Moreover, a detailed Fast-Fourier Transform based calibration technique is presented to accurately measure the Power/Phase of the plasma load from the external Voltage/Current probes. This in-turn is used to obtain the impedance measurement of the discharge; subsequent to calibration of the experimental setup.

3.1 Introduction

Power deposition inside the plasma volume is maintained through the RF current passing through the volume of discharge. This current is conserved at both the electrodes and if the two electrode are dissimilar in area ($A_a > A_b$); then the sheath at both the electrodes also becomes dissimilar ($s_a < s_b$). For the constant ion density model of the sheaths; this comes out to be [11];

$$s_a A_a = s_b A_b \tag{3.1}$$

Eq:3.1 signifies that the positive charge in both the sheaths is equal $Q_a = Q_b$. Therefore, if follows that

$$C_a V_a = C_b V_b \tag{3.2}$$

Where C_a and C_b are the sheath capacitance and V_a and V_b are the voltage drop across the sheaths. Hence,

$$\frac{\epsilon_0 A_a}{s_a} V_a = \frac{\epsilon_0 A_b}{s_b} V_b \tag{3.3}$$

Therefore;

$$\frac{A_a}{A_b} = \frac{V_b}{V_a} \times \frac{s_a}{s_b} \tag{3.4}$$

Substituting Eq: 3.1 in the Eq: 3.4 we have;

$$\frac{V_b}{V_a} = (\frac{A_a}{A_b})^2 \tag{3.5}$$

From, Eq: 3.5; the potential drop across the smaller electrode is

$$V_b = (\frac{A_a}{A_b})^2 \times V_a \tag{3.6}$$

Therefore, one can achieve a significantly higher potential drop across the smaller electrode by varying the dissimilarity of the two electrodes. This type of discharges is known as asymmetric discharges referring to asymmetry in the electrode areas. This configura-

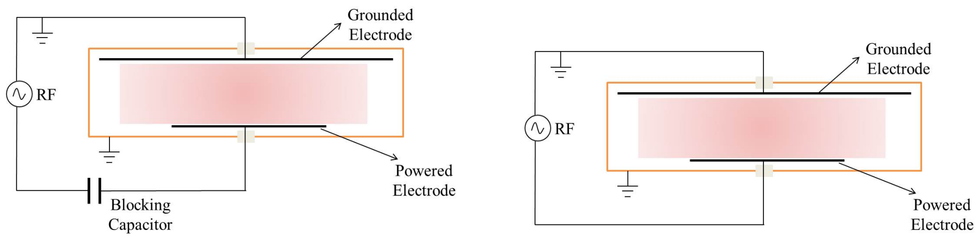

(a) Capacitive Coupled (b) DC Coupled

Figure 3.1: Coupling scheme for a CCRF discharge

tion is used during plasma processing to provide higher ion bombardment at the substrate [55]. Power coupling schemes to deliver RF power to a CCRF plasma discharge is therefore an important phase of designing a processing reactor. The coupling scheme as well as the discharge symmetry varies depending on the processing requirement. The external magnetic field can also introduce a discharge asymmetry in a geometrically symmetric CCRF discharge [56].

The effect of different potential drops across the two sheaths changes the plasma depending on the power coupling scheme used in the setup. The RF power to a CCRF discharge may be coupled in two methods; 1) Capacitive Coupled and 2) DC Coupled. These two are shown in Fig 3.1

Fig 3.1a shows the capacitive coupled scheme; which is the most commonly used setup in plasma processing reactor. The grounded electrode is larger in area than the bottom or the live electrode where substrate is kept. The blocking capacitor in the circuit prevents the net dc current to be flown through the discharge. Fig 3.1b is the DC coupled scheme, in this scheme the blocking capacitor is removed as the two electrodes remain shorted through the power supply and therefore a net DC current can flow through the plasma.

For the capacitive coupled scheme, the higher potential drop in the smaller sheath for asymmetric discharge charges the blocking capacitor to a DC bias corresponding to;

$$V_{DC} = V_b - V_a = V_b[1 - (\frac{A_b}{A_a})^2] \tag{3.7}$$

Therefore, in this configuration, the smaller electrode becomes negatively biased by V_{DC}. While for the DC coupled case, as the two electrodes are shorted and remain at the same time averaged potential, a DC bias voltage cannot sustain in this configuration. However, since a DC current is allowed to flow; a DC current corresponding to V_{DC} flows through the plasma leading to discharge current being a combination of RF and DC currents. This phenomenon of DC current through RF plasma is known as the battery effect [1] as the dissimilar potential drops across the two sheaths act as a DC battery in series with the RF power supply.

Eq: 3.7 was based on the constant ion density sheath models; while for a more accurate inhomogeneous sheath model instead of the constant ion density; we have [16]

$$\frac{A_b}{A_a} = (\frac{s_a}{s_b})^{1/3} \tag{3.8}$$

This dependency also leads to higher potential drop across the smaller electrode with value of V_{DC} different from the equations derived before in Eq:3.7 however; the effect of asymmetry remains the same for both the coupling scheme.

Therefore, in an asymmetric discharge, the effects of DC bias or current would always be associated along with the RF current. The DC effects in the discharge would lead to asymmetric drifts near the sheaths or inside the plasma in presence of B-field. Hence in order to avoid these effects and to study the effect of magnetic field, we prefer to choose electrode configuration in which the plate area is geometrically same. Furthermore, to maintain the electrical symmetry we drive the plasma discharge in push-pull configuration; where both the electrodes are driven by out of phase RF potentials simultaneously. This configuration avoids stray grounded electrodes (for eg: Probe shafts) exposed to the plasma; participating in the discharge. Such a configuration is achieved by DC coupling the plasma electrodes through a 1:1 isolation transformer or by commercial RF power splitter as shown in Fig 3.2

The complete circuit for power delivery is shown for the parallel plate setup; here we have two symmetric electrodes driven through a specially designed 1:1 ferrite isolation transformer. The primary of the transformer is fed RF power from the RF generator through the impedance match box. The impedance of the discharge load is measured by the Voltage/Current probe placed very close to the electrodes outside the vacuum chamber to infer the magnetization effects on a CCRF plasma discharge

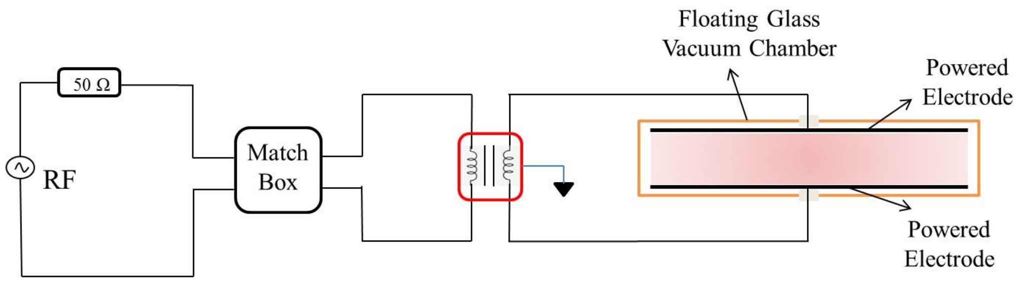

Figure 3.2: RF power delivery scheme for parallel plate setup

Advantages of operating a CCRF plasma discharge in symmetric push-pull configuration are listed below;

1. The DC current/bias effects on the impedance and plasma characterization are avoided.
2. The RF current path is well-defined by avoiding multiple grounded surfaces in the plasma. This also ensures the plasma discharge is also well-defined between the electrodes.
3. Proper return current to the generator is ensured.
4. RF Power measurements by the Voltage/Current probes near the electrodes become simpler because of well-defined current path through the plasma.

For the cylindrical CCP experimental setup the discharge is driven in push-pull configuration with the help of a commercial power splitter instead of the 1:1 isolation transformer. The power splitter drives the set of electrodes 180^0 out of phase to each other with respect to the RF ground. The power splitter keeps the electrodes DC shorted and therefore in this case also the out of phase voltage on the geometrically symmetric electrodes with respect to the same RF ground keeps the discharge electrically symmetric. To validate

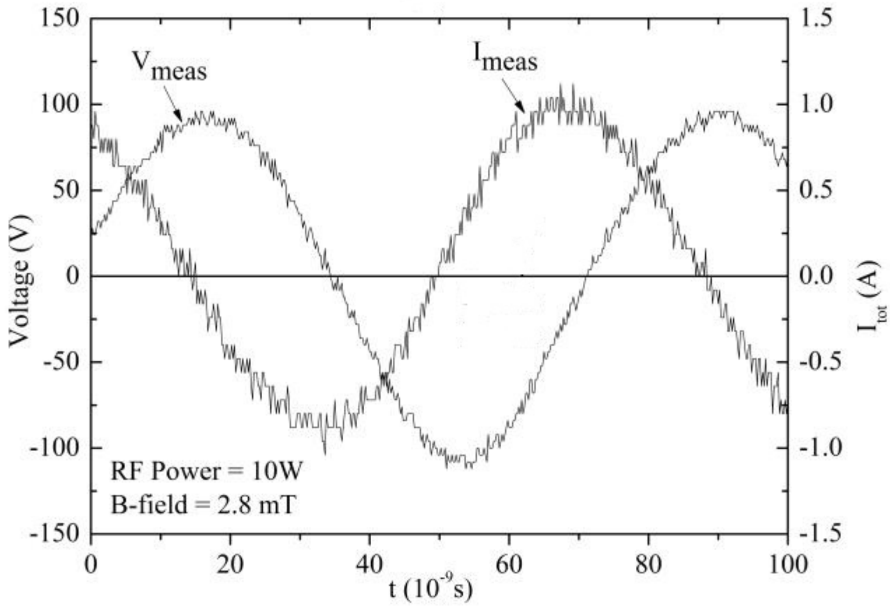

Figure 3.3: Sample Discharge Voltage/Current Waveform for the symmetric CCRF plasma discharge

the electrical symmetry of the both the discharge; we must measure the DC current flowing through the discharge, corresponding to the battery effect induced by any electrical asymmetry in the discharge electrodes. A sample of voltage/current waveforms for the plasma discharge is shown in Fig 3.3. Fig 3.3 shows a negligible DC offset in the current measurement. This confirms that the battery effect in both the setup is negligible. Therefore, both the experimental systems are considered to be electrically symmetric. It is also known that the asymmetry in the discharge creates harmonic frequency components in the plasma [57]. These components can be observed in the FFT of the Current signal. A sample FFT of the current signal in Fig 3.4 for the cylindrical setup shows that the fundamental frequency remains dominant while, the second harmonic is comparatively insignificant. This result also confirms the symmetry of the discharge.

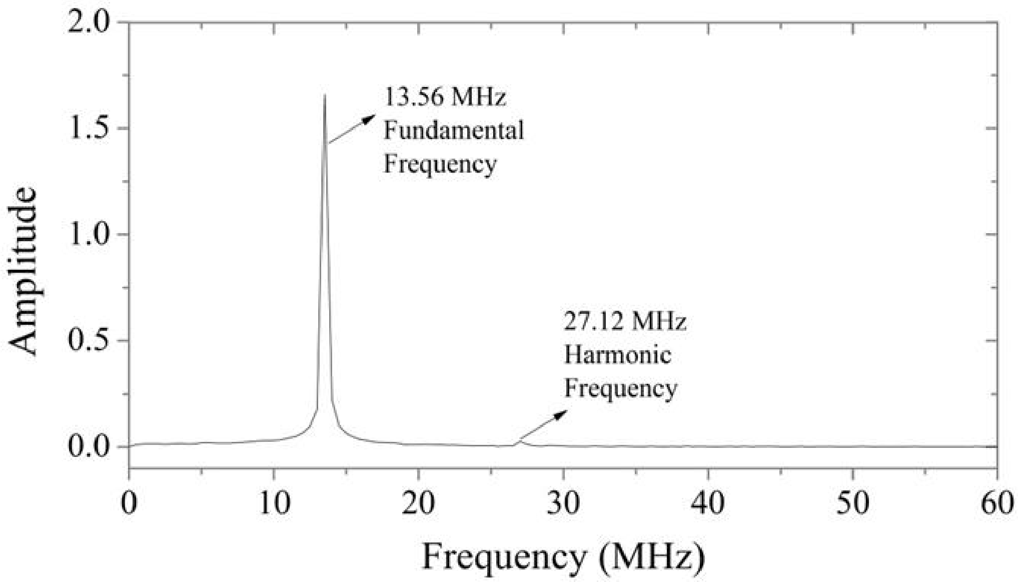

Figure 3.4: FFT of the current waveform

3.2 1:1 Ferrite isolation transformer/Power Splitter for Push-Pull Configuration

As discussed in the previous section, the push-pull configuration for the CCRF discharge is achieved by ferrite transformer or a commercial power splitter. These are designed to have minimum losses for 13.56 MHz power transmission.

1) 1:1 Ferrite Isolation Transformer

A national magnetics M2 toroidal core is used to make this transformer. The material specifications are attached in the appendix. This material is NiZn based ferrite with initial permeability $\mu_i = 40$ typically used for high frequency applications upto 50 MHz. The core dimensions are OD=3.175 cm, ID=1.905 cm and thickness=0.9525cm. To design the transformer; we estimate the potential on the electrodes for the experimental RF power regime to be less than 400V. Therefore, considering discharge voltage = 400V as the input parameter the potential across the primary/secondary side of the transformer will be given as [58];

$$V = 400 = 4.44 fABN \tag{3.9}$$

(a) Ferrite core (b) 10 core Transformer

Figure 3.5: 1:1 Ferrite Transformer

Where, f – Freq. of operation = 13.56 MHz, A – Cross-section for magnetic flux, B – Magnetic flux density and N – No. of turns. Substituting all the values we get;

$$ABN = 6.64 \times 10^{-6} \tag{3.10}$$

For the given dimension of the core, the cross-section area of $1core = 1.20cm^2$. We take 10 such cores to make the transformer and for the available ID of 1.905 cm; it is possible to have N=4 turns through the core. Therefore inserting these values in the above Eq:3.10 we get;

$$B = 1.38mT = 13.8Gauss \tag{3.11}$$

This value of 13.8 Gauss is about 0.7% of the saturation flux density of 2300 Gauss for material M2. The number of turns N=4 is decided by the estimated current to the plasma. For the experimental power regime, we consider this to be always less than 4.0 A hence a multi-strand copper wire of cross-section $4.0mm^2$ is used for windings.

Considering this design parameters for the transformer; the core losses are likely to be negligible as we are operating at very low flux densities for the material; while the copper losses in windings are carefully minimized by taking a conservative current density of $1A/mm^2$. We also chose teflon shielded multi-strand copper wires; which reduces the

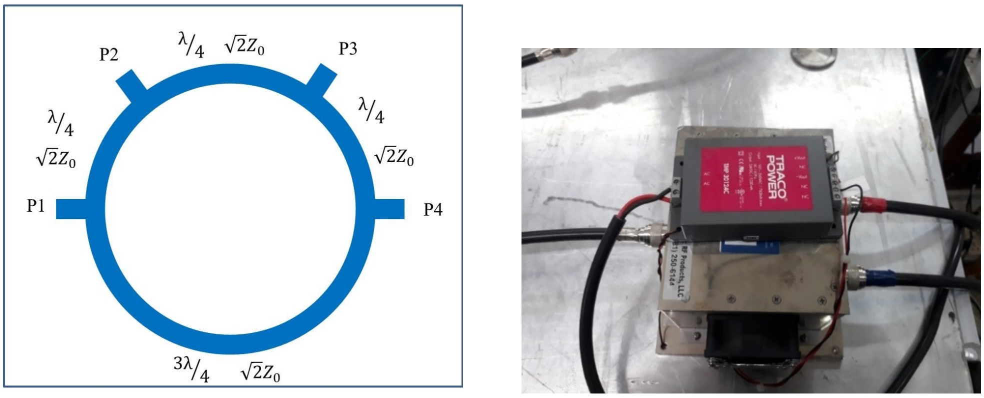

(a) Rat-Race Design (b) Hybrid Coupler

Figure 3.6: Nortec Rat-Race Hybrid Coupler

resistance ($\backslash loss$) of the winding by minimizing the skin effects on the conductor at 13.56 MHz.

2) Commercial Power Splitter

A specially designed power splitter is procured (from Nortec-RF) to deliver 180^0 out of phase potentials to the electrodes in the cylindrical CCP. It is a Rat-Race hybrid power splitter [59]; with one input port (Port-P1) and two output ports (Port-P2, and P4) and the fourth port (P3) is terminated internally through a 50 Ω resistance to ground. The transmission circuit is designed to have a characteristic impedance $\sqrt{2}Z_0$ where $Z_0 = 50\Omega$ and the overall transmission length of the rat-race is $3/2\lambda$. This configuration gives 180^0 ($\lambda/2$ length between them) out of phase potentials at ports (P2 and P4); with isolation between these two ports at the fundamental frequency. The configuration also provides equal power sharing between them for perfectly matched loads with P3 terminated at 50Ω load. This circuit is typically used for GHz range frequencies in micro-strips. However, similar configuration is achieved in manageable size for 13.56 MHz by using ferrite based inductors/transformers in the circuit instead of the actual transmission lines (micro-strips) as used in GHz range. About 3% power is lost in this passive device for driving the electrodes in push-pull configurations. Detail workings of the Rat-Race power couplers/Splitters are available in various resources [59] and are not delved into.

The specifications of the commercial power splitter designed at 13.56 MHz are tabulated in Table 3.1;

Description	1200W, 13.56 MHz, 2-way 180-degree Divider
Power	1200 W
Frequency	13.56 MHz
Insertion Loss (Typical/Max)	0.2 dB/0.25 dB
Isolation (Typical/Max)	27 dB/25 dB
VSWR (Typical/Max)	1.15/1.2

Table 3.1: Specifications of the hybrid Power Splitter

3.3 Impedance matching

To efficiently deliver RF power to a complex load such as plasma at 13.56 MHz, impedance matching becomes important dynamic part of the plasma discharge circuit. Impedance matching in simple terms is manipulation of the driving/driven circuit impedance to ensure a condition of no reflected power from the driven load (Plasma). Most RF power supplies as used in these experiments are designed to have 50 Ω (Source) impedances and the co-axial cables delivering the RF power also have the characteristic impedance of 50 Ω. The driven load (Plasma) on the other hand can have any impedance value depending upon the discharge Voltage/Current/Gas Pressure/Magnetic field etc. Therefore, it becomes mandatory to introduce matching networks; which could alter the impedances in the circuit to have good matching conditions.

3.3.1 Maximum Power Transfer and L-Type matching network

The fundamental of impedance matching is derived from the maximum power transfer theorem. This theorem states that for a Thevenin equivalent circuit of a complex electrical load like plasma, maximum power to the load will be delivered when the source side impedance is complex conjugate of the driven electrical load. Consider the circuit in Fig 3.7a for driving a plasma load; where we have the source side impedance of 50 Ω driving the discharge load through the L-Type matching circuit. The steps for matching in a L-Type network are as follows;

1) Matching the Real Part of impedance

If we suppose for a capacitive plasma side load of 2-j10 Ω; the Thevenins equivalent circuit becomes as shown in Fig 3.7b. Now, the matching network must alter the load/source side impedance such that the load and source side impedance are complex conjugates of each other. This manipulation is achieved through changing the L (Load) and T (Tune) capacitor values in the matching unit. As shown in Fig 3.7b, the L capacitor is in parallel to the Source side impedance of 50 Ω . Therefore, the capacitor L will maneuver to a value such that the real part of the parallel combination of the 50 Ω and the L-capacitor matches to real value of the plasma side impedance of 2 Ω i.e.;

$$Re[\frac{-j50X_L}{50 - jX_L}] = 2 \tag{3.12}$$

Solving Eq: 3.12; we get $X_L = 10.2\Omega$; with Capacitance of L = 1.1 nF; while the complex part of this parallel combination gives value of -j99.88 Ω. Hence now, the circuit becomes as shown in Fig 3.7c

2) Matching the Reactive part of the impedance.

In the circuit shown in Fig 3.7c the real parts of both the source side and the plasma side is equal; while the complex part are not. To obtain the condition of maximum power transfer; the source side reactance value must be complex conjugate of plasma load side i.e.

$$-j99.88 + jX_{coil} - jX_T = +j10 \tag{3.13}$$

Here, the X_{coil} is a fixed inductor coil; while X_T is variable. Therefore, X_T settles at a value to satisfy this Eq:3.13 to give a matched circuit condition.

There are different types of matching networks such as L-type/T-type or a π-type to re-

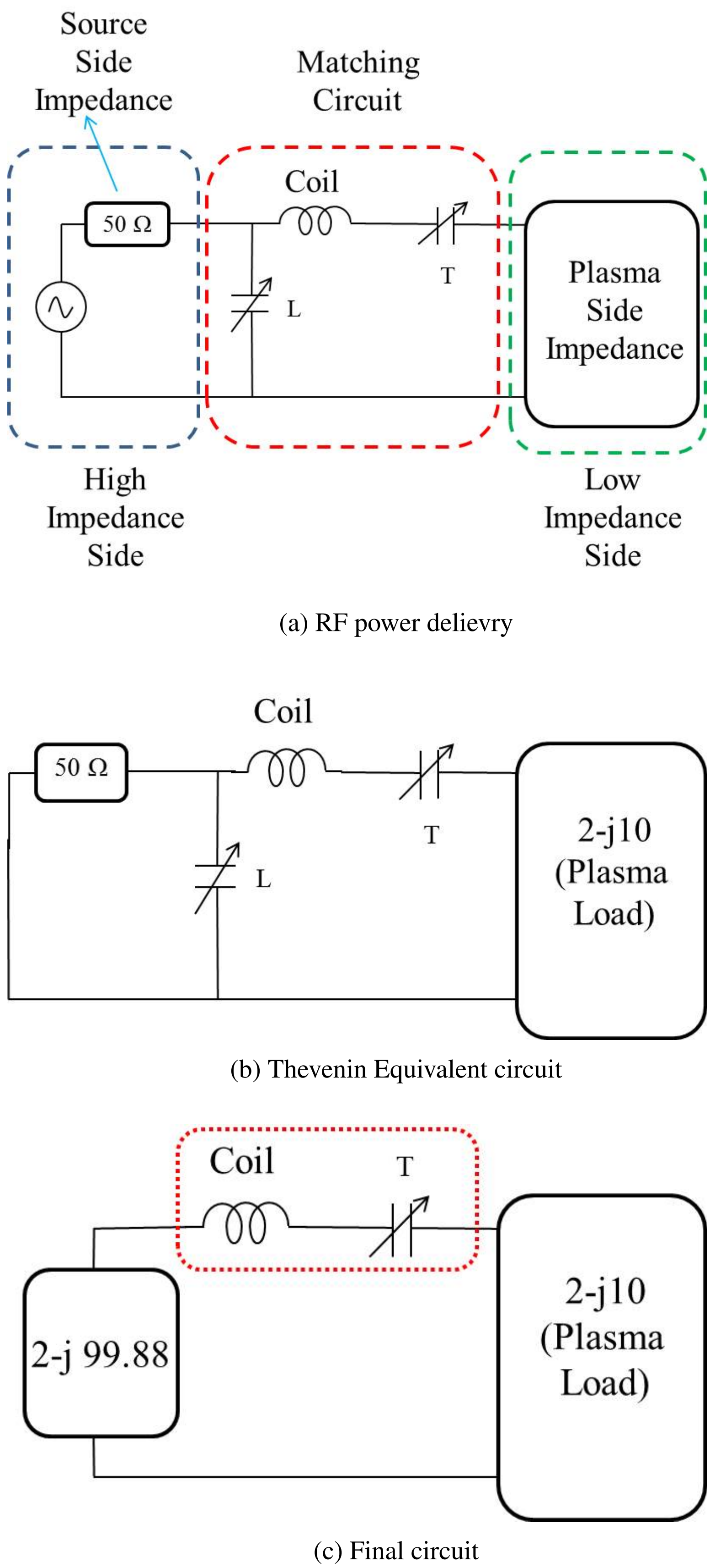

Figure 3.7: RF power delivery scheme through L-Type matching network

alize a matched load. Each type of network has its advantages and operating regimes in terms of impedance matching. Significant literatures on each matching networks and their advantages are available [59] and therefore here we are only focused on the L-Type network used in this experimental study,

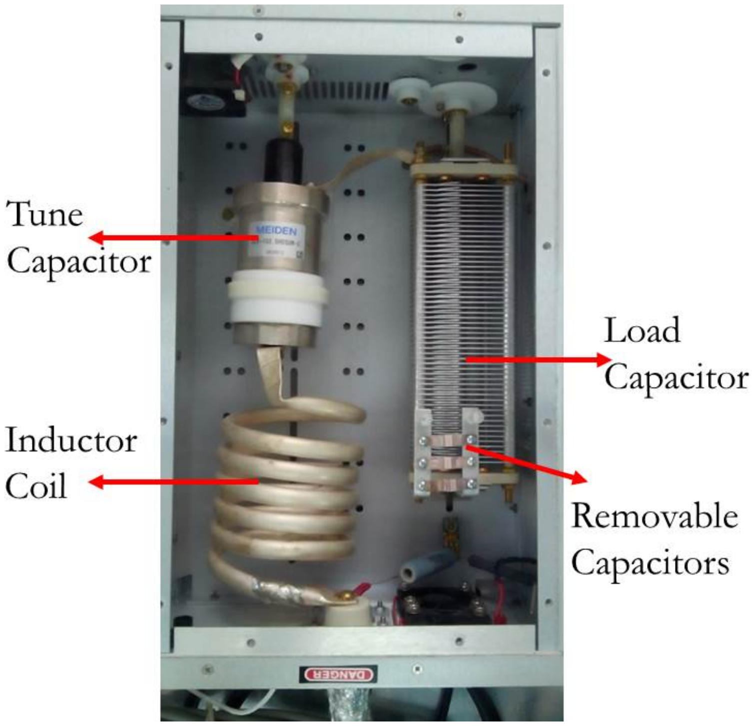

Figure 3.8: Actual matching network with all its components (AIT-600R)

The Matching network used in the experiments is an L-type network (AIT-600R, T & C Power Conversion) with a RF power generator of 1.2 KW (50 Ω, T & C Power Conversion). This matching network is designed such that it can match to plasma loads with real part of impedances less than 50 Ω i.e. High impedance side of the matching network is the source side of 50 Ω; while the low impedance side is the discharge load. As shown in Fig 3.7a and discussed in the example, the Load (L) capacitor on the source side can match the real part of the load (Plasma) side impedance by varying the capacitance of variable L capacitor. Now to attain a condition of cancelling imaginary parts of load and source side reactance (Complex conjugates), a fixed inductor and a variable Tune (T) in series are present. The Tune (T) capacitor achieves a value which can complement capacitive/inductive plasma side load with an inductive/capacitive reactance to the circuit.

This process of matching (Varying Capacitor values) is done automatically via feedback control mechanisms between the RF generator and the matching network; where T can vary from 50 to 350 pF and L can vary from 100 to 1000 pF with three fixed capacitor (240 pF each) that can be added/removed from the circuit.

3.3.2 Electrical Equivalent Circuit of an actual CCRF plasma setup

As seen in first chapter, a CCRF plasma load is analogous to an R-L-C series load. Yet, this analogy does not consider any stray impedance loading effects on the overall impedance seen by the matching network. Any large experimental setup as used in this thesis will always introduce external parallel stray capacitive reactance to the plasma due to transmission lines, vacuum feed-through etc. Ideally, an experimental setup must be designed to have minimum stray capacitances (few pico Farads → Open circuit at 13.56 MHz) such that their effect on the load side impedance could be ignored [60]. However, such stringent conditions of low stray capacitance are rarely achieved in the practical experimental/industrial setups with stray capacitances in the range of few 100s of pico-farads. Consequently, any actual equivalent circuit of a CCRF plasma load must include a stray capacitive reactance in parallel to the R-L-C plasma load as shown in Fig 3.9. Therefore for the matching network the load side impedance is the parallel combination of the R-L-C series discharge load and the stray capacitance of the setup.

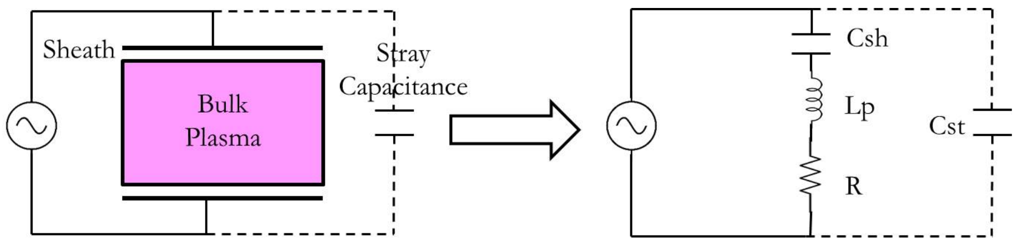

Figure 3.9: Actual CCRF plasma load as seen by the matching unit

3.4 Supplementary matching techniques

As discussed previously, the Tune (T) and Load (L) capacitors value changes to obtain impedance match. However, these variable capacitors have fixed range of values that they can maneuver in; which limits the load (discharge) impedance that can be matched by the network. The operating range of the automatic tuner used in the experiments is as presented in Fig 3.10. The resistive range of the network is from 1.8 Ω to 25 Ω; while the reactive range is from -80^0 to $+60^0$ normalized to 50 Ω.

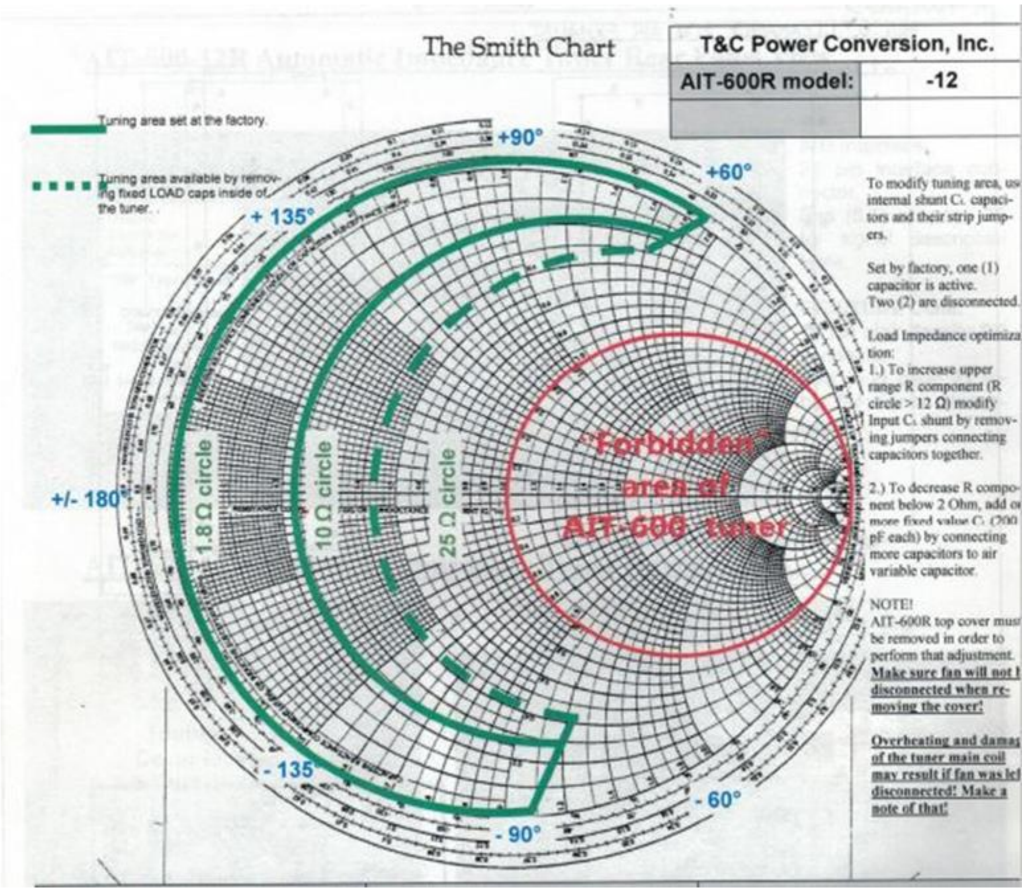

Figure 3.10: Matching network operating range

Since, in an actual experimental setup,the matching range is determined not only by the plasma load but also the stray loads which acts in parallel to the plasma load. Therefore, it may not be necessary that the overall load (Plasma) side lies inside the operating regime of the matching network and hence, different procedures to obtain a good match must be employed. We used a modest method based on trial and error of introducing different length of transmission line coax cables (0.5/1.0 and 2.0 m) from the matching unit to the power splitter/the 1:1 isolation transformer to alter the stray reactance seen by the matching unit. A RG-213 (Technical data-sheet in Appendix) cable introduces about 100 pF (≈ -j117 Ω) of capacitance in parallel for 1.0 m length of cable; therefore altering the impedance seen by the matching unit. Fig 3.11 shows the block diagram of complete RF power delivery scheme as we examine the effect of introducing different cable lengths. The effect of transmission lines on the impedance seen by the matching network can be

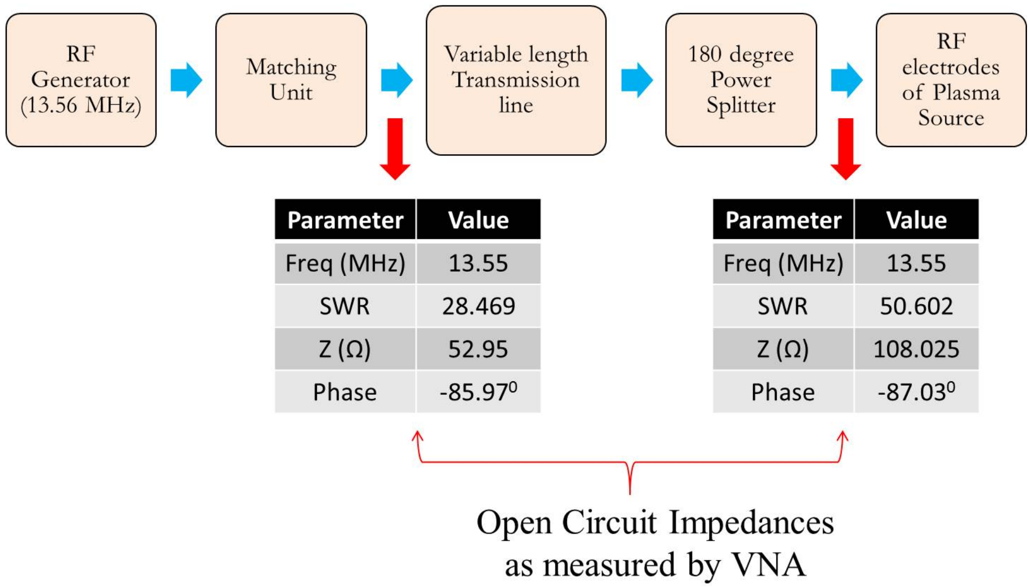

Parameter	Value
Freq (MHz)	13.55
SWR	28.469
Z (Ω)	52.95
Phase	-85.97^0

Parameter	Value
Freq (MHz)	13.55
SWR	50.602
Z (Ω)	108.025
Phase	-87.03^0

Figure 3.11: Power delivery to the Cylindrical CCRF plasma setup

understood from Fig 3.11. Here, we used a Vector Network Analyzer (Array Solutions VNA-2180) to obtain the open circuit impedances (No plasma) at the discharge electrodes just outside the vacuum chamber and also at the matching unit terminals with 1.0 m transmission line from the power splitter. It is seen from the measurements that the open circuit impedances seen by the match-box (≈ 53Ω) is drastically different from the impedance at the electrode terminals (≈ 108Ω).

In presence of plasma the absolute values of impedance would change. However, the principle of altering impedance range still remains valid. This method is equivalent to introducing a capacitive load in parallel to the plasma and thus can be used to finely alter the matching range. However, a caveat of this method is that introducing primarily capacitive reactance in parallel would present a bypass path for the RF current. Therefore, one might draw higher current from the RF matching unit to deliver a fixed RF power; which becomes pertinent problem when operating discharge at higher powers.

3.5 Power, Phase and Plasma Impedance Measurements

The power measurement in RF discharge is critically important to obtain the discharge impedance of a CCRF discharge. This measurement is also highly sensitive to external circuit conditions. Various studies have shown methods to calculate the net RF power delivered to the discharge. In most cases, the actual power delivered in the plasma is calculated by finding the power lost in the matching unit and the transmission lines and then subtracting it from the onboard power measurement reading. Traditionally measurements in RF systems have been performed by accounting the difference in the forward and the reflected power displayed by the on panel power meter considering that the matching unit works with minimum loss of power. However, the losses in the matching unit and the transmission lines could be up to 90 % of the total power [61], which could render any measurement useless. Many authors have shown that this consideration is not valid for various conditions, the wasted power changes with the RF power [60] [62], the excitation frequency [63], with gas pressure [64] [65] [66], matching network topology [63] [67] the gas mixture [64] [62] [68], the reactor design [69] and the electrode gap [69].

A robust approach is the one wherein the power is inferred from the phase measurements between the Voltage (V) and the current (I) waveform at the electrodes by the equation $P_{dis} = V_{rms} I_{rms} cos\phi$. Although the phase measurement technique is accurate, its practical application is difficult due to several factors influencing the actual phase measured between the RF voltage and current signals. At higher frequencies there are uncertainties which creep into the phase measurement due to the physical lengths of the coax cable of the measuring voltage/ current probes (at freq. of operation) which give rise to characteristic delay in the signal transmission. Any mismatch in the delay between the 2 probes (Voltage/Current probes) causes the phase measured in the Digital Storage Oscilloscope (DSO) to be inaccurate. Therefore it is essential to calibrate the voltage/current probes used for the RF power measurement.

3.5.1 Calibration Procedure

To account for, and eliminate the phase delay introduced by the transmission lines of the voltage/current probes; we compare the phase measured in DSO (Digital storage oscilloscope) by the voltage/current probe signals to the phase obtained by characterizing the same electrical load with help of a vector network analyzer [70]. Fig 3.12 shows the probe calibration setup. In this setup we have a non-inductive 50 Ω dummy load connected to the secondary side of a 1:1 transformer as the load for comparing the phase measurements by two methods. The phase data obtained by the measuring probes are determined by sup-

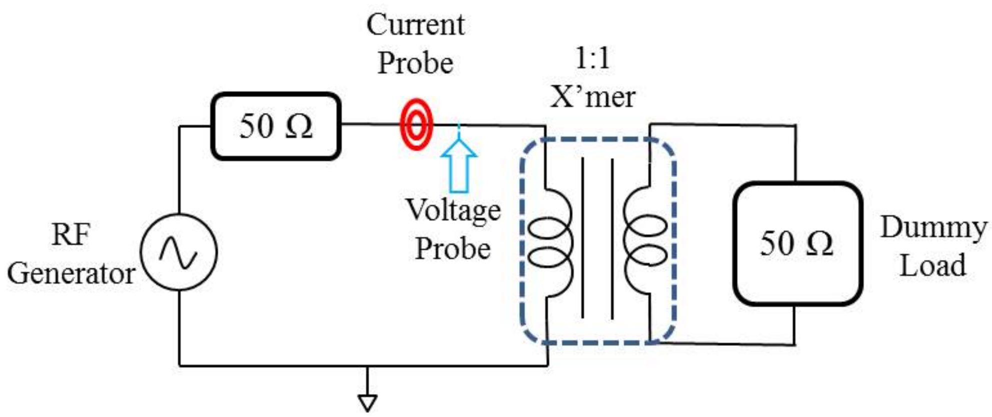

Figure 3.12: Probe Calibration Setup

plying a small $\sim 5W$ power from the RF generator (without matching unit) to the primary of the 1:1 ferrite transformer. The phase between RF voltage and the current is captured in DSO (Tektronix TDS 3034C). The RF voltage waveform is obtained by Tektronix high voltage probes (TEK P6015A) with a bandwidth of 75 MHz while; the current waveform was measured using a current transformer (ion physics CT). The CT has sensitivity of 1 V/A (CM-100-M) with 50 MHz bandwidth.

The process is repeated by replacing the RF generator with a VNA network (Array solutions VNA 2180). The VNA provides the total impedance of the combined load i.e inductive (1:1 transformer) plus the resistive 50 Ω dummy load corresponding 13.56 MHz, the results of VNA are presented in Table 3.2 For comparison, Table 3.3 shows the corresponding phase difference obtained with VNA and those obtained from the voltage and the current waveform based on FFT analysis. The phase difference between voltage and current measured by probe is found to be smaller than those obtained from VNA by 18.89^0. This difference is now taken as the calibrating factor for all phase measurements in the thesis with the same Voltage/Current probe setup.

Parameters	**Data from VNA at 13.56 MHz**
$RealImpedanceR_s$	$187.07 \pm 0.03\Omega$
$ImaginaryImpedanceX_s$	$101.59 \pm 0.04\Omega$
Phase $tan^{-1}(X_s/R_s)$	28.25 ± 0.02^0
$\%Reflection$	44%

Table 3.2: Load characterization by VNA

Analysis Method	**Phase (By VNA)**	**Phase (By DSO)**	**Calibrating Factor**
FFT	28.25 ± 0.02^0	9.36 ± 0.05^0	18.89 ± 0.053^0

Table 3.3: Calibrating factor for FFT method

3.5.2 Fast-Fourier Analysis of the voltage/Current waveform

The data of the voltage/current waveform obtained by the DSO must be analyzed to get the phase measurement from it. A time-domain based method is inept for accurate phase measurements as the sampling rate of the DSO was 5.0 GS/sec; which corresponds to 0.2 nsec in time. Now, for a 74 nsec waveform at 13.56 MHz, 0.2 nsec corresponds to 0.94^0 resolution in phase. This resolution is too large to accurately measure the phase;

especially for CCRF discharges which could be strongly capacitive in nature and will lead to significant errors in the power/phase measurements. Therefore, a Fast-Fourier Transform (FFT) based analysis method is used for this process. This method is reliable and has been used to obtain highly accurate phase measurements with error in phase measurement of the order of 0.02^0 [61].

The frequency domain outcomes of the voltage and current waveform after FFT analysis gives phase values at different frequency steps (Δf). The phase value for each voltage/current waveform at the fundamental frequency (13.56 MHz) is actually the phase of the waveform w.r.to an ideal cosine wave of same frequency (13.56 MHz). Therefore, the measured phase between the voltage/current waveforms in time-domain is essentially the difference between the phase values obtained in frequency domain at the fundamental frequency (f=13.56 MHz). This method eliminates the zero crossing errors usually present in time domain methods [59]. Errors due to the harmonic content in the waveform is also suppressed as this method gives the phase between the voltage and current only for the fundamental frequency, removing the effect on phase measurement due to presence of higher frequency components [59].

To obtain the signal waveforms, through-out the experimental study the bandwidth of the oscilloscope was set to 20 MHz to avoid unwanted high frequency noise, while N=10000 data points (Horizontal resolution) have been captured at sampling rate of 5 GS/s ($\Delta t = 0.2nsec$). Based on these settings in DSO the frequency steps in frequency domain in FFT of the signals would be given by;

$$\Delta f = \frac{1}{N\Delta t} = 0.5MHz \tag{3.14}$$

Therefore, the fundamental frequency in this case for the data analysis is considered to be 13.5 MHz; which is closest frequency step to 13.56 MHz.

3.5.3 Actual RF power measurements by calibrated probes

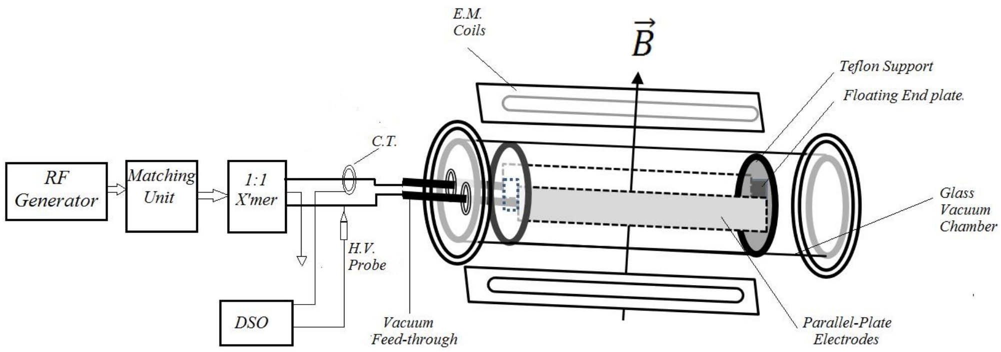

Figure 3.13: Schematic of the experimental and RF power delivery set-up

Fig 3.13 shows the parallel plate experimental setup with the RF power delivery and RF power measurement setup. We measure the voltage across the two electrodes with the help of high voltage probe (TEK P6015A) while current is measured by a current transformer (CM-100-M) of ion-physics. In this setup, the discharge voltage (V_{rms}) is the potential difference between the two electrodes. The two voltage signals and the current signal are acquired on the DSO (Digital Storage Oscilloscope-Tektronix TDS – 3034C). The RF power delivered to the plasma is then obtained by analyzing the signals as discussed in the preceding sections and obtaining the phase between the voltage and current signals by $P_{dis} = V_{rms}I_{rms}cos\phi$.

These readings are compared with the on-board power meter reading (RF power = Forward-Reflected power) on the RF generator for different neutral gas pressures, magnetized and un-magnetized plasma and plotted in Fig 3.14. It is seen that the reading of the on-board meter and the probe measured power matches very well for the un-magnetized plasma at 1.0 Pa neutral argon gas pressure. For, this case, the RF generator shows zero reflected power reading as matching is conveniently achieved. However, when the magnetic field is introduced into the CCRF plasma; we observe very high reflection values of about 60 % of the set RF power. In this case the measurement reading of the on-board power meter is seen to over-estimate the delivered RF power. Higher reflection from the plasma load leads to higher transmission losses in the Match box, 1:1 transformer, and transmission coax-line and therefore the actual power delivered to the plasma is less than the on-board power meter readings. As a result, we depend on the calibrated probe measured power readings.

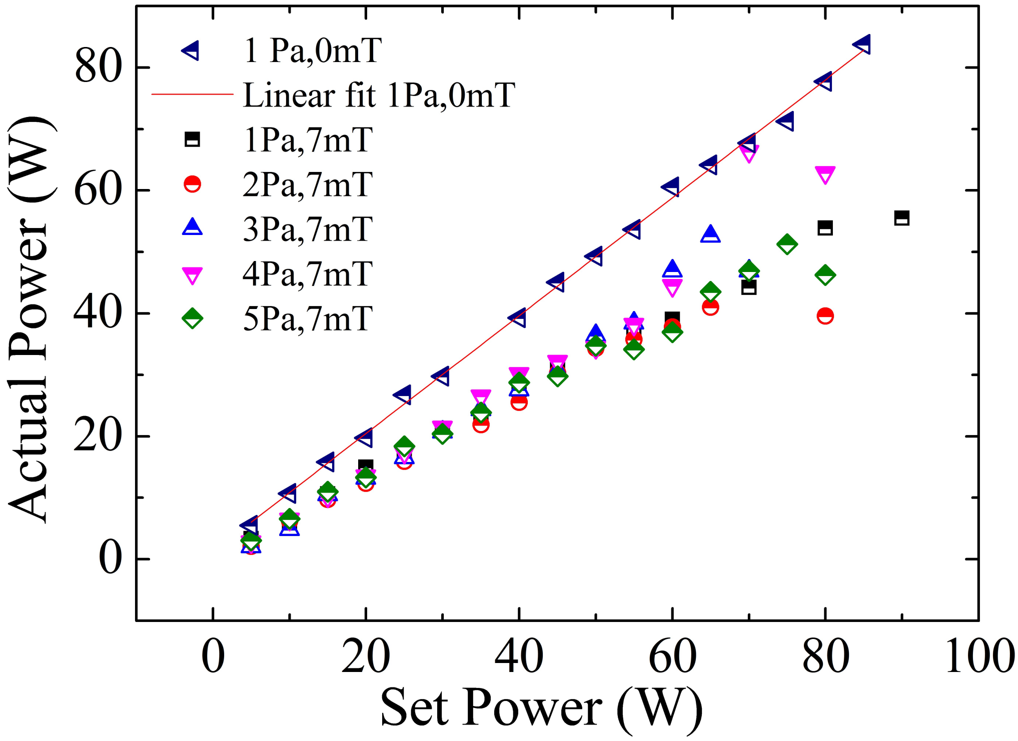

Figure 3.14: Set power Vs Actual power for a range of pressures for B = 7.0mT and at 1 Pa for magnetic field B = 0 mT . *The solid line is a linear fit (slope = 0.94) to the data corresponding to 1Pa,0mT*

3.5.4 Experimental setup Calibration for accurate impedance measurements

From the measured RF power by $P_{dis} = V_{rms}I_{rms}cos\phi$; discharge impedance can be obtained from the equivalent electrical circuit diagram of a CCRF discharge as presented in Fig 3.9. The circuit diagram shows the typical R-L-C series circuit of plasma discharge load in parallel to a stray capacitive reactance. This circuit can then be simplified from Fig 3.9 to Fig 3.15. As seen in Fig 3.15, the RF current measured externally by the current transformer is divided in two branches; while the measured phase between the Voltage

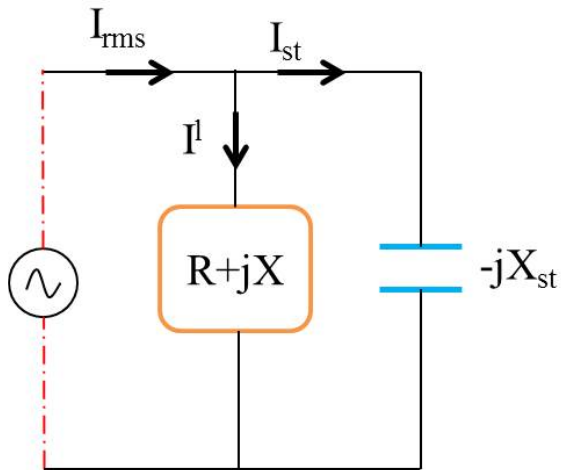

Figure 3.15: Equivalent Circuit of the discharge load in parallel with stray capacitance

and Current external to the vacuum chamber is also indicative of the parallel combination of the R-L-C series discharge load and the stray capacitive loading. It is therefore necessary to eliminate the effect of C_{st} on the impedance measurements which must show the discharge impedance only.

In view of the above discussion, the rms current measured by the current probe shown in Fig 3.15 is $I_{rms} = I' + I_{st}$ where I' represents the component of RF current flowing through the plasma and I_{st} is the current by-passed through C_{st}.

Therefore, the externally measured total impedance Z_{tot} of the discharge circuit is obtained as [70];

$$Z_{tot} = \frac{RX_{st}^2}{R^2 + (X - X_{st})^2} + j\frac{-XX_{st}(X - X_{st}) - R^2 X_{st}}{R^2 + (X - X_{st})^2} \tag{3.15}$$

In Eq;3.15, $X = (X_p - X_{sh})$ is the net reactance where $X_p = \omega_{rf} L_p$ and $X_{sh} = 1/\omega_{rf} C_{sh}$ respectively; whereas, $X_{st} = 1/\omega_{rf} C_{st}$.

The real and imaginary components of Eq: 3.15 could be separated as;

$$Z_{tot} cos(\phi) = \frac{RX_{st}^2}{R^2 + (X - X_{st})^2} \tag{3.16}$$

$$Z_{tot} sin(\phi) = \frac{-XX_{st}(X - X_{st}) - R^2 X_{st}}{R^2 + (X - X_{st})^2} \tag{3.17}$$

The phase ϕ is the relative phase measured between V_{rms}, I_{rms} and $Z_{tot} = V_{rms}/I_{rms}$. To quantify the value of C_{st} a VNA (Vector Network Analyzer) has been used in the experiment. Vector network analyzer (Array solutions VNA-2180) characterizes the open circuited chamber load and gives an estimate of the stray capacitance of the experimental setup; which is used in the above Eq:3.16 and 3.17. With this information; the 3.16 and 3.17 can be solved simultaneously to determine values of R and X. From this the actual phase difference $\phi^{'}$ (i.e without the effect of stray capacitance Cst) between RF current $I^{'}$ (flowing through the plasma) and the RF voltage can be obtained as follows;

$$\phi^{'} = tan^{-1}(X/R) \tag{3.18}$$

Furthermore, the actual r.m.s current $I^{'}$ through the discharge can be estimated from;

$$I^{'} = \left(\frac{X_{st}}{\sqrt{R^2 + (X - X_{st})^2}} \right) \times I_{rms} \tag{3.19}$$

This procedure to obtain the real values of plasma current and the phase is critical in measurements; as for large discharge setups; the stray capacitance could be in few 100 picoFarads. At such values of C_{st}, the capacitive reactance in parallel with the discharge load becomes 100s of Ω at 13.56 MHz. Therefore, it is imperative, that the experimental setup along with the measuring probe be calibrated as discussed in the preceding sections of this chapter to ensure accurate measurement of the discharge impedance and the RF power delivered to the plasma load.

3.6 Summary

To summarize this chapter, we established power coupling scheme to create an electrically symmetric plasma discharge for two experimental setups by using 1:1 ferrite isolation transformer in the parallel plate setup and a commercial power splitter in the cylindrical electrode setup. The symmetry is verified through the current waveform and its FFT. Symmetric systems are preferred in this study to conveniently observe the global effects of magnetic field on the CCRF plasma through impedance measurements and avoid the DC current/Bias effects on the plasma.

The RF power/phase measurement is also a critical part of the present study to obtain the discharge impedance accurately. It was shown, that we can obtain the actual discharge impedance from the externally measured Voltage/Current and Phase measurements, if necessary steps are taken in calibration of the measuring instruments as well as the experimental setup.

Chapter 4

Power mode transitions in magnetized CCRF discharges

4.1 Introduction

As we have already discussed in chapter-1, that equivalent circuit of a CCRF discharge has many resistances ($R_{stoc}, R_{ohm,sh}, R_p$ and R_i) each signifying different power dissipating mechanism for electrons and ions. The total discharge power P_{dis} is dissipated inside the plasma and sheath to balance the many plasma loss mechanisms. Predominant fraction of power is coupled to the electrons in the bulk plasma which subsequently dissipates it through various collisional/non-collisional dissipative processes. The collisional ohmic heating (R_p) of electrons via elastic/inelastic collisions with the background neutrals is the dominant means of power dissipation at intermediate/high pressures; however at low pressures (ionization mean free path,$\lambda_i > d$, electrode gap length) the columbic collisions of the electrons with the oscillating sheath electric field becomes the dominant power dissipating/coupling mechanism to sustain the plasma bulk. This mechanism of heating is also known as the stochastic/non-collisional (R_{stoc}) heating of electrons. In the present experiment; we are operating in low pressure regime and hence it is estimated that R_{stoc}

dominates over the ohmic resistances (R_p and $R_{ohm,sh}$). The power dissipated in the positive ion acceleration in the sheaths is accounted for in the equivalent circuit by resistance R_i.

Although the Power is mostly transferred to the plasma electrons; however to maintain a steady state plasma, a fraction of the total power is also transferred to positive ions; which are accelerated in the DC sheath voltages to the electrodes[11]. This fraction of power transferred to the ions is typically small at lower RF powers (plasma density); while it tends to increase as the RF power (Plasma density) is increased. Therefore, with the increase in plasma density a shift from power dissipation from electron dominated to the ion dominated inside the sheath is seen. This has been widely referred as power mode transition in CCP discharges.

This could be essentially understood as follows: As RF power is gradually increased, the plasma density also increases ($n_0 \propto I_{dis}$). The increase in plasma density has different effects on the fractional power distribution to electrons in bulk/sheaths and ions in the sheaths. The increase in plasma density makes the plasma more conducting as both $R_{stoc} \propto \frac{1}{I_{dis}}$ and $R_p \propto (\frac{1}{I_{dis}})^{3/2}$ [16] [Table 5.1 of Ref[16]] are inversely proportional to the discharge current. On the other-hand with increase in plasma density the ion flux in the sheaths would increase and therefore $R_i \propto {I_{dis}}^{1/2}$.

As the dominant resistance $R_{stoc} \propto \frac{1}{I_{dis}}$; the fraction of power transferred to electrons P_{elec} becomes a linear relation of the discharge current ($P_{elec} \propto I_{dis}$). Meanwhile as $R_i \propto {I_{dis}}^{1/2}$; the power transferred to ions in the sheaths $P_{ion} \propto {I_{dis}}^{5/2}$. Therefore at low P_{dis} or I_{dis} the fraction of power coupled to ions is very small as the ion bombarding flux/energy is low in the sheaths. Now as the plasma density/sheath voltage drop increases with RF power (P_{dis}); the ion flux and the ion energy of the bombarding ion also increases leading to increased fraction of the power coupled to ions in sheaths as compared to electrons. Hence, once the ion dissipating mode starts to dominate between the two competing modes; a mode transition in power coupling has occurred. The power mode transition has been the subject of research for number of reasons:

1. It is the primary reason for observing saturating plasma densities in CCRF plasma discharge as subsequent to reaching the point of transition in a CCRF plasma; any increase in RF power will be primarily utilized in ion acceleration inside the sheaths.

2. Almost all of the substrate processing in CCRF plasma reactors are dependent on the RF power coupling to ions for ion bombardment onto the substrate to achieve desired material properties. This necessitates the study of RF power coupling into ions inside the sheaths and its external control.

Beneking [71] in 1990 was the first to suggest such a transition in dissipation modes in CCRF plasmas. In that work, he quantified the power sharing between the two dissipative modes with help of an equivalent circuit model and the impedance measurement of the plasma discharge. He also obtained and validated a relation for the power dissipation in sheaths for discharge current and RF frequency $P_{ion} \propto (\frac{I_{dis}}{\omega})^{5/2}$. Power mode transitions were further investigated by Godyak et.al [60] and You et.al [2] with help of impedance measurements. In those works, Godyak et.al showed that the transition from electron to ion dominated dissipation shifts to higher discharge currents as pressure is increased; while You et.al revealed the effect of magnetic field on the power mode transition. It was showed in that work that magnetic field has a similar effect as increasing pressure since the power mode transition shifts to higher discharge current (RF power) by increasing the transverse magnetic field to the CCRF plasma i.e. increasing transverse magnetic field allows more power coupling into electrons. A recent PIC simulation work by S.Sharma et.al [7] on CCRF discharge demonstrated the effectiveness of static transverse magnetic field in controlling the ion energy and flux to the electrodes. They obtained a 60% reduction in sheath widths (that improves control of ion energy) and a fourfold increase in the ion flux at the electrode as a consequence of the altered ion and electron dynamics due to the ambient magnetic field.

If we could possibly control the ratio of the RF power sharing amongst the electrons and ions then one may possibly control not only the plasma density but also the ion energy/flux for plasma processing. So far the studies on power mode transitions has been mainly conducted for the un-magnetized case, however recently few works [7] [6] have discussed the role of external magnetic field in the power coupling and power mode transitions in a CCRF discharge. In the present context, we observe the effect of transverse magnetic field on the power mode transition through impedance measurements. The eventual goal of this work is optimizing the magnetic field for designing a plasma source wherein magnetic field controls the power sharing between the electrons and ions as per requirement of the processing substrate.

4.2 Identifying power mode transition through impedance measurements

The power mode transition could be conveniently identified from the plasma impedance measurements as the plasma resistances which co-relates to the electron and ion heating in the CCRF plasma have unique dependence on the RF power (Discharge current I_{dis}). The underlying reason for this behavior of a CCRF discharge is due to the intrinsic nature of plasma resistances with increasing RF power (Discharge current).The RF power coupled to the electrons is dissipated by the plasma electrons (P_{elec}) ; while the power coupled to the ions are dissipated by ions inside the sheaths (P_{ion}). These two independent mode of power dissipation combines to present them as a dissipative resistor R in the equivalent circuit of CCRF discharge presented in chapter-1. The resistance $R = R_{stoc} + R_{ohm,sh} + R_p + R_i$ in the equivalent circuit of the plasma is comprised of various heating mechanism for the plasma electrons and ions. Here, $R_{stoc}, R_{ohm,sh}$ and R_p represents the electron dissipative resistors; while R_i represents the ion dissipative resistor. All the four dissipative resistors are plasma dependent and therefore changes with discharge current (RF power).

As a result, the dominant heating mechanism (dissipative modes) between electrons and ions is dependent on the discharge current (I_{dis}). The total discharge power is $P_{dis} = (I_{dis})^2.R = P_{elec} + P_{ion}$.Therefore, the profile of $P_{dis}(I_{dis})$ is dependent on effect of I_{dis} on the individual resistive components $R_{stoc}, R_{ohm,sh}, R_p$ and R_i. The dependency of these resistors ($R_{stoc}, R_{ohm,sh}, R_p$ and R_i) on I_{dis} have been found for parallel plate discharges i.e.$R_{stoc}, R_{ohm,sh} \propto \frac{1}{I_{dis}}$ and $R_p \propto (\frac{1}{I_{dis}})^{3/2}$; while $R_i \propto (I_{dis})^{1/2}$ [16]. For low pressure discharges the R_{stoc} dictates the electron dissipative resistors i.e. $P_{elec} \approx (I_{dis})^2 R_{stoc}$ and therefore, the dependence of $P_{elec}(I_{dis})$ is linear; while $P_{ion}(I_{dis})$ shows a non-linear dependence $P_{ion} \propto I_{dis}^{5/2}$. The combined effect of $P_{elec}(I_{dis})$ and $P_{ion}(I_{dis})$ on $P_{dis}(I_{dis})$ is thus as follows; At low RF powers (discharge currents I_{dis}) the P_{ion} is smaller; as P_{elec} dominates. This behavior is reflected in the linear nature of plot between $P_{dis} Vs.I_{dis}$. However, when the RF power is high (large I_{dis}); the characteristic of $P_{dis} Vs.I_{dis}$ changes from linear to non-linear dependence signifying a change in dominant heating mechanism. This change in the behavior of plot of $P_{dis} Vs.I_{dis}$ indicates power mode transition from electron dominated dissipation to the ion dominated dissipation.

The above mentioned technique for observing the power-mode transition was used by You et.al [2]. Although the dependency of $P_{ion} \propto I_{dis}^{5/2}$; You.et.al proclaimed a change from linear to square dependency in characteristics of $P_{dis} Vs.I_{dis}$ would indicate a transition. Equally, one can also identify the power mode transition from a plot of real voltage drop plotted against the discharge current i.e. $V_{dis} cos\phi$ Vs. I_{dis}. The latter method was preferred by Godyak et.al [60] to identify the power mode transitions in CCP's. We have used both the methods for observing the transitions in the parallel plate and the cylindrical CCP setups.

The P_{dis} Vs. I_{dis} is based on Eq: 4.1; which represents the total RF power coupled to the plasma [2] [71];

$$P_{dis} = V_p I_{dis} + R_i (I_{dis})^2 \tag{4.1}$$

In the above equation, V_p is the real component of the voltage drop across the discharge which includes both the collisional and the stochastic electron heating. Therefore, the first term on the right hand side of represents the electron heating across the discharge (P_{elec}); while second term corresponds to the ion heating in the sheaths (P_{ion}). Now, it is known that the V_p is almost independent of I_{dis} as $V_p \propto I_{dis}^{-0.15}$ [71] and the driving frequency (ω) owing to ionization and energy balance in an weakly ionized plasma [71] [60]. Since in low pressure CCRF plasmas $V_p \approx I_{dis} R_{stoc}$ and $R_{stoc} \propto \frac{1}{I_{dis}}$, therefore V_p remains almost constant with increase in I_{dis}. As for the second term; $R_i \propto (I_{dis})^{1/2}$; hence, $P_{ion} \propto I_{dis}^{5/2}$ [71].

Godyak et.al [60] on the other-hand chose to observe the power mode transition from the plot of real voltage drop V_{real} Vs. I_{dis}. The real voltage drop (V_{real}) across the discharge is given by;

$$V_{real} = V_{dis} cos\phi = I_{dis} R = V_p + V_i \tag{4.2}$$

Here, $V_p = I_{dis} R_{elec}$ and $V_i = I_{dis} R_i$ are the real voltage drops across the discharge corresponding to electrons and ions. We have already seen that V_p is almost independent of I_{dis}; while $V_i = I_{dis} R_i$. Now, as $R_i \propto I_{dis}^{1/2}$; the potential drop V_i increases with I_{dis}. Therefore, at low I_{dis}, V_p dominates as most of the power is coupled into the electrons , however when I_{dis} is increased with increase in RF power; V_i begins to dominate indicating higher power coupling to the ions in the sheaths. Consequently a plot of $V_{real}(I_{dis})$ is almost flat at low I_{dis} and starts to increase as I_{dis} is increased. Accordingly, a sudden change in slope of the plot of $V_{real}(I_{dis})$ also represents a power-mode transition in CCRF plasma.

4.3 Experimental Results

4.3.1 Power-mode transition in un-magnetized systems

Power mode transition in parallel plate setup is observed in an argon discharge at 1.0 Pa neutral gas pressure [70]. The transition in this case is identified from the plot of real voltage drop Vs. discharge current as seen in Fig 4.1

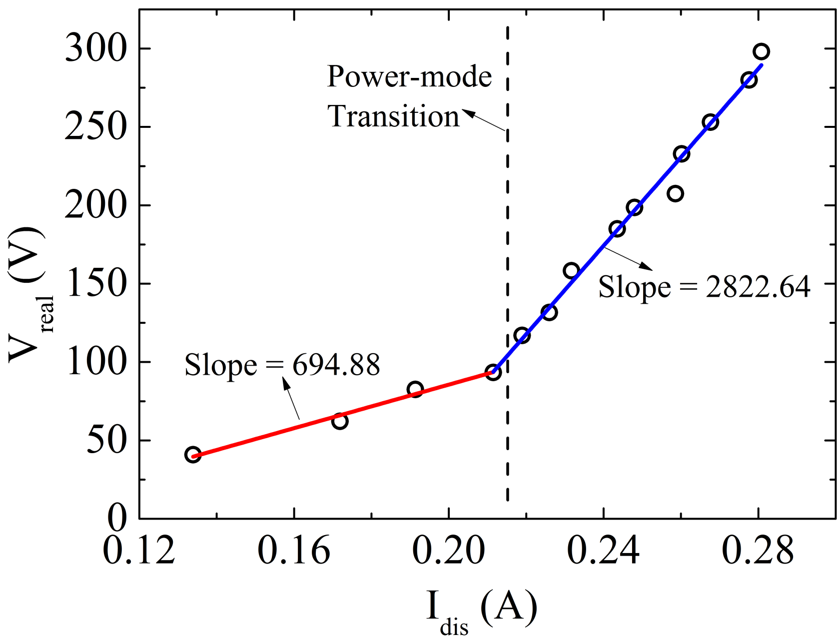

Figure 4.1: Plot of V_{real} Vs. I_{dis} at 1.0 Pa argon discharge in parallel plate setup

Looking in detail at Fig 4.1, the real voltage drop increases slowly up to 0.21 A while it sharply begins to increase as I_{dis} rises above 0.22 A. This sudden change in the slope m=694.88 to m = 2822.64 signifies the power-mode transition. The approximate point of transition is marked by the dotted vertical line in the plot. The plot in Fig 4.1 is a typical plot of V_{real} Vs. I_{dis} for a un-magnetized CCRF plasma.

4.3.2 Power-mode transition in magnetized systems

1) Parallel Plate System

As seen in the previous section, a power-mode transition is conveniently achieved for an un-magnetized parallel plate CCRF discharge. The situation however is different in presence of 7.0 mT transverse magnetic fields. A plot of V_{real} Vs. I_{dis} in the magnetized case of is plotted in Fig 4.2.

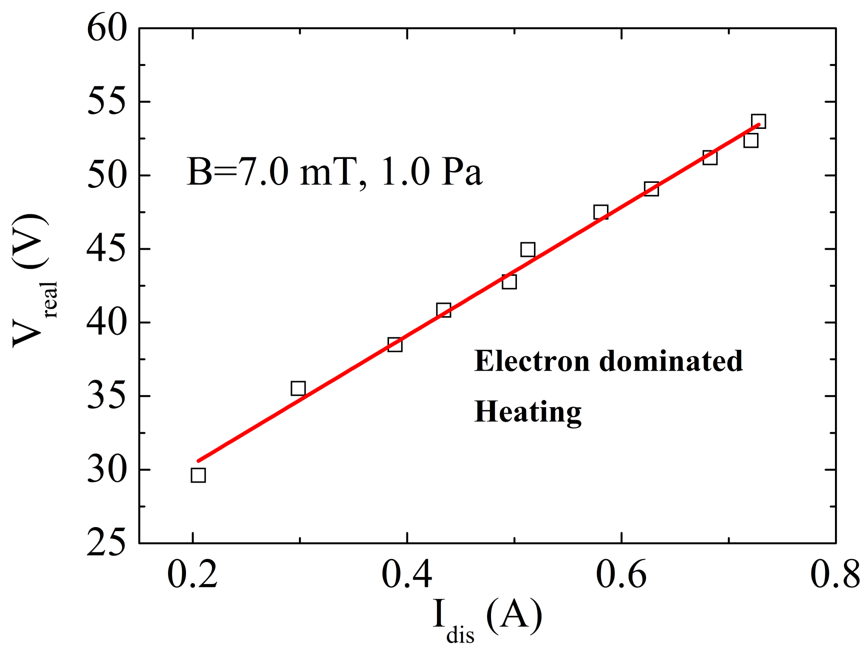

Figure 4.2: Plot of V_{real} Vs. I_{dis} at 1.0 Pa and 7.0 mT argon discharge

From, this plot it is seen that the real voltage drop does not exhibit a change in the slope with increase in I_{dis} with very small change in the real voltage drop values. Therefore, it is concluded that power-mode transition is not observed in presence of 7.0 mT transverse magnetic field and the discharge remains in the electron dominated heating regime only.

2) Cylindrical CCRF System

To observe the power mode transitions in a cylindrical CCP setup; we plot $P_{dis} Vs. I_{dis}$ as seen in Fig 4.3 and 4.4 for argon and helium discharge in presence of 2.8 mT axial magnetic fields at 1.0 Pa neutral gas pressures [72].As the dependence of the plot is expected to be as per Eq 4.2 ; where a linear to non-linear change in the plot would point to the power-mode transition. Ensuing You.et.al [2] method to identify the transition to non-linearity; we try to recognize a change from linear to squared dependency in the plot of $P_{dis} Vs. I_{dis}$ and therefore we take a parabolic fit $(Ax^2 + Bx + C)$ to the data points. We also plot on the same graph the straight line derivative plot $(\frac{dP_{dis}}{dI_{dis}})$ of the parabolic fits. The slope "m" of the derivative plots directly relates to the co-efficient A of the parabolic fit i.e. m=2A.

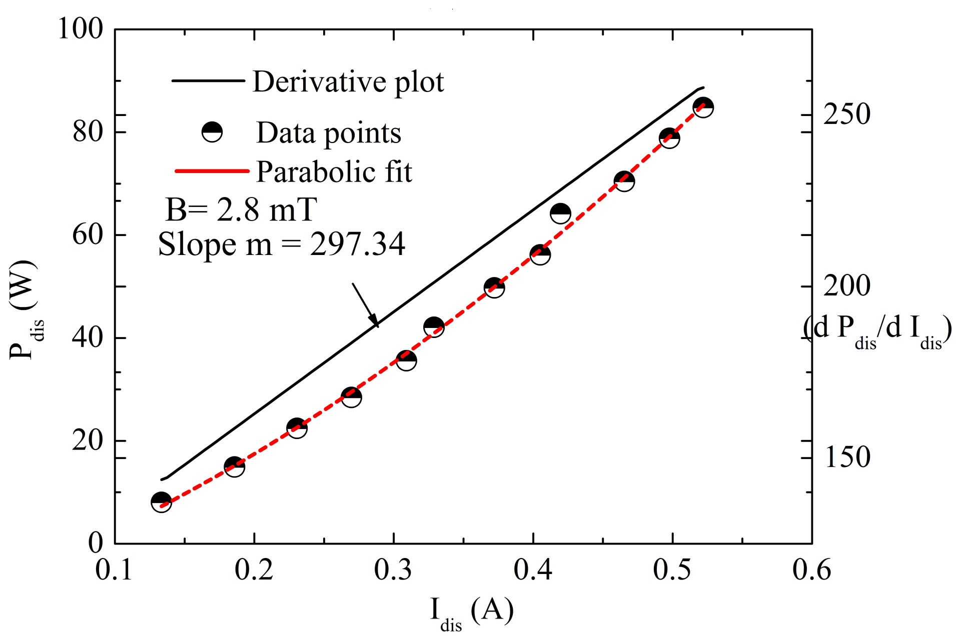

Figure 4.3: Plot of P_{dis} Vs. I_{dis} and $(\frac{dP_{dis}}{dI_{dis}})$ for 2.8 mT in argon discharge.

The value of slope "m" therefore is an indirect means to ascertain the square dependence of the P_{dis} plot. Hence, higher the value of "m" higher is the power coupling to ions inside the CCRF discharge i.e. second term in Eq 4.2 is dominating. The effect of magnetization on the power mode transitions can thus, be qualitatively obtained from the slopes "m" of the $(\frac{dP_{dis}}{dI_{dis}})$. These results are discussed in the following section.

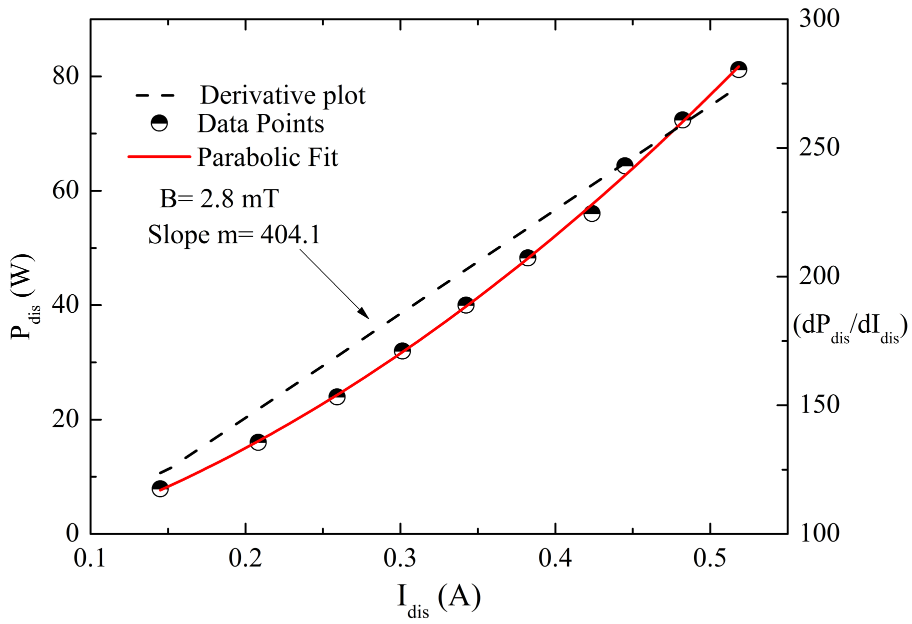

Figure 4.4: Plot of P_{dis} Vs. I_{dis} and $(\frac{dP_{dis}}{dI_{dis}})$ for 2.8 mT in helium discharge.

4.4 Discussion

As seen in Fig 4.1 the transition in the power coupling from plasma electrons to the ions inside the sheaths is obtained conveniently for a un-magnetized CCP discharge;. However, similar a transition is not observed in the transversely magnetized CCP discharge [p.s. Fig 4.2].

This effect of transverse magnetization on power-mode transition is consistent with similar observation by You et.al in their seminal work on effects of magnetic field on power-mode transitions [6]; where they proved that gradually increasing the transverse magnetic field shifted the mode transitions to higher discharge currents (RF powers).

The reason for discharge remaining in the electron dominated heating in presence of transverse magnetic field of 7.0 mT could be qualitatively understood as follows: A transverse magnetic field is known to enhance the collisions in the bulk plasma [5]. This leads to increased value of R_p [11]; while the stochastic heating of the electrons by sheath oscillations is also enhanced due to transverse magnetic field [11]. Therefore both R_p and R_{stoc} corresponding to the electron heating in the plasma is increased in presence of magnetic field which pushes the transition point at higher at higher discharge current (P_{dis}).

Moreover, the confinement of electrons in the bulk by magnetic field; also reduces the particle losses from the system. This would lead to a reduced amount of non ambi-polar ion loss from the system ultimately leading to less power coupling to ions in the sheaths. From, an electrical stand point the magnetic field is recognized to reduce the sheath width [7] at electrodes reducing the capacitive potential drop across the sheaths and therefore prompting less acceleration of ions in the sheaths. Consequently, the value of R_i is diminished in presence of magnetic field. Overall the magnetic field enhances R_p and R_{stoc}; while reduces R_i leading to significantly reduced power coupling into ions as electron dominated heating with no power mode transition is observed at 7.0 mT of transverse B-field.

As mentioned in the previous section; we highlight the effect of axial magnetic field on power mode transition in cylindrical CCRF plasma by observing the slope "m" of the derivative plot ($\frac{dP_{dis}}{dI_{dis}}$). The slopes of the derivative plots with increasing axial magnetic fields are shown in Table 4.1.

	Mag. Field (mT)	Slope m (Argon)	Slope m (Helium)
1	2.8	297.34	404.1
2	14	189.54	379.56
3	25.2	102.82	239.74
4	28.0	94.88	242.16

Table 4.1: Slope of ($\frac{dP_{dis}}{dI_{dis}}$) for varying magnetic field

The decreasing values of slope "m" with increasing magnetic field for both argon and helium again suggests increased fraction of power to electrons than ions with increase in axial magnetic field. This behavior remains consistent with the results of parallel plate setup. However, the trend of helium is noteworthy as in Table 4.1, the numerical value of the slope falls at a relatively faster rate in argon than in helium. For argon, the heavy positive ions are accelerated only inside the DC electric fields of sheath. On the other hand, the lighter helium ions instantly respond to time-varying RF electric field ($\omega_{rf} \approx \omega_{pi}$) inside the sheath as well as inside the bulk. As a result for helium the power coupling to helium ions inside the bulk cannot be neglected. This results in a relatively slower rate of decrease in power coupling to ions as the magnetic field increases. The behavior of low frequency sheaths in our experimental frequency regime ($\omega_{rf} \approx \omega_{pi}$) is still an open problem with significant implications in RF heating by antennas in tokomaks [11].

4.5 Summary and Conclusions

In summary, this chapter discussed the effect of transverse magnetic field on the power mode transition in parallel plate and cylindrical CCRF plasmas. The previously known effects of magnetic field on power mode transitions are reaffirmed by the experimental results on both the experimental setups. The underlying reason for the effects of magnetic field on power mode transitions is explained through enhanced collisional and stochastic heating of electrons along with diminishing ion heating in the sheaths in presence of transverse magnetic field. It is also found that the nature of the power coupling varies with ions of different masses. For 10 times lighter helium ions than argon, the power coupling into the ions is also expected to be inside the bulk plasma which is attributed to the ion response to the RF oscillations.

In conclusion, we report that magnetization of CCRF plasmas can alter the power sharing between the two dissipation modes of electron (P_{elec}) and ions (P_{ion}). Although a static magnetic field cannot couple any power to the plasma; however it is seen that with increase in magnetic field, the discharge remains in electron heating mode for higher discharge powers. Therefore, the plasma density is enhanced by higher power dissipation by electrons in the bulk in presence of B-Field; which is a limitation of a non-magnetized CCRF discharge. The lighter ions response to the RF fields in CCRF discharge also alters the power coupling dynamics between ions and electrons and therefore; it is of vital importance to consider this effect especially in higher frequency CCRF plasmas such as 60 MHz. Such effects of magnetic field on power coupling through sheaths for responsive ions may also be important in ICRF heating schemes in tokomaks where a resonance region could be shifted due to effects of sheaths near the antenna where the magnetic field is generally at an oblique/ parallel to the surfaces. Further research on this topic is still required to assess the possibility of magnetic field controlled ion bombardment for processing substrates and for designing a magnetized plasma system for plasma processing applications.

Chapter 5

Electron Series Resonance Phenomena

5.1 Introduction

Earlier in chapter-1, the electrical equivalent circuit of CCRF discharge was briefly discussed. The sheath acts as a capacitor C_{sh} in series with the bulk plasma composed of plasma resistance R and inductance L_p [c.f. Fig 1.5]. Their combination can be treated as analogous to an R-L-C series circuit. Unlike an ordinary electric circuit, the parameters R and L_p and C_{sh} are plasma dependent and rely on the intrinsic properties of plasma. A condition of series resonance can occur in a CCRF discharge when the reactive impedance offered by the bulk plasma, i.e $X_p = j\omega L_p$ exactly cancels the reactive impedance offered by the sheaths $X_{sh} = -j/\omega C_{sh}$. This is popularly recognized as series resonance in CCRF discharge. Under this condition the discharge behaves as a pure resistive plasma load, implying $Z = R + jX = R$ as $X_p = X_{sh}$.

Experimentally the series resonance effect in a CCRF plasma can be identified by careful measurement of the plasma reactance while, theoretically one can identify the condition by solving for the RF frequency at which the $X_p = X_{sh}$ i.e. for resonance $\omega_{res} = 1/\sqrt{L_p C_{sh}}$. For a symmetric parallel plate setup; this simplifies to $\omega_{res} = \omega_{pe}\sqrt{s/d}$ where s – sheath width and d – plasma length. A detailed derivation of this equation is presented in section 5.2. Historically, while Schneider and Angew were the first to suggest the existence of resonance in a CCP discharge with the full description being given by Taillet [17]. In Taillet's work they presented homogeneous collisional model of plasma to verify the results with the experiments. Extensive experimental studies were performed by Godyak [73] since the $1970's$; The primary predictions from these works suggested (i) two possible values of plasma density can be obtained for a given RF voltage across the discharge plates, (ii) the driving amplitude of RF voltage is minimal during ESR condition. Godyak and Popov experimentally validated the existence of ESR in a symmetric parallel plate argon discharge.

Cooperberg and Birdsall [74] have extensively performed PIC-MCC (Particle in Cell with Monte-carlo-collisions) simulations on ESR discharges. EEPF measurements from this simulation study revealed hot electron tail at low pressure discharges. They also verified the scaling laws for sheath widths and electron densities with the Godyak experiments. A comprehensive study on ESR can be found in the thesis by W.D. Qiu [75]. Their studies included the role of an external magnetic field on ESR condition. They had also simulated the initiation and "locks on" (lock on - Resonance achieved in frequency chirping) for resonance discharges. A global plasma model along with the equivalent circuit of discharge are used to find the interrelations among the sheath widths, plasma densities and the electron temperatures with the power supply parameters such as frequency, voltage and current as the input parameters to the model.

ESR's are not only unique to a particular plane parallel plate system but it can be observed for all geometries. ESR condition in a co-axial and concentric spherical RF diode geometries have been simulated [75]. The resonance condition was also observed for non-uniform plasmas where the dense plasma behavior was inductive and the rarefied plasma behaves as a capacitor.

From, all the above mentioned experimental/simulation and theoretical works it is established that the main advantages of operating in ESR are:

1. The driving voltage under ESR is small, i.e of the order of $\sim T_e$; while the ion bombardment energy is typically $\sim (10T_e)$, which corresponds to the time-averaged spatial plasma potentials between the discharge plates.

2. For compensating the capacitive reactance in the sheaths, a significant inductive potential drop occurs across the bulk plasma. Hence the potential across the plasma bulk can be significantly higher than the net RF potential across the electrodes. Consequently, highly energetic directional electrons are present inside the bulk plasma during ESR.

3. The electrons responding to the oscillatory RF potentials/ electric field inside the bulk plasma, gives rise to space charge bunching of electrons, during alternate half cycle near the electrode. The back and forth motion of electrons at RF time scales enhances the ionization probability in the plasma bulk and enables operating at lower pressures.

4. Unlike the non-resonant CCRF discharges, the ion energy distribution shifts from a double energy peak to a single peak during ESR. The bombarding ions has a narrow angular spread and a single peak in ion energy is observed that corresponds to the plasma potential [75]. The beam-like ion energy brings better process uniformity and control on to the processing substrate.

5. Since the plasma load is purely resistive during ESR, therefore the RF matching become trivial and allows maximum RF power transfer to the plasma.

Due to the above reasons operating the CCRF discharge in ESR condition becomes highly significant. However, it is practically difficult to achieve this condition with a fixed RF frequency source. For processing relevant plasma densities of the order of $10^{16}m^{-3}$; the resonance condition is much higher than conventional RF frequencies such as 13.56 MHz. The series resonance reported by Godyak and Popov [73] in a symmetric parallel plate system for typical plasma densities in range of $10^{16}m^{-3}$ was obtained at a driving frequency of 81.36 MHz.

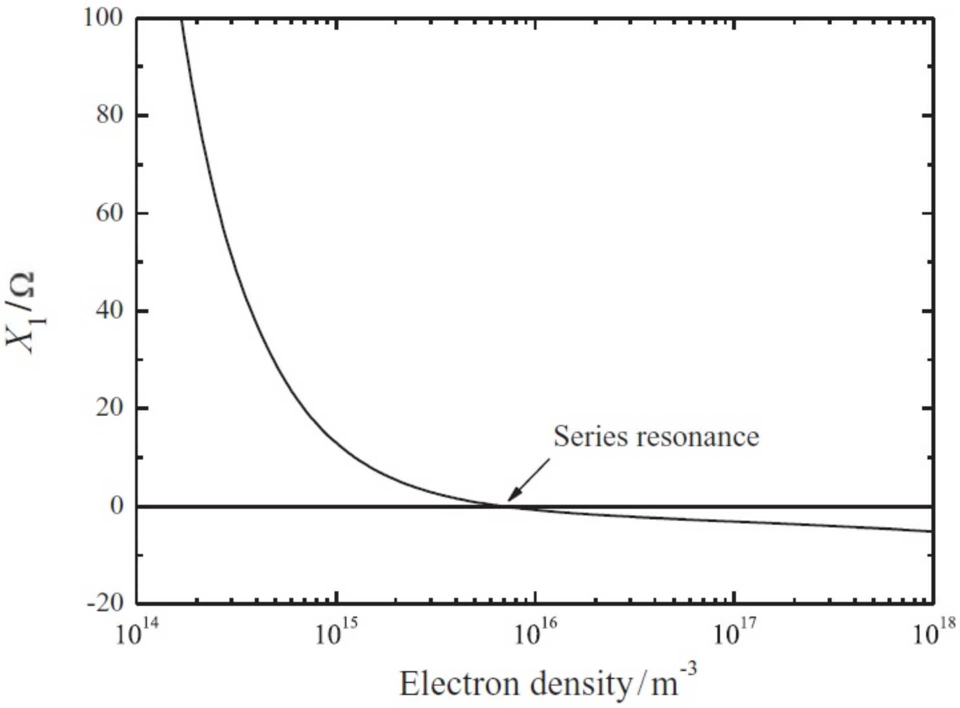

Figure 5.1: Typical Reactance Vs. Density plot for a 135.6 MHz parallel plate discharge. *Image courtesy: Physics of RF plasma by Chabert and Braithwaite [16], Cambridge university press, UK . Reproduced with permission of The Licensor through PLSclear*

Figure 5.1 plots the plasma reactance as a function of plasma density for 135.6 MHz argon discharge. At low plasma densities (RF powers), the plasma load generally behaves inductively, whereas it shifts to capacitive as the plasma density increases with RF power. In-spite of several advantages, the demand of typically 6 to 10 times higher frequency than conventional 13.56 MHz limits the application of ESR in normal processing applications. Qiu in his thesis looked at the possibility of introducing an external magnetic field as a parameter to induce the ESR. However their study was limited to 1-D simulation and far from relevant experimental conditions. In this chapter we experimentally demonstrated the ESR due to presence of a transverse magnetic field and validated the results based on an analytical model. The study can be beneficial for the design of plasma sources with salient features observed during electron series resonance observed in CCRF discharges.

5.2 Analytical Formulation of Electron series resonance

The ESR is achieved when the complex part of the discharge impedance vanishes. From here on in this thesis, discharge impedance corresponds to total impedance of plasma bulk + sheath; while plasma correspond to bulk plasma impedance and sheath correspond to sheath impedance.

From the cold plasma conductivity as given in [10];

$$\sigma = \frac{ne^2}{m(\nu_m + j\omega)} = \frac{\epsilon_0 \omega_{pe}^2}{\nu_m + j\omega} \tag{5.1}$$

Due to the presence of highly conducting free electrons in plasma bulk; it is reasonable assumption to ignore the displacement current in comparison to the conduction current through the plasma bulk.

$$Z_B = \frac{d}{A\sigma} = \frac{d}{A\epsilon_0 \omega_{pe}^2}(\nu_m + j\omega) \tag{5.2}$$

Where, A – plasma cross-section and d – plasma length.

Inside the sheath, the conduction current through the sheath can be neglected. The capacitive reactance for a planar electrode sheath is given as

$$Z_s = \frac{s}{jA\omega\epsilon_0} \tag{5.3}$$

Where, s is the total sheath width at both electrodes.

The total impedance of the discharge Z is sum of Z_B and Z_s;

$$Z = Z_B + Z_s = \frac{d}{A\epsilon_0 \omega_{pe}^2}(\nu_m + j\omega) + \frac{s}{jA\omega\epsilon_0} \tag{5.4}$$

On equating the complex part of the above equation to zero, gives the series resonance

ω_{res}. i.e.

$$j\frac{\omega_{res}d}{A\epsilon_0\omega_{pe}^2} = j\frac{s}{A\omega_{res}\epsilon_0} \tag{5.5}$$

Simplifying this we get;

$$\omega_{res} = \omega_{pe}\sqrt{s/d} \tag{5.6}$$

For characteristic plasma density of CCRF plasmas in the range of $10^{16-17}m^{-3}$, ω_{pe} ranges from $1-5\times 10^9 rad/sec$. If one assume a combined sheath width of $s \sim 10mm$, and bulk plasma of 70.0 mm, in the parallel plate setup used in this thesis; the factor $\sqrt{s/d} = 0.37$. Consequently, for such typical values of plasma density and sheath width the resonance condition should exist at few $100's$ of MHz. Therefore, a series resonance is not observed for a 13.56 MHz ($\omega_{rf} = 85.2\times 10^7 rad/sec$) discharge in the typical density of CCRF discharges; while Godyak and Popov [73] obtained it at 6 times higher frequency. Although symmetric parallel plate discharge do not exhibit resonance condition at lower frequencies; however, some experimental/ simulation studies have reported series resonance in low frequency asymmetric discharges [16]. The reasons have been attributed to non-linear harmonics generated in asymmetric RF sheaths [57].

5.2.1 Analytical formulation for Electron series resonance in a transversely magnetized CCRF plasma

In this experiment, the resonance is observed in presence of transverse magnetic field. To highlight the role B-field plays in inducing this resonance; we again resort to cold plasma conductivity in presence of magnetic field. For the experimental setup discussed in chapter-2 Fig 2.1; we consider the B-field along the Z-axis. The driving electric field perpendicular to the electrodes is considered along X-axis. This results in current density $J = \overline{\overline{\sigma}}E$, where $\overline{\overline{\sigma}}$ is anisotropic conductivity tensor and $\vec{E}$ is the total electric field vector.

Therefore $\vec{J}$ can be described according to Bittencourt [10] as follows:

$$\begin{pmatrix} J_x \\ J_y \\ J_z \end{pmatrix} = \begin{pmatrix} \sigma_\perp & -\sigma_H & 0 \\ \sigma_H & \sigma_\perp & 0 \\ 0 & 0 & \sigma_\parallel \end{pmatrix} \begin{pmatrix} E_x \\ E_y \\ E_z \end{pmatrix} \tag{5.7}$$

Considering Y-axis along the length of the parallel plate electrode; then the perpendicular (to B-field) component of currents is given by,

$$J_x = \sigma_\perp E_x - \sigma_H E_y \tag{5.8}$$

$$J_y = \sigma_H E_x + \sigma_\perp E_y \tag{5.9}$$

Where, $\sigma_\perp$ and σ_H are respectively the transverse and hall conductivities in magnetized plasma.

J_y is the hall current component in the parallel plate setup. This component is directed along the length of the plates. However, as this is a bounded system in Y-axis with two flush mounted floating plates as the boundary [p.c. Fig 2.1 chapter-2]; the plasma electrons cannot flow un-impeded. Therefore an intrinsic electric field would setup inside the plasma to restrict J_y. For comparison in azimuthally symmetric systems; such as hall thrusters [76] , the hall current is closed within the plasma, and therefore in steady state the hall electric field is zero. However, in the Cartesian system, a time averaged $\vec{E} \times \vec{B}$ drift propagates along Y-axis. This drift is due to ambi-polar electric field along (+/-) X-axis, with B-field along Z-axis; as shown in Fig 2.1 and 2.2. These drifted electrons constitute a net current along Y-axis; which likely closes through the floating conducting end plates. The short-circuiting effects of conducting boundaries in magnetized discharge is well-known phenomenon since 1955 [77] and recently also by chen and currelli [78]. Only difference in this case is that current is due to the $\vec{E} \times \vec{B}$ drifts.

Simulation results for similar setup, as used in this experiment also report; that $\vec{E}\times\vec{B}$ drifts are dominant in the sheaths and pre-sheath regions. These drifts are opposite for the top and bottom electrodes and commensurate at the electrodes for an electrically symmetric discharge [22]; which is also the case in the current setup. Therefore, it is supposed that the $\vec{E} \times \vec{B}$ drift closes in a rather complex manner and a detailed description of which would be an involved study which has to be done separately. Considering a closed $\vec{E} \times \vec{B}$ drift one can assume the electric field $E_y << E_x$, except near the floating end plates at the extreme ends of Y-axis. Therefore from Eq: 5.8 , the net RF current through the discharge plates along X-axis approximates to;

$$J_{rf} = J_x \approx \sigma_\perp E_x \tag{5.10}$$

Considering the transverse plasma conductivity $\sigma_\perp$ as given in Bittencourt [10],

$$\sigma_\perp = \frac{ne^2}{m}\left[\frac{\nu_m \pm j\omega}{(\nu_m \pm j\omega)^2 + \Omega^2}\right] \tag{5.11}$$

Where, Ω is the electron cyclotron frequency

The $\pm$ sign in the conductivity gives two practical solutions for the resonance conditions. First, considering –ve sign in the conductivity equation and performing a similar analysis as done for the un-magnetized cold plasma conductivity in bulk plasma yields the bulk plasma impedance as;

$$Z_B = \frac{d}{A\sigma_\perp} = \nu_m L_p\left[1 + \frac{\Omega^2}{\nu_m^2 + \omega^2}\right] - j\omega L_p\left[1 - \frac{\Omega^2}{\nu_m^2 + \omega^2}\right] \tag{5.12}$$

In Eq: 5.12 L_p is the bulk plasma inductance; which can be expressed [16] as $L_p = 1/(\omega_{pe}^2 C_b)$ where $C_b = \frac{\epsilon_0 A}{d}$ is the capacitance of the bulk plasma and $\omega_{pe}^2 = \frac{ne^2}{m\epsilon_0}$ is the electron plasma frequency.

Consequently, the total discharge impedance together with the sheath becomes;

$$Z = Z_B + Z_s = \frac{d}{A\sigma_\perp} + \frac{s}{jA\omega\epsilon_0} = \nu_m L_p\left[1 + \frac{\Omega^2}{\nu_m^2 + \omega^2}\right] - j\omega L_p\left[1 - \frac{\Omega^2}{\nu_m^2 + \omega^2}\right] - j\frac{s}{A\omega\epsilon_0} \tag{5.13}$$

Separating the reactive component (imaginary term) of Z = R + jX,

$$X = -j\omega L_p[1 - \frac{\Omega^2}{\nu_m^2 + \omega^2}] - j\frac{s}{A\omega\epsilon_0} \tag{5.14}$$

Equating this Eq: 5.14 to zero; would yield the condition of series resonance in magnetized plasma that is;

$$\omega_{res,B} = \omega_{pe}\sqrt{s/d}[\frac{\nu_m^2 + \omega^2}{\Omega^2 - (\nu_m^2 + \omega^2)}]^{1/2} = \omega_{res}[\frac{\nu_m^2 + \omega^2}{\Omega^2 - (\nu_m^2 + \omega^2)}]^{1/2} \tag{5.15}$$

Here, $\omega_{res,B}$ is the modified resonance frequency in magnetized CCRF discharge and $\omega_{pe}\sqrt{s/d}$ is the series resonance frequency in the un-magnetized case. In Eq 5.15; it is to be noted that $\omega_{res,B}$ and ω is the same i.e. driving frequency. Therefore Eq 5.15 shows that the driving frequency at which the discharge would exhibit ESR is dependent on the Pressure (ν_m) magnetic field (Ω) and driving frequency (ω) as discharge impedance changes with all these parameters. This has been discussed further in Section 5.4.

Considering a collision-less ($\nu_m = 0$) case; the condition of resonance in Eq: 5.15 becomes

$$\omega_{res,B}^2 = \Omega^2 - \omega_{res}^2 \tag{5.16}$$

If, we would have considered +ve sign in Eq: 5.11 then following the same derivation Eq: 5.16 would change to give

$$\omega_{res,B}^2 = \Omega^2 + \omega_{res}^2 \tag{5.17}$$

The solution of Eq.5.17 is similar to an upper hybrid resonance frequency in plasma wherein ω_{pe} is replaced by ω_{res} due to the effect of sheaths on the resonance. We know, that $\Omega = 1.23 \times 10^9 rad/sec$ (7.0 mT); while ω_{res} is also in similar range. Therefore, $\omega_{res,B}^2$ would also be in $10^9 rad/sec$ range as per Eq: 5.17. However, the experimental observation of resonance is at $8.52 \times 10^7 rad/sec$ and therefore, the observed resonance could only be explained by the solution of Eq 5.15.

For Collision-less case in Eq 5.16 and Eq. 5.17 as $\nu_m = 0$; the resistance of the plasma bulk becomes zero. Therefore, plasma cannot sustain. Consequently, the resonance given by Eq. 5.16 and 5.17 is basically the resonance of a L-C Series circuit; which is not a real solution for plasma. These limiting cases of $\nu_m = 0$ were shown just to highlight the fact the we must consider only the -ve sign in conductivity Eq 5.11 to derive the condition of resonance in 5.15. For +ve sign in Eq 5.11; the resonance condition would be satisfied in much higher frequency range. Two solutions of frequency were also found by Qiu [75] for the same magnetized plasma conditions.

5.3 Experimental Results

We report the first experimental observation of ESR condition in transversely magnetized plasma in 13.56 MHz argon discharge [70]. This experiment is performed in the parallel plate experimental system details of which are already disclosed in chapter-2.

As shown in the Fig:5.2, the discharge reactance shows a similar form as shown in Fig:5.1 as it behaves inductively at low RF powers and transitions to capacitive load as RF power is increased in presence of a transverse magnetic field of 7.0 mT.

It is also observed that the condition of resonance also changes with the neutral gas pressure inside the vacuum chamber. A plot of RF power at resonance condition P_{res} is plotted in Fig:5.3 for different operating pressures. It is seen that the power at which resonance is obtained is higher for lower operating pressures. The underlying reason for it is presented in the discussion section of this chapter.

5.3.1 Series Resonance for lighter/responsive ions

In this experimental study; we also report a resonance condition in the second experimental setup i.e. Cylindrical CCRF discharge. The observed resonance is for helium

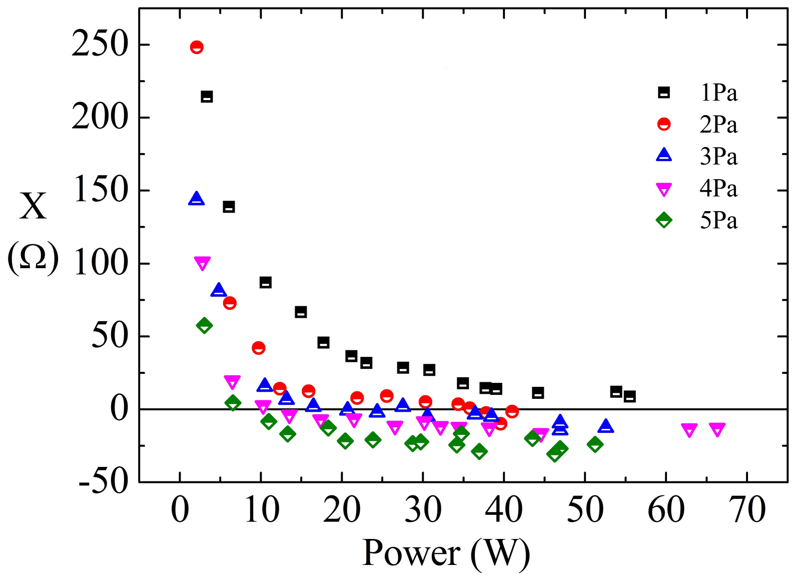

Figure 5.2: Plasma reactance for different neutral gas pressures at 7.0 mT transverse B-field

discharge at 1.0 Pa of neutral gas pressure where a transition in discharge reactance from inductive to capacitive is seen at relatively higher magnetic fields of 25.2 mT and powers above 70 W. The reactance are plotted in the fig 5.4 for different axial magnetic fields with increasing RF power levels. The observed resonance differs from the one observed in transversely magnetized parallel plate discharge; as in that case the resonance is governed by the electron conductivity only. It is not straight forward to derive a theoretical expression for series resonance in this case due to radially expanding and collapsing sheaths as well as responsive ions to the RF fields. However, a qualitative analysis for the observed resonance could be provided as follows;

In this case the resonance condition is governed by the electrons as well as ions. For the given plasma density the condition of low frequency sheaths is satisfied i.e. $\omega_{pi} \approx \omega_{rf}$. Therefore, the ions also respond to the RF fields leading to very thin sheaths [11] [Section:11.5 of Ref [11]]. As the sheaths are very thin is such a case, the capacitive reactance of the sheath is also small. On the other hand the bulk plasma inductance ($L_p \propto L/A$) in the cylindrical CCRF system is large due to source design. The ratio of plasma length over cross-section i.e. L/A is about 50 times in cylindrical CCRF system

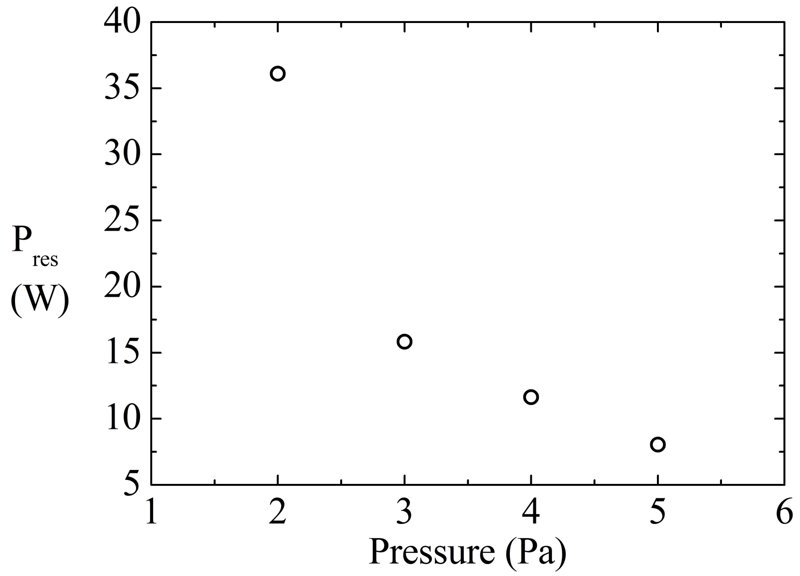

Figure 5.3: RF Power levels at resonance condition Vs Pressure

as compared to parallel plate setup.

The effect of magnetic field and the RF power on the discharge impedance in this setup is only expected to reveal itself in the plasma density (inductive reactance) as the external axial magnetic field remains parallel to the plasma bulk electric field making the bulk plasma conductivity independent of B-field. As the plasma density increases with the RF power and with the magnetic field due to confinement of electrons the reactance correspondingly falls as seen in 5.4. Consequently a series resonance is observed for sufficiently high RF power and the magnetic fields. The observed resonance in this case is due to the enhanced inductive reactance created by the source geometry as well as the effect of responsive ions of the cylindrical sheaths. Therefore, the apparent reason for inducing this resonance condition is the dynamics of the responsive helium ions to the RF fields and not due to the transverse magnetic fields as is the case in parallel plate setup.

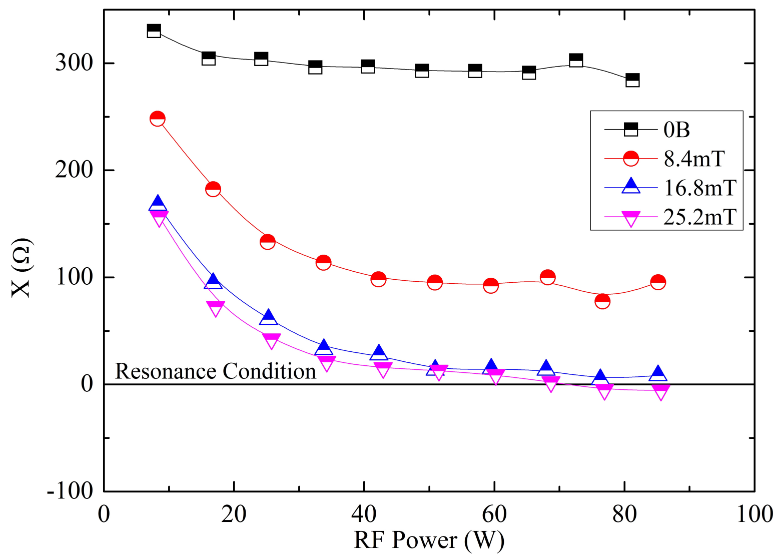

Figure 5.4: Plasma reactance for different axial magnetic fields at 1.0 Pa helium discharge

5.4 Discussions

The existence of series resonance is marked by the transition of discharge reactance from positive to negative values which is observed for both the experimental setups for different gases and magnetic fields. For the parallel plate setup; the ESR condition for transversely magnetized plasma is given by Eq: 5.15. i.e.

$$\omega_{res,B} = \omega_{pe}\sqrt{s/d}[\frac{\nu_m^2+\omega^2}{\Omega^2-(\nu_m^2+\omega^2)}]^{1/2} = \omega_{res}[\frac{\nu_m^2+\omega^2}{\Omega^2-(\nu_m^2+\omega^2)}]^{1/2}$$

This equation for $\omega_{res,B}$ is a implicit function of ω and therefore can be written in the form $\omega_{res,B} = \beta\omega_{res}$ where,

$$\beta = [\frac{\nu_m^2+\omega^2}{\Omega^2-(\nu_m^2+\omega^2)}]^{1/2} \quad (5.18)$$

Substituting $\omega = 85.2\times10^7 rad/sec$ for a 13.56 MHz discharge and $\Omega = 1.23\times10^9 rad/sec$ (7.0 mT) in Eq: 5.18; we can plot the value of β as a function of collision frequency ν_m. The range of the collision frequency is chosen for the experimental pressure regime of 1.0 to 5.0 Pa. Such a plot is shown in Figure 5.5;

As seen from the plot in Figure 5.5 β increases with ν_m. However we know that for

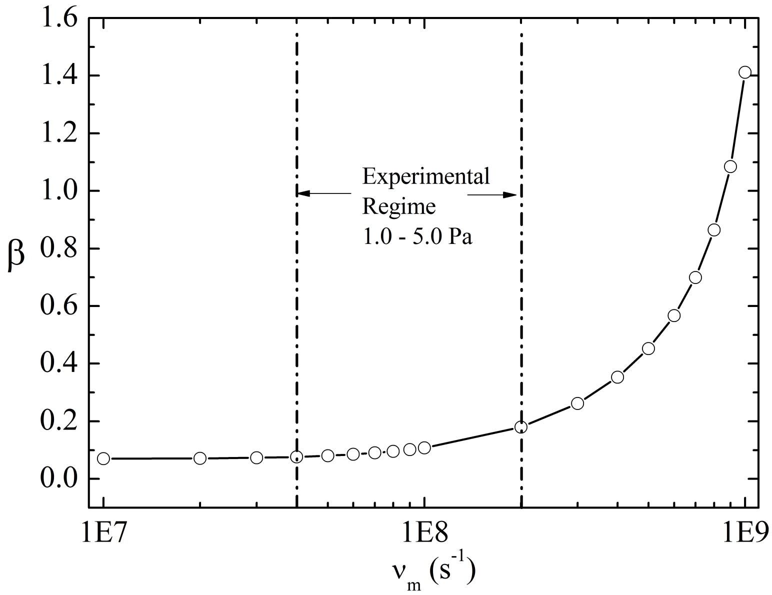

Figure 5.5: Plot of $\beta(\nu_m)$ as a function of collision frequency

the observed experimental resonance condition is at a fixed RF frequency of 13.56 MHz $\omega_{res,B} = \beta\omega_{res} = 8.52\times10^7 rad/sec$. While in the experimental pressure range of 1.0 to 5.0 Pa, β ranges from 0.1 to 0.3 and therefore ω_{res} ranges from 850-284 $\times10^6 rad/sec$. The corresponding electron plasma frequency therefore varies as $\omega_{pe} = \omega_{res}\sqrt{d/s}$; Assuming $\sqrt{d/s} \sim 4$, this gives an estimate of electron density $n_e \sim 0.36\times10^{16}m^{-3} - 0.4\times10^{15}m^{-3}$ corresponding to ω_{res}. The obtained values of n_e reasonably agree to the densities observed in a typical parallel plate CCRF discharges.

Moreover, we have seen in Fig 5.3, that RF power at resonance condition falls as the pressure is increased. Since RF power is proportionate to $n_e(\omega_{pe})$; therefore $\omega_{res} = \omega_{pe}\sqrt{s/d}$ is also expected to fall with pressure. This implicitly suggests that for β value must proportionately increase with pressure to satisfy the resonance condition $\omega(f = 13.56MHz) = \beta\omega_{res}$ which is seen in the plot of β. Therefore, the experimental result is in qualitative agreement with the conductivity model.

5.4.1 Role of transverse B-field in inducing resonance at lower RF frequency

It is necessary to understand the underlying reason for observing resonance condition in transversely magnetized discharge. If we consider Eq: 5.13 for the plasma impedance we have;

$$Z = Z_B + Z_s = \frac{d}{A\sigma_{\perp}} = \nu_m L_p[1 + \frac{\Omega^2}{\nu_m^2 + \omega^2}] - j\omega L_p[1 - \frac{\Omega^2}{\nu_m^2 + \omega^2}] - \frac{s}{jA\omega\epsilon_0}$$

Again, focusing only on the complex part of the equation;

$$X = -j\omega L_p[1 - \frac{\Omega^2}{\nu_m^2 + \omega^2}] - \frac{s}{jA\omega\epsilon_0}$$

In the above equation the last term is the capacitive reactance due to sheath. This term is same as seen for the un-magnetized plasma in Eq: 5.4. The first term of the equation however, is different from the un-magnetized plasma case. In presence of magnetic field a factor $\alpha = -[1 - \frac{\Omega^2}{\nu_m^2+\omega^2}]$ is introduced with $j\omega L_p$ (inductive reactance of the bulk plasma for un-magnetized plasma).

Substituting values of $\Omega = 1.23 \times 10^9 rad/sec$ (7.0 mT) and ν_m (as shown in Figure5.5) for the experimental pressure range; we get $\frac{\Omega^2}{\nu_m^2+\omega^2} >> 1$ and therefore $\alpha >> 1$. As $\alpha >> 1$ is multiplied with the inductive reactance term $j\omega L_p$, the inductive reactance is much enhanced in presence of a transverse magnetic field. The overall effect is that the inductive reactance of the bulk plasma becomes comparable to the usually dominant capacitive reactance of the sheaths so that a resonance condition could be achieved at a lower frequency of 13.56 MHz RF frequency.

The fundamental principle for observing resonance is however same as the one which was obtained at 81.36 MHz by Godyak and Popov. They enhanced the inductive reactance of the bulk plasma 6 times by increasing the frequency 6 times ($X_p \propto \omega$); while also reducing the capacitive reactance 6 times ($X_{sh} \propto 1/\omega$). Therefore, increasing the frequency has a 36 times effect on the discharge reactance. Similar, effect in magnetized case is introduced by α factor as for $\Omega = 1.23 \times 10^9$ (7.0 mT) $\approx 10^9$ collision frequency $\nu_m \approx 10^8 sec^{-1}$ and $\omega = 8.52 \times 10^7 \approx 10^8$ the value of $\alpha = 100$. Therefore, in the magnetized plasma case, only the bulk inductance is enhanced 100 times to match with the high capacitive reactance of the sheaths.

Other-way to understand this is that in high frequency resonance the capacitive voltage drop across the sheath is lowered; while the inductive voltage drop is increased to cancel each other, However in the magnetic field induced resonance the only the inductive drop is increased by α factor. Therefore, it is inferred that in transversely magnetized plasma the voltage drop across the plasma bulk is much higher than in case of high frequency resonance condition. Intrinsic effect of this would be on the electron bunching near the sheaths as seen by Qiu [75]. The electrons would oscilate from sheath to sheath under the influence of this inductive voltage drop as simulated by Qiu. Higher inductive voltage drop would accelerate the electrons to very high energies causing improved ionization along the way leading to high plasma density operation at lower neutral gas pressures.

5.4.2 Practical implication of modified magnetized ESR condition

The practical implication of the transverse magnetic field induced series resonance could be understood from Eq: 5.15 itself;

$$\omega_{res,B} = \omega_{pe}\sqrt{s/d}[\frac{\nu_m^2+\omega^2}{\Omega^2-(\nu_m^2+\omega^2)}]^{1/2} = \omega_{res}[\frac{\nu_m^2+\omega^2}{\Omega^2-(\nu_m^2+\omega^2)}]^{1/2}$$

In the above equation, experimentally, $\omega_{res,B} = \omega$ is fixed by the supply frequency. i.e. $\omega_{res,B} = 8.52 \times 10^7 rad/sec$ for a 13.56 MHz supply frequency. Plasma density (ω_{pe}) and the pressure (ν_m) is usually determined by the substrate process requirements and therefore it can be given as an input to the equation. If we assume a value of sheath thickness s and substitute all these values in the above equation; we can solve to obtain the value of Ω – electron cyclotron frequency for which a resonance condition would be observed. Therefore, this equation gives a blue-print on using the magnetic field as a control parameter to precisely create a condition of series resonance.

5.5 Summary and Conclusions

To summarize, we have devised an equation of ESR in a transversely magnetized CCRF discharge; which can be the basis for designing a CCRF discharge setup wherein magnetic field could be used as a controlling parameter to induce the resonance conditions. The role of pressure, RF power, ion response to RF fields, plasma source dimensions in determining the plasma impedance is deliberated. This chapter follows up on the conclusions of chapter-4; which showed the effectiveness of transverse magnetic field in controlling the RF power coupling into individual plasma species inside the discharge.

In conclusion, the resonance condition in a CCRF discharge could be achieved with help of external means such as magnetic fields as well as the plasma discharge configuration. The observed resonance condition in the cylindrical CCRF setup also suggests that the discharge configuration (Ratio of L/A) and the ion dynamics also plays a vital role in determining the resonance condition. In case of responsive ions to the RF fields $\omega_{pi} \approx \omega_{rf}$; the theoretical modeling becomes very complex owing role of ion in determining the overall plasma conductivity in the plasma bulk as well as the sheaths.

The theoretical as well as simulation study of ESR in presence of responsive ions is still an open problem; with no literature available on the topic; while the experimental work in the thesis gives an insight into the problem. The problem is of importance as higher frequency CCRF discharges (60 MHz) are now being operated for plasma processing; which challenges the stationary ion assumption in the plasma bulk. The responsive ion would completely change the plasma dynamics; moreover the higher frequency discharges (60

MHz or above) introduces the electromagnetic effects along the discharge electrodes in a CCRF discharge [79]; which would also change the plasma behavior and the impedance.

Chapter 6

Characteristics of a capacitive coupled magnetized plasma column

This chapter presents in detail the impedance characteristics of a magnetized plasma column created by a set of capacitive coupled cylindrical electrodes in presence of axial magnetic field. The objective was to create an elongated plasma column in presence of higher magnetic fields. The interaction between the capacitive RF electric field with stationary magnetic field for creating an elongated magnetized plasma column is fundamentally motivated towards plasma formation at low operating pressures in cylindrical and toroidal plasma devices. Elongated plasma in a linear device is particularly important; as high density plasmas confined in an axial magnetic field assists to be a significant tool for investigating many basic phenomena in laboratory plasmas [80] [81] such as cross-field transport of charge particles to oblique magnetized sheaths [78][82] [83]. The interaction between the RF driven electrodes in presence of oblique magnetic field leads to anomalous heating of antenna surfaces in ICRF heating antennas applied in tokomak [84]. Improvised experiments to study effect of electrode biasing in magnetized plasma column with implications in tokamak discharge have been conducted; elongated plasma with minimal gradients and curvatures in presence of magnetic field can mimic scrape of layer (SOL) region [85] [86] existing near the plasma facing components such as diverter/limiters in tokamaks [87]. Moreover, the magnetization effects on CCRF plasma may well be more pronounced in other electrode geometries than a parallel plate system . Additionally, the azimuthally closed $\vec{E}\times\vec{B}$ drift inside the hollow cylindrical electrodes would also enhance the ionization; similar to a hall current in hall thrusters [76].

This chapter applies the impedance measurement technique described in chapter-3 to reveal the properties of magnetized plasma column produced by a set of cylindrical electrodes operated in push-pull configuration. The impedance measurements are associated with the direct measurement of radial plasma density n_0 and electron temperature T_e obtained using the hybrid electric probe [31]. Using the above information, the role of external magnetic field on the plasma uniformity due to azimuthally closing $\vec{E}\times\vec{B}$ drifts generated near the cylindrical sheaths is discussed. A correlation between the local plasma density n_0 and electron temperature T_e measured at the radial center of the plasma column and the gross externally measured impedance is recognized.

6.1 Uniform plasma column formation in cylindrical CCRF plasma source

The cylindrical CCRF plasma source described in Chapter-2 has been used for the present investigation. The discharge is sustained by applying the RF potential to the extreme cylinders with respect to the central electrode. The external magnetic field is applied along the axis of the hollow cylinders. This geometry not only helps to close the $\vec{E}\times\vec{B}$ drift current, it also allows an axial current for sustaining a plasma column between these electrodes.

Fig 6.1 shows the schematic of the setup detailing the manner in which the currents between the electrodes are closed due to application of magnetic field. Briefly, the three cylindrical electrodes are placed at fixed axial locations inside the linear vacuum chamber. The intense radial electric field inside the sheaths is transverse to the axial magnetic field. This gives rise to a localized azimuthally closed electron drifts; while axial currents are generated to provide the current continuity between the discharge electrodes.

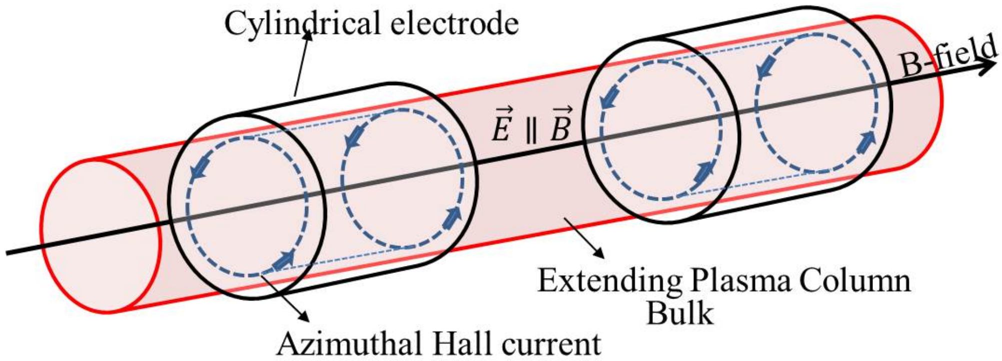

Figure 6.1: Schematic of the cylindrical plasma column

Fig 6.2, shows the photographic images of the elongated plasma column. A direct (Front) view of the column shows that the plasma is radially more intense at large radius than at the center. This is caused because the ionizing electrons undergo a closed $\vec{E} \times \vec{B}$ drift in the vicinity of the radial sheaths. The RF current between the consecutive electrodes however does not have this drift because the bulk electric field in the plasma column is along the magnetic field i.e $\vec{E} \parallel \vec{B}$ between the axially separated electrodes.

6.1.1 Magnetized plasma column

The front (axial) and the side photographs taken from outside the vacuum chamber for argon discharge are shown in Fig 6.2 (a) to (f) for increasing axial B-field at a fixed RF power level of 60 W. From, the visual images it can be seen that as the magnetic field is increased the radial confinement of the plasma column is seen to increase to form a well-defined cylindrical plasma column. It is also worth noting that with the increase in B-field, an intense bright annular ring of plasma inside the hollow cylindrical electrodes tends to shrink in radial width and shifts more closer towards the cylindrical surface as the

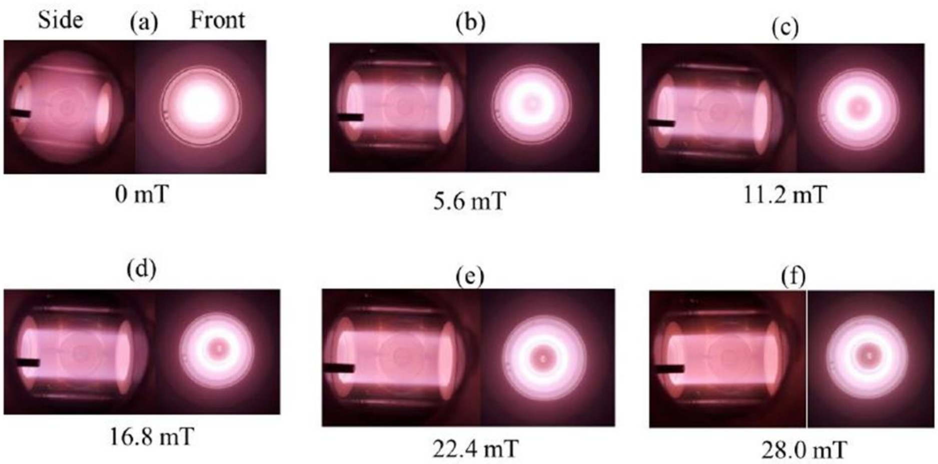

Figure 6.2: Side and front views of argon plasma column in cylindrical CCRF discharge

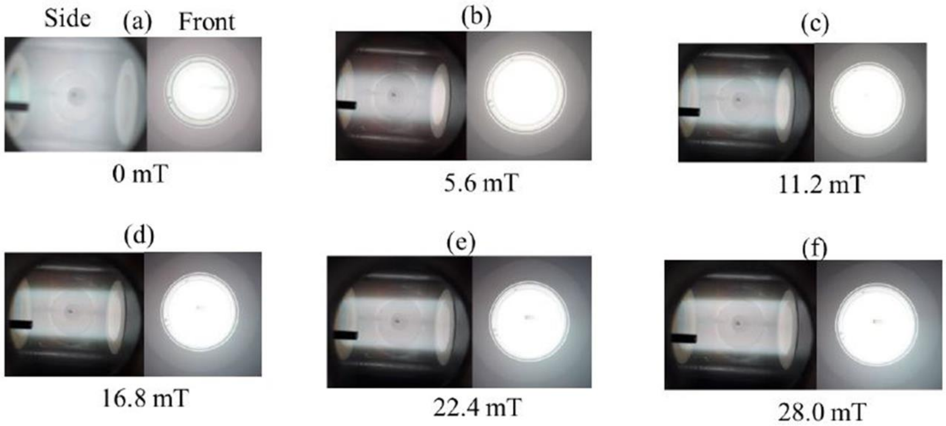

Figure 6.3: Side and front views of helium plasma column in cylindrical CCRF discharge

$\vec{E} \times \vec{B}$ drift currents becomes localized near the sheaths. Fig 6.3 (a)-(f) shows similar plots for a helium plasma column. Although, the effect of B-field on the radial confinement is similar to the argon discharge, however, as it can be seen from the front views that the plasma column is homogeneous irrespective of the applied magnetic field. The reason for such behavior in helium is discussed in the upcoming sections.The radial homogeneity is visible to the naked eye; while the photographs presented in Fig: 6.3 becomes highly saturated unlike the argon plasma.

6.2 Experimental results and Discussions

To characterize the magnetized plasma column; three externally measured electrical parameters are plotted in Fig 6.4 . The three basic parameters 1) discharge voltage V_{dis}, 2) Plasma current I_p and 3) the power factor $cos\phi$; for argon and helium discharges with increasing magnetic field strengths for different set RF power levels are shown. The product of these parameters provides the actual power delivered to the discharge; which is about $80 - 85\%$ of the set power for the present experimental setup.

From, these plots it is seen that at a constant B-field, the RF voltage and Current for both argon/helium discharge column increases with increase in set RF power level. In contrast we observe that for a fixed RF power level the RF voltage tends to fall while the RF Current increases with increase in B-field. The power factor values obtained in Fig 6.4a for argon are due to capacitive phases (-ve Reactance); while in Fig 6.4b in helium are due to inductive phase (+ve Reactance). The inductive behavior observed for Helium CCRF discharge is a notable result and is discussed with the impedance plots in Fig 6.5b of the plasma column. The power factor values in argon as seen in Fig 6.4a falls initially and then increases with B-field. In case of helium discharge the power factor values tends to increase consistently with B-Field; and a resonance is seen when $cos\phi = 1.0$ as the magnetic field strengths increases. From, these electrical parameters we obtained the discharge reactance and discharge resistance as per procedure described in chapter-3. The power factor values for both the discharges are seen to be high (0.65-1.0) for a capacitive coupled plasma. The discharges with such high values of power factor are called near resonant discharges [75]. The higher values of the power factor in a typically capacitive reactance dominant system is due to the dimension of the plasma. Since, bulk plasma inductance $L_p \propto L/A$; where L-plasma length and A-plasma cross-section; it is expected that the inductive reactance is significantly higher if the length of the plasma column is large. In this case, the inductive reactance of the bulk plasma compensates for the usually dominant capacitive sheath reactance giving rise to higher values of power factor close to

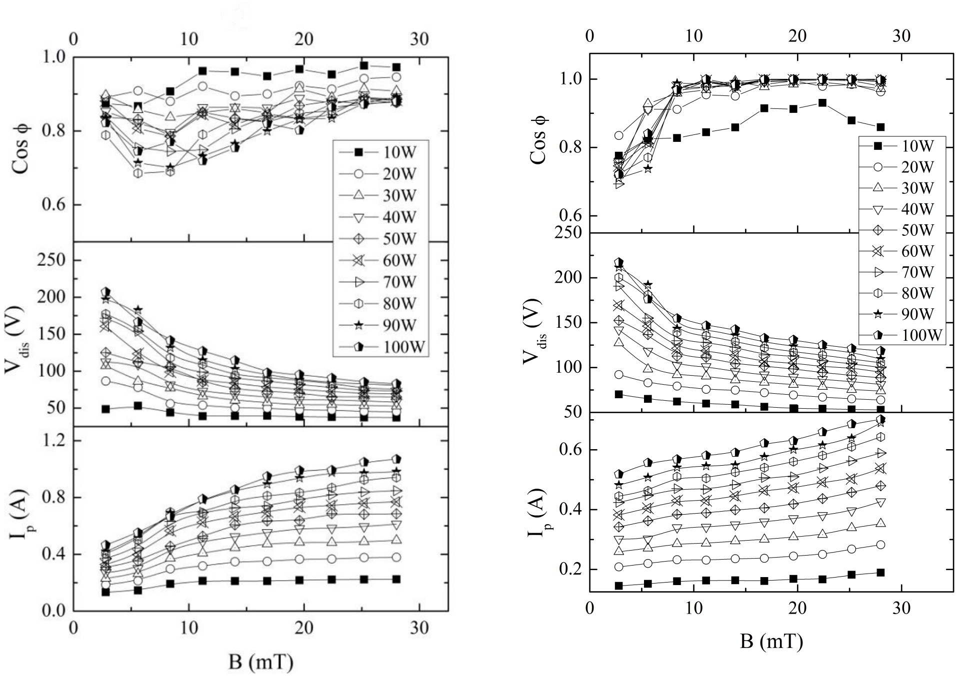

(a) Argon (b) Helium

Figure 6.4: Plot of electrical discharge parameters Vs. B-field

1. For comparison, the ratio of L/A of the cylindrical setup is almost 50 times higher than the parallel plate system and therefore this plasma is not strongly reactive in nature.

6.2.1 Impedance characteristics

The real ($\backslash resistance$) and imaginary ($\backslash reactance$) part of the impedance for the argon and helium discharge column are plotted as a function of increasing axial B-Field for different set RF power levels in Fig 6.5. The resistance R is due to power dissipation in the plasma and inside the sheaths; while the plasma reactance is due to the bulk plasma inductance in series with the sheath capacitance. Therefore, the reactance $X = \omega L_p - \frac{1}{\omega C_{sh}}$. In Fig 6.5a , it is observed that the resistance R for argon falls quickly initially with increase in magnetic field. However, as the magnetic field increases above 15.0 mT, the rate of fall slows until a saturation value of R is reached around 100 – 200 Ω . The fall in case of helium is however found to be monotonic in nature. As for fig 6.5b, the discharge reactance X is found to be capacitive in argon and inductive in helium.

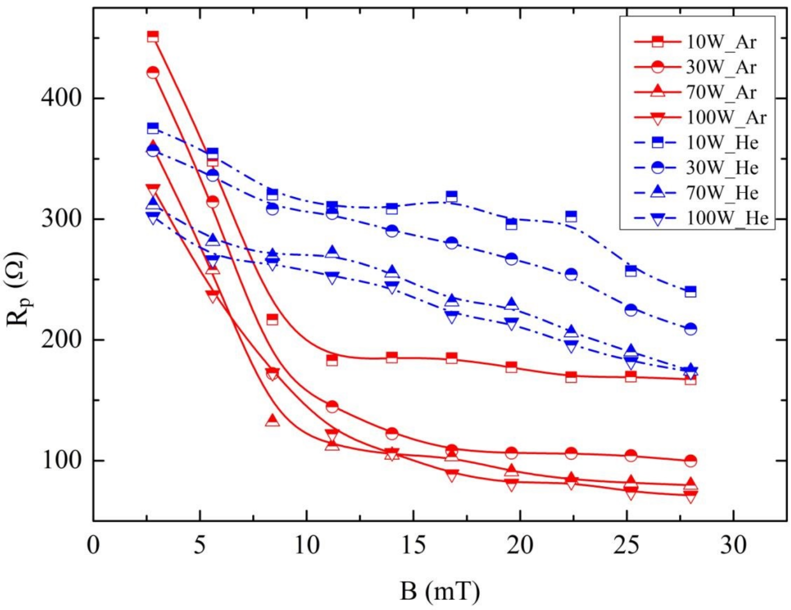

(a) Resistance

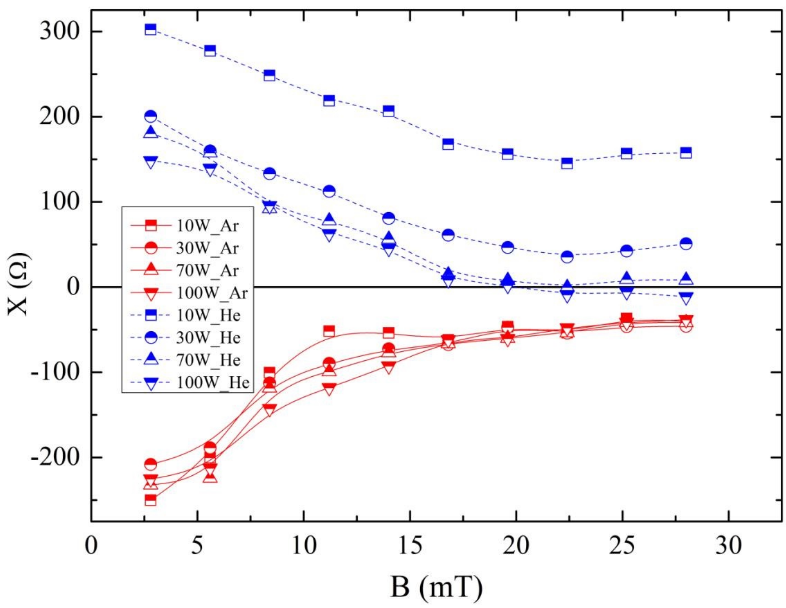

(b) Reactance

Figure 6.5: Impedance characteristics for different set RF powers levels with increasing B-fields

Fig:6.6 plots plasma parameters (n_0 and T_e) Vs. B-Field for an array of RF power levels in a) argon and b) helium at the radial center of the plasma column. Trends in Fig:6.6 showed that for a fixed RF power level the plasma density increased with magnetic field whereas electron temperature T_e decreases. It is also seen that the central plasma density does not increase significantly with rise in RF power levels.

Insights into the phenomenology of the argon discharge are given by combining plots in Fig:6.5 and Fig:6.6 ; where it is seen that the fall in resistance is concurrent with increased conductivity (/density) and therefore the measured plasma density trend and the externally measured resistance trends concur well. Electron temperature T_e on the other hand is seen to be directly linked to increase in RF power coupled to the plasma discharge.

The complex reactive impedance plots in Fig 6.5b also divulges stimulating intrinsic behavior of the discharge. In argon, the measured reactance was negative; while its magnitude decreased with increase in magnetic field and is almost independent of the RF power. Like the resistance, the discharge reactance plot also exhibit a saturating nature as the B-field is increased above 15.0 mT. The initial fall in the magnitude of the reactance could be due to either decrease in capacitive reactance or increase in inductive reactance of the bulk. However, it is known that the bulk plasma inductance L_p varies inversely with electron density n_e [11]. Therefore, it is not a plausible explanation for decreasing magnitude of reactance based on the plasma density measurements plotted in Fig 6.6a. The capacitive reactance on the other hand is determined by the sheath width $s \propto V/I$ [11] [16]. As per plot in Fig 6.4a, the voltage falls significantly with increasing B-field; which will lead to smaller sheath widths. The capacitive reactance hence reduces in magnitude due to decrease in sheath widths. A decreasing sheath width due to increase in magnetic field is consistent with the results reported by You and Sharma [6] [7]. Thus it can be concluded that the fall in capacitive reactance of the sheaths is dominant over the change in inductive reactance of the bulk plasma.

In helium discharge, an opposing trend in reactance is seen as compared with the case

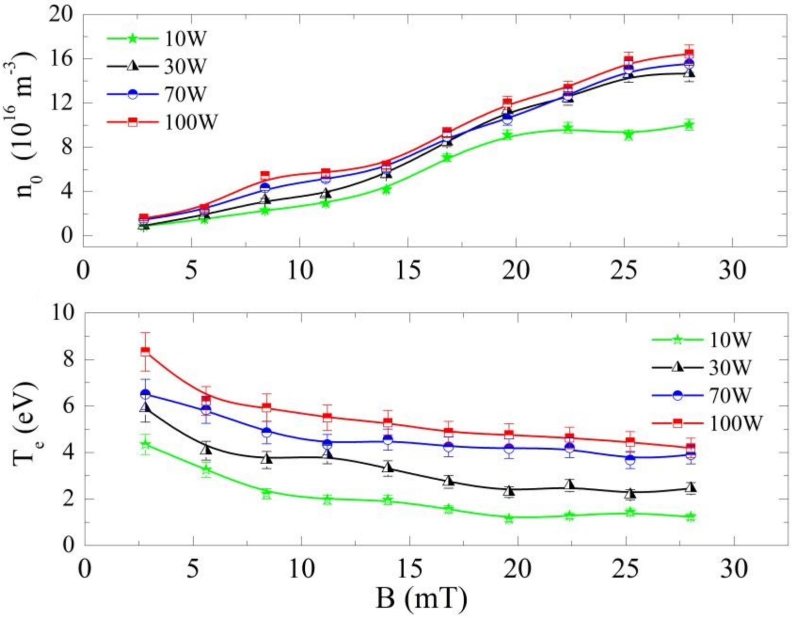

(a) Argon

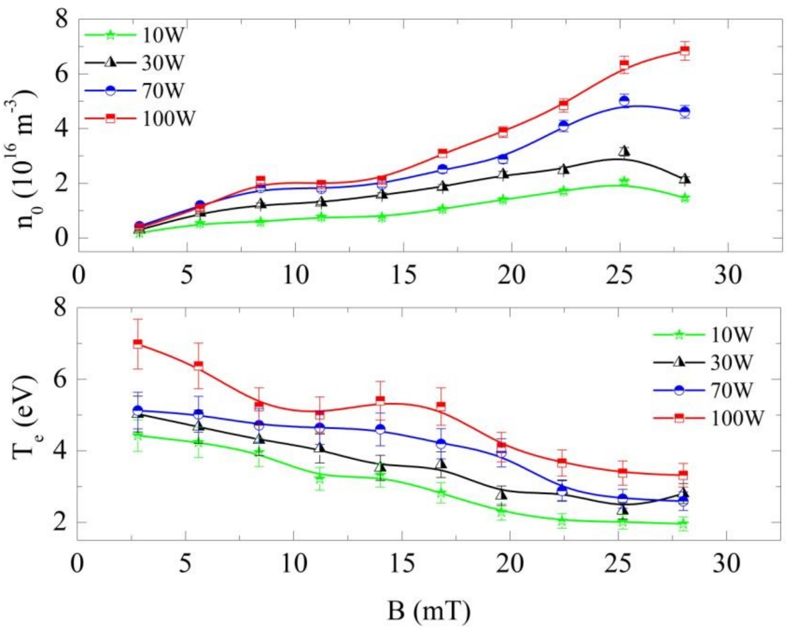

(b) Helium

Figure 6.6: Plasma Parameters with B- field for range of RF powers

of argon discharge (c.f fig 6.5b)where the magnitude of the reactance decreases with B-field. For the helium discharge, the reactance is found to be primarily inductive. Since, the helium ions are lighter than argon as a result, the ion time scale for typical plasma density of $10^{16} m^{-3}$ is close to the RF time scale for 13.56 MHz. Consequently, the helium ions are able to follow the instantaneous RF potential in the sheaths unlike in argon; which can only respond to time averaged DC potentials inside the sheaths. Therefore is is expected that in the case of helium discharge the sheaths are resistive in nature [11]. Consequently, the capacitive reactance of the sheaths are negligible for helium and therefore, the inductive reactance of the bulk dominates as seen in Fig 6.5b. The sheath widths are correspondingly smaller in helium as compared to argon [11]. This result is also consistent with the visual observation in Fig 6.3; which showed no ring like structure in the visual image of helium plasma column as B-field was increased. Since, sheath widths are very small, the effect of $\vec{E} \times \vec{B}$ drift near the sheaths is also not discernable. Furthermore, as the plasma density increases, the inductive reactance inside the bulk plasma will reduce. Therefore resonance condition can be seen for stronger magnetic fields, which has been discussed in chapter-5.

The primary reason for observing the rise in plasma density with B-field in Fig 6.6 can be attributed to enhancement in collisions introduced by the magnetic field. The electrons are confined by the external magnetic field and the gyro-motion along the magnetic field lines can increase the probability of collisions with the background atoms. As given in Ref [5]; an effective pressure $P_{eff} = P_g + \alpha(\frac{B^2}{P_g})$ was introduced which is analogous to increase in collisions introduced by the magnetic field. Here, α is a constant factor and P_g is the actual neutral gas pressure (present case P =1.0 Pa). The improvement in power coupling efficiency in presence of magnetic field inside a discharge is well-known [11] [16]. This result is also in agreement with the power-mode transition discussed in chapter-5; which demonstrated that with increase in B-field; higher fraction of the set RF power was coupled to plasma electrons. In the case of cylindrical electrode the gross electric field inside the bulk plasma points radially outwards and more strongly adjacent

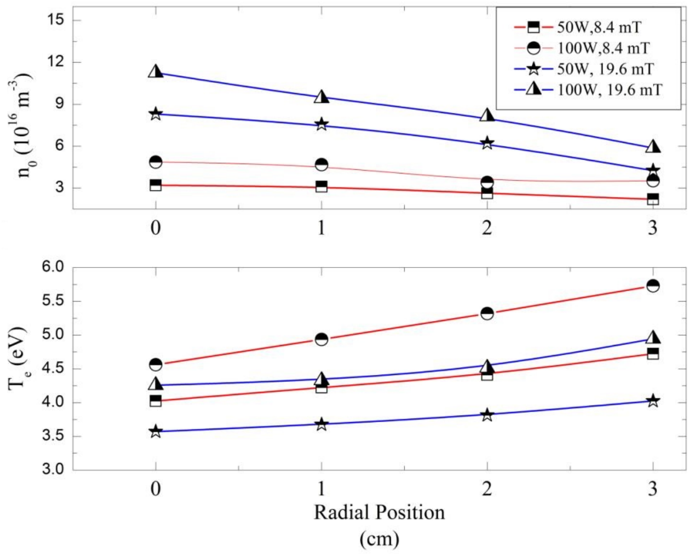

(a) Argon

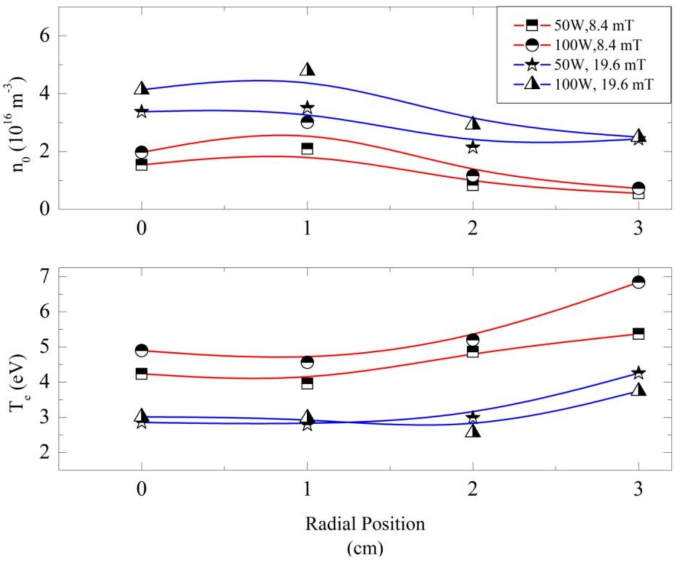

(b) Helium

Figure 6.7: Radial Plasma density and electron temperature

to the inner electrode surface. Therefore the electric field is perpendicular to the external magnetic field . The energetic electrons therefore azimuthally orbits due to $\vec{E} \times \vec{B}$ drifts near the inner periphery of the electrode surface and provides non-local heating close to the cylindrical surface. Magnetically induced non-local heating of electrons was earlier reported in a simulation study in a parallel plate setup [88]. However with the increase in B-field; it becomes difficult for the energetic electrons near the electrodes to transport radially across the magnetic field lines towards central plasma region; thus they remain confined in the periphery of the cylindrical column. This characteristic can be observed from the radial plots of the electron temperature; measured between two axially located cylindrical electrodes.

In Fig 6.7, the radial plasma density and electron temperature T_e for argon and helium discharges are plotted. It is clearly seen that the T_e is peaked at radial position of 3.0 cm. This high temperature region is along the magnetic field lines passing close to the inner surface of the cylindrical electrodes at a radial distance of 3.25 cm. The plasma density however shows an inverse trend since the hotter electrons tends to diffuse more rapidly along the axial B-field. For the radial profiles of plasma density and electron temperatures plotted in Fig 6.7; the dependence on B-Field and RF power level shown for central density and temperature measurements in Fig 6.6 remains consistent.

The rise in T_e with RF power level; is fundamentally due to enhanced voltage drops across the sheaths as seen in Fig 6.4. The electrons primarily gain energy from the rapidly oscillating RF potential across the sheath. The energetic electrons interact with the background neutral gas and thermalized by elastic and inelastic collision process close to the electrode surface. The increase in local electron temperature near the electrode is not seen to affect the plasma density significantly as the particle loss by diffusion is also expected to rise due to the ambi-polar electric field along the magnetic field.

The impedance plots for argon discharge in Fig 6.5 shows a saturation in the values of resistance as well as the reactance on increasing the B-field strength above 15.0 mT. The corresponding electron larmor radius R_L were also plotted in Fig 6.8 considering the electron temperature T_e values for the range of applied magnetic field. We also observe a similar trend in R_L showing a saturation value as the magnetic field strength increases above 15.0 mT. Therefore as far as magnetization is concerned, we observe no significant

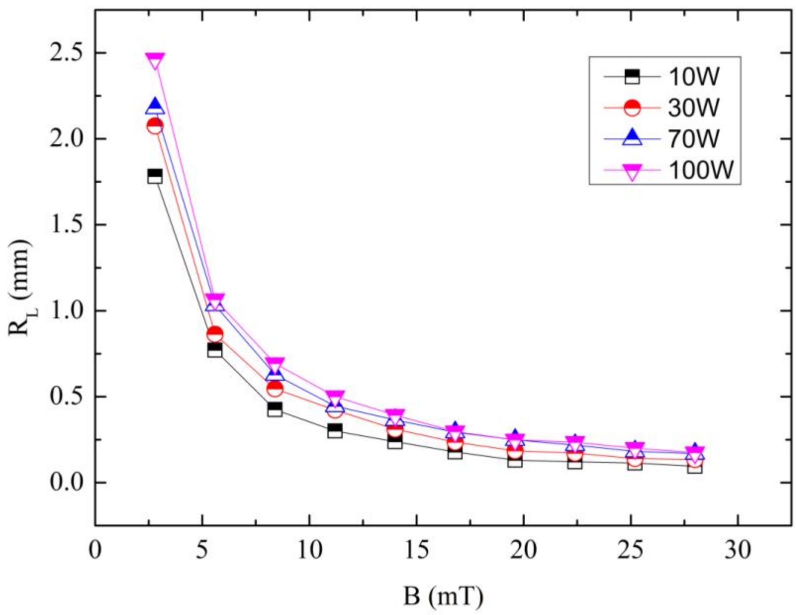

Figure 6.8: Larmor Radius R_L Vs. B-field

change in impedance characteristic above B = 15 mT. Therefore for observing a prominent change above 15.0 mT in discharge impedance, the magnetic field must be strong enough to influence the ions. Hence, the trend in R_L parameter with the applied magnetic field can provide key inputs for designing the magnetized plasma system and the impedance matching range for the plasma load due to external magnetic field.

6.3 Summary and Conclusions

In summary, a magnetized plasma column produced by a set of hollow cylindrical electrodes in a linear plasma device is presented. The characteristic effect of ion mass on the discharge properties is demonstrated by considering argon and 10 times lighter helium gas within the same discharge setup. A dramatic change in the discharge impedance characteristic is revealed from this study; it is found that in the case of argon, the sheath reactance is dominant whereas bulk plasma inductance is dominant in the case of helium. Low frequency resistive sheaths for helium discharge in the presence of magnetic field are revealed for the first time in this study through impedance measurements. The radial plots of plasma density reveal the characteristic difference in the plasma properties due to application of external magnetic field. The electron temperature is found to be peaked at the sheath edge due to confinement of energetic electrons in $\vec{E} \times \vec{B}$ Orbits near the electrode surface. The study also shows that the device has the potential to create axially sustained radially uniform plasma column along the magnetic field. The experimental results also demonstrate an increase in central plasma density with rise in magnetic field. It will be interesting to study in future, if such mechanism can be used to create toroidally confined plasma. The impedance measurements provides a key to understand the performance of magnetized sheaths, in particular such techniques can be useful to underpin the deleterious effect of magnetized plasma interaction with an RF driven electrode as encountered in ICRF antenna in fusion devices. The magnetic field can also be useful as an external parameter for controlling the plasma density and temperature inside the discharge. The impedance measurements of the discharge column confer with the intrinsic plasma density measurement, therefore the technique can be useful for inferring the relative change in the plasma density inside the magnetized plasma column.

Chapter 7

Summary, Conclusions and Future scope of work

The thesis was primarily motivated towards studying the effect of an external magnetic field on a capacitive driven CCRF discharge by non-invasive electrical measurements and analysis of its impedance characteristics. The impedance measurement technique is a highly useful technique used by process engineers for the characterization of plasma processing tools in microelectronics industries [9]. The application of this method to study the behavior of magnetized CCRF plasma has been attempted for the first time and it remain the focal point of the investigation. Using this technique some important results have been revealed such as, identification of electron-series-resonance at 13.56 MHz inside CCRF discharge setup, with magnetic field applied parallel to the electrode surface. The impedance measurement technique also reveals the power mode transition from a shift from linear to parabolic dependence from plots of $P_{dis}(I_{dis})$ [72]; Power mode transition is an unique characteristic of a CCRF discharge which tells whether the discharge power is coupled to plasma electrons or the positive ions inside the sheaths. A rigorous calibration and analysis of the passive measuring instruments (RF voltage/current probes) and the discharge set-up has been performed to compensate for the phase-delay in the voltage and current measurements by commercial probes as well as estimation of stray capacitance of the entire discharge set-up [70]. Theoretical analysis of the electrical equivalent circuit of the discharge explains the series resonance condition due to application of a transverse magnetic field to the CCRF discharge. It is found that the magnetic field can reduce the frequency range for observing the ESR effect by one order in magnitude. These results are detailed in Chapters 4, 5 and 6.

The impedance measurement method performed with cylindrical hollow electrodes with lighter helium gas reveals that the resistive nature becomes dominant over the reactive impedance as seen from power factor values $cos\phi$. This observation has been attributed to the positive ion response to the RF fields; since lighter helium ions are able to follow RF fields because the ion plasma frequency in this case become comparable with 13.56 MHz. It is important to highlight that the operation of CCRF discharge close to ion plasma frequency has seen very limited study; the impedance measurements are able to capture this behavior. It is also revealed that the plasma column tends to be more inductive in nature and compensates for the usually dominant capacitive effect due to sheaths. Therefore, the discharge tends to operate near resonance ($cos\phi$= 1) when created using a pair or isolated electrodes to form an extended plasma column over a long length. This particular mechanism is particularly useful to create uniform plasma column in a linear as well as toroidal machine. The sheaths formed in the presence of axial magnetic field which is transverse to the RF driven electrode surface can mimic the effect of near-field region of RF antenna that are used in tokamaks for plasma heating [24]. Recently linear plasma devices are being developed to study plasma surface interaction studies [84]. The linear plasma devices are also ubiquitously used to study various plasma phenomena in laboratories such as drift wave, magnetized mirror, cross-field transport [80] [85]. The cylindrical CCRF discharge can be potentially applied in linear device to create elongated plasma column.

The electrical impedance measurement performed in the cylindrical plasma device has been comprehended by supporting direct measurements of plasma parameters inside the discharge. For the measurement of plasma parameters two types of electric probe diagnostics have been introduced. The hairpin probe is a well known method to determine the electron density. Whereas to obtain the electron temperature a hybrid-type probe comprising of an emissive probe and triple probe has been designed to measure the radial plasma parameters in the cylindrical magnetized plasma column [31]. The experimental results clearly demonstrated the short-fall in the application of conventional triple Langmuir probe in contrast to the newly constructed hybrid probe. The hybrid probe also found deviation in the electron density obtained by hairpin as the magnetic field was increased.

A condition of electron-series-resonance (ESR) using 13.56 MHz RF driving frequency has been demonstrated for the first time in parallel plate CCRF discharge for plasma densities in the range of $10^{16} m^{-3}$ and magnetic field strength of 7.0 mT by varying the pressure regime from 1.0 to 5.0 Pa in an argon discharge. Through the calibrated non-invasive measurements of external power, the ESR condition could be established by observing the net reactive impedance of the discharge becoming zero under certain parameters, such that the discharge behaves as purely a resistive load. As found from the literature, the main advantage of working in an ESR condition is that [75]; (i) the operating RF voltage amplitude is minimum; (ii) the ion energy on to the substrate has a singly peaked distribution, which is a prime requirement for certain surface processes, (iii) the ionization enhances, that helps in operating the discharge at lower operating pressures; finally (iv) the RF matching also becomes easier.

The magnetic field introduced in this study reduces the frequency range for observing the ESR by almost 6 times, as compared to previously observed resonance in an unmagnetized discharge. Hence obtaining series resonance at commercially popular RF power frequencies such as 13.56 MHz simplifies working the discharge at ESR in industrial CCRF plasma reactors. A theoretical model to predict the ESR condition at different working pressures (Collision frequencies) and plasma density (RF power) by externally varying the B-field is also derived and verified in the experimental setups designed for specific objectives. To obtain the theoretical model of magnetically induced ESR condition; we used an electrical equivalent circuit of CCRF discharge in conjunction with the plasma conductivity in presence of magnetic field and the sheath capacitance model. It has been demonstrated that externally measured gross impedance characteristics cannot be trivially used to predict ESR and hence a system calibration of the experimental setup is inevitable to obtain the actual plasma impedances, which eliminates the effects of stray impedances associated with the discharge circuit during the measurements.

The overall findings can be briefly summarized in the following points:

The ultimate application for this research work would be in commercial CCRF processing reactors; as this work can be harnessed into a feed-back controlled system which controls the B-field to operate the discharge at ESR conditions with varying pressures and plasma densities as per process requirements.

In cylindrical CCRF source, a radially uniform plasma column is created, while electron temperature T_e tends to decrease towards the radial center of the plasma column. The effect of increase in RF power however shows an increment in T_e with a marginal increase in plasma density; whereas the central plasma density increases strongly with application of axial magnetic field. Therefore, the two parameters plasma density and electron temperature can be controlled almost independently in this setup by varying the applied magnetic field and RF power. The local measurements of plasma parameters carried inside the discharge tube have been comprehended with the help of a hybrid probe system. The hybrid probe is a unique apparatus developed by combining a double probe and an emissive probe. The hybrid probe has been calibrated/ benchmarked against well known resonance hairpin probe. The overall local plasma parameters obtained through the hybrid probe technique qualitatively supports the non-invasive plasma impedance measurements.

It is also established that the cylindrical magnetized CCRF discharge can show an inductive reactance. The inductive reactance of the bulk plasma is directly dependent on the length of the plasma column ($L_p \propto L/A$) where L- plasma length and A- cross-section of the plasma column). Due to the long plasma column, the inductive reactance dominates over the reactive impedance due to the sheath capacitance. This fact is supported with help of plasma impedance measurement, which shows an inductive phase for an unmagnetized CCRF plasma discharge. The axial magnetic field in the cylindrical electrode setup modifies the power mode transition and power coupling to the individual charge species (electrons/ions). A series resonance condition was observed in the case of helium discharge. This was possible as lighter ions of helium were able to respond to the time varying RF electric field inside the low-frequency sheaths ($\omega_{rf} \approx \omega_{pi}$); which are typically resistive sheaths [11]. This is an important experimental result as power coupling into ions in this frequency range is a matter of great interest and is still a topic of research; with major implications in RF heating schemes in tokomaks. A comparison between the magnetization effects on argon/helium plasmas highlights the role ion mass plays in the segregation of RF power between electrons and ions in CCRF plasma discharges. This is particularly important as the present commercial processing reactors are switching to higher operating frequencies (up to 60 MHz). The ion response in these setups then becomes important and, hence suitable ion mass may be introduced to achieve resonance in these setups.

To conclude, an experimental investigation of magnetization effects on the power coupling and its impact on the discharge load behavior has been preceded. The usefulness of the non-invasive electrical measurements in predicting intrinsic plasma behavior such as power mode transitions and electron series resonances has been demonstrated. Theoretical models have been developed to determine the operating plasma regime at which ESR condition can be achieved by introducing B-field. The magnetic field is shown to manipulate the discharge impedances strongly. A cylindrical plasma source has been developed with closed $\vec{E} \times \vec{B}$ drifts to work at stronger axial magnetic fields and create a uniform plasma column. The results show an almost linear increment in plasma density with increasing axial magnetic field and uniform radial plasma profiles in the bulk. It has also been experimentally shown that the magnetization has a strong dependence on the power coupling on individual plasma species and the ion response to the RF fields also impacts the power sharing between the species. Finally, it is concluded that further research on the topic is required to ultimately develop a feed-back control system based on magnetization for regulating CCRF plasma discharges.

Bibliography

[1] Yuri P Raizer, Mikhail N Shneider, and Nikolai A Yatsenko. *Radio-frequency capacitive discharges*. CRC Press, 2017.

[2] SJ You, SK Ahn, and Hong-Young Chang. “Study on the mode transitions for rf power dissipation in capacitively coupled plasma”. In: *Surface and Coatings Technology* 193.1-3 (2005), pp. 81–87.

[3] Jack W Coburn. *Plasma etching and reactive ion etching*. American Institute of Physics New York, 1982.

[4] T Lafleur et al. “Separate control of the ion flux and ion energy in capacitively coupled radio-frequency discharges using voltage waveform tailoring”. In: *Applied Physics Letters* 101.12 (2012), p. 124104.

[5] SJ You et al. “Power dissipation mode transition by a magnetic field”. In: *Applied physics letters* 81.14 (2002), pp. 2529–2531.

[6] SJ You et al. “Role of transverse magnetic field in the capacitive discharge”. In: *Thin Solid Films* 519.20 (2011), pp. 6981–6989.

[7] Sarveshwar Sharma et al. “Spatial symmetry breaking in single-frequency CCP discharge with transverse magnetic field”. In: *Physics of Plasmas* 25.8 (2018), p. 080704.

[8] Taisei Motomura et al. “Real-time characteristic impedance monitoring for end-point and anomaly detection in the plasma etching process”. In: *Japanese Journal of Applied Physics* 53.3S2 (2014), p. 03DC03.

[9] Masaaki Kanoh, Masashi Yamage, and Hiroyuki Takada. “End-point detection of reactive ion etching by plasma impedance monitoring”. In: *Japanese Journal of Applied Physics* 40.3R (2001), p. 1457.

[10] José A Bittencourt. *Fundamentals of plasma physics*. Springer Science & Business Media, 2013.

[11] Michael A Lieberman and Alan J Lichtenberg. *Principles of plasma discharges and materials processing*. John Wiley & Sons, 2005.

[12] Christopher Gerard Goedde, Allan J Lichtenberg, and Michael A Lieberman. “Self-consistent stochastic electron heating in radio frequency discharges”. In: *Journal of applied physics* 64.9 (1988), pp. 4375–4383.

[13] MM Turner. “Pressure heating of electrons in capacitively coupled rf discharges”. In: *Physical review letters* 75.7 (1995), p. 1312.

[14] MA Lieberman et al. “The effects of nonlinear series resonance on Ohmic and stochastic heating in capacitive discharges”. In: *Physics of Plasmas* 15.6 (2008), p. 063505.

[15] OA Popov and VA Godyak. “Power dissipated in low-pressure radio-frequency discharge plasmas”. In: *Journal of applied physics* 57.1 (1985), pp. 53–58.

[16] Pascal Chabert and Nicholas Braithwaite. *Physics of radio-frequency plasmas*. Cambridge University Press, 2011.

[17] J Taillet. “Resonance-sustained radio frequency discharges”. In: *American Journal of Physics* 37.4 (1969), pp. 423–441.

[18] R.W. Boswell T.Lefleur and J.P. Booth. In: *Appl.Phys.Lett 100,194191* (2012).

[19] Trevor Lafleur and Jean-Paul Booth. “Control of the ion flux and ion energy in CCP discharges using non-sinusoidal voltage waveforms”. In: *Journal of Physics D: Applied Physics* 45.39 (2012), p. 395203.

[20] Z Donkó et al. “PIC simulations of the separate control of ion flux and energy in CCRF discharges via the electrical asymmetry effect”. In: *Journal of Physics D: Applied Physics* 42.2 (2008), p. 025205.

[21] Julian Schulze et al. “The electrical asymmetry effect in multi-frequency capacitively coupled radio frequency discharges”. In: *Plasma Sources Science and Technology* 20.1 (2011), p. 015017.

[22] Shahid Rauf, Jason Kenney, and Ken Collins. “Three-dimensional model of magnetized capacitively coupled plasmas”. In: *Journal of Applied Physics* 105.10 (2009), p. 103301.

[23] S Binwal et al. “Triple and emissive probe measurements of plasma parameters in a magnetized capacitive coupled discharge”. In: *44th EPS Conference on Plasma Physics*. 2017.

[24] MPH Weenink. “Resonant energy absorption in the ion sheath of a plate antenna”. In: *Radio Science* 17.2 (1982), pp. 411–419.

[25] Robert L Merlino. “Understanding Langmuir probe current-voltage characteristics”. In: *American Journal of Physics* 75.12 (2007), pp. 1078–1085.

[26] Francis F Chen. “Langmuir probe diagnostics”. In: *IEEE-ICOPS Meeting, Jeju, Korea*. Vol. 2. 6. 2003.

[27] Francis F Chen. “Lecture notes on Langmuir probe diagnostics”. In: *Mini-Course on Plasma Diagnostics, IEEE-ICOPS meeting, Jeju, Korea*. Vol. 5. 2003.

[28] EY Wang et al. “Techniques for using emitting probes for potential measurement in rf plasmas”. In: *Review of scientific instruments* 57.10 (1986), pp. 2425–2431.

[29] R Schrittwieser and J Adámek. “J. mek, P”. In: *Balan, M. Hron, C. Ionita, K. Jakubka, L. Kryska, E. Martines, J. Stöckel, M. Tich, and G. Van Oost. Measurements with an emissive probe in the CASTOR tokamak. Plasma Physics and Controlled Fusion* 44.5 (2002), p. 567.

[30] Roman Schrittwieser et al. “Laser-heated emissive plasma probe”. In: *Review of scientific instruments* 79.8 (2008), p. 083508.

[31] JK Joshi et al. “A hybrid probe system for quantifying plasma parameters in a 13.56 MHz capacitive coupled magnetized plasma”. In: *Review of Scientific Instruments* 89.11 (2018), p. 113503.

[32] GD Hobbs and JA Wesson. “Heat flow through a Langmuir sheath in the presence of electron emission”. In: *Plasma Physics* 9.1 (1967), p. 85.

[33] Robert F Kemp and JMs Sellen Jr. “Plasma potential measurements by electron emissive probes”. In: *Review of Scientific Instruments* 37.4 (1966), pp. 455–461.

[34] JR Smith, Noah Hershkowitz, and P Coakley. “Inflection-point method of interpreting emissive probe characteristics”. In: *Review of Scientific Instruments* 50.2 (1979), pp. 210–218.

[35] Sin-Li Chen and T Sekiguchi. “Instantaneous direct-display system of plasma parameters by means of triple probe”. In: *Journal of Applied Physics* 36.8 (1965), pp. 2363–2375.

[36] CR Hoffmann and DJ Lees. “A differential method of measuring plasma potential”. In: *Plasma Physics* 13.8 (1971), p. 689.

[37] JP Sheehan and N Hershkowitz. “Emissive probes”. In: *Plasma Sources Science and Technology* 20.6 (2011), p. 063001.

[38] JP Sheehan et al. “A comparison of emissive probe techniques for electric potential measurements in a complex plasma”. In: *Physics of Plasmas* 18.7 (2011), p. 073501.

[39] RB Piejak et al. “The hairpin resonator: A plasma density measuring technique revisited”. In: *Journal of Applied Physics* 95.7 (2004), pp. 3785–3791.

[40] RB Piejak, J Al-Kuzee, and N St J Braithwaite. “Hairpin resonator probe measurements in RF plasmas”. In: *Plasma Sources Science and Technology* 14.4 (2005), p. 734.

[41] James W Bradley et al. “Resonance hairpin and Langmuir probe-assisted laser photodetachment measurements of the negative ion density in a pulsed dc magnetron discharge”. In: *Journal of Vacuum Science & Technology A: Vacuum, Surfaces, and Films* 29.3 (2011), p. 031305.

[42] GS Gogna and SK Karkari. “Microwave resonances of a hairpin probe in a magnetized plasma”. In: *Applied Physics Letters* 96.15 (2010), p. 151503.

[43] David J Peterson et al. “Electron neutral collision frequency measurement with the hairpin resonator probe”. In: *Plasma Sources Science and Technology* 26.9 (2017), p. 095002.

[44] Hiroshi Amemiya and Toshihiko Dote. “Cylindrical probe in a collisionless magnetized plasma”. In: *Japanese Journal of Applied Physics* 8.6 (1969), p. 818.

[45] Muhammad Yasin Naz et al. “Double and triple Langmuir probes measurements in inductively coupled nitrogen plasma”. In: *Progress In Electromagnetics Research* 114 (2011), pp. 113–128.

[46] K Jakubka, J Stoeckel, and F Zacek. *Measurements of the temperature in the edge plasma of the CASTOR tokamak by a triple Langmuir probe*. Tech. rep. Ceskoslovenska Akademie Ved, 1992.

[47] F Lockwood Estrin, SK Karkari, and JW Bradley. “Triple probe interrogation of spokes in a HiPIMS discharge”. In: *Journal of Physics D: Applied Physics* 50.29 (2017), p. 295201.

[48] Robert Eckman et al. "Triple Langmuir probe measurements in the plume of a pulsed plasma thruster". In: *Journal of Propulsion and Power* 17.4 (2001), pp. 762–771.

[49] Brian L Sands, Nicholas S Siefert, and Biswa N Ganguly. "Design and measurement considerations of hairpin resonator probes for determining electron number density in collisional plasmas". In: *Plasma Sources Science and Technology* 16.4 (2007), p. 716.

[50] R Chodura. "Plasma–wall transition in an oblique magnetic field". In: *The Physics of Fluids* 25.9 (1982), pp. 1628–1633.

[51] G-H Kim et al. "Magnetic and collisional effects on presheaths". In: *Physics of Plasmas* 2.8 (1995), pp. 3222–3233.

[52] David Coulette and Giovanni Manfredi. "Kinetic simulations of the Chodura and Debye sheaths for magnetic fields with grazing incidence". In: *Plasma Physics and Controlled Fusion* 58.2 (2016), p. 025008.

[53] Bornali Singha, A Sarma, and Joyanti Chutia. "Experimental observation of sheath and magnetic presheath over an oblique metallic plate in the presence of a magnetic field". In: *Physics of Plasmas* 9.2 (2002), pp. 683–690.

[54] M Keidar et al. "Magnetic field effect on the sheath thickness in plasma immersion ion implantation". In: *Applied physics letters* 81.7 (2002), pp. 1183–1185.

[55] Randy J Shul and Stephen J Pearton. *Handbook of advanced plasma processing techniques*. Springer Science & Business Media, 2011.

[56] E Schüngel et al. "The electrical asymmetry effect in geometrically asymmetric capacitive radio frequency plasmas". In: *Journal of Applied Physics* 112.5 (2012), p. 053302.

[57] U Czarnetzki, T Mussenbrock, and RP Brinkmann. "Self-excitation of the plasma series resonance in radio-frequency discharges: An analytical description". In: *Physics of plasmas* 13.12 (2006), p. 123503.

[58] BL Theraja and AK Theraja. *A Text-Book Of Electrical Technology*. Nirja Construction & Development, 1980.

[59] David M Pozar. *Microwave engineering*. John Wiley & Sons, 2009.

[60] Valery A Godyak, Robert B Piejak, and Benjamin M Alexandrovich. "Electrical characteristics of parallel-plate RF discharges in argon". In: *IEEE Transactions on plasma science* 19.4 (1991), pp. 660–676.

[61] VA Godyak and RB Piejak. "I nsitu simultaneous radio frequency discharge power measurements". In: *Journal of Vacuum Science & Technology A: Vacuum, Surfaces, and Films* 8.5 (1990), pp. 3833–3837.

[62] JG Langan et al. "The role of diluents in electronegative fluorinated gas discharges". In: *Journal of applied physics* 79.8 (1996), pp. 3886–3894.

[63] AA Howling et al. "Frequency effects in silane plasmas for plasma enhanced chemical vapor deposition". In: *Journal of Vacuum Science & Technology A: Vacuum, Surfaces, and Films* 10.4 (1992), pp. 1080–1085.

[64] B Andries, G Ravel, and L Peccoud. "Electrical characterization of radio-frequency parallel-plate capacitively coupled discharges". In: *Journal of Vacuum Science & Technology A: Vacuum, Surfaces, and Films* 7.4 (1989), pp. 2774–2783.

[65] Mark A Sobolewski, JG Langan, and BS Felker. "Electrical optimization of plasma-enhanced chemical vapor deposition chamber cleaning plasmas". In: *Journal of Vacuum Science & Technology B: Microelectronics and Nanometer Structures Processing, Measurement, and Phenomena* 16.1 (1998), pp. 173–182.

[66] N Spiliopoulos, D Mataras, and DE Rapakoulias. "Power dissipation and impedance measurements in radio-frequency discharges". In: *Journal of Vacuum Science & Technology A: Vacuum, Surfaces, and Films* 14.5 (1996), pp. 2757–2765.

[67] M Mohamed Salem, J-F Loiseau, and B Held. "Impedance matching for optimization of power transfer in a capacitively excited RF plasma reactor". In: *The European Physical Journal-Applied Physics* 3.1 (1998), pp. 91–95.

[68] JD Scofield, P Bletzinger, and BN Ganguly. “Oxygen-free dry etching of α-SiC using dilute SF 6: Ar in an asymmetric parallel plate 13.56 MHz discharge”. In: *Applied physics letters* 73.1 (1998), pp. 76–78.

[69] Maolin Long. “Power efficiency oriented optimal design of high density CCP and ICP sources for semiconductor RF plasma processing equipment”. In: *IEEE transactions on plasma science* 34.2 (2006), pp. 443–454.

[70] JK Joshi et al. “Electron series resonance in a magnetized 13.56 MHz symmetric capacitive coupled discharge”. In: *Journal of Applied Physics* 123.11 (2018), p. 113301.

[71] C Beneking. “Power dissipation in capacitively coupled rf discharges”. In: *Journal of applied physics* 68.9 (1990), pp. 4461–4473.

[72] Jay K Joshi, Shantanu K Karkari, and Sunil Kumar. “Effect of Magnetization on Impedance Characteristics of a Capacitive Discharge Using Push-Pull Driven Cylindrical Electrodes”. In: *IEEE Transactions on Plasma Science* 47.12 (2019), pp. 5291–5298.

[73] VA Godiak and OA Popov. “Experimental study of resonant rf discharges”. In: *Fizika Plazmy* 5 (1979), pp. 400–407.

[74] DJ Cooperberg and CK Birdsall. “Series resonance sustained plasmas in a metal bound plasma slab”. In: *Plasma Sources Science and Technology* 7.2 (1998), p. 96.

[75] W.D. Qiu. “Electron series resonance plasma discharges: Unmagnetized and magnetized”. PhD thesis. Berkeley, 2001.

[76] VV Zhurin, HRf Kaufman, and RSf Robinson. “Physics of closed drift thrusters”. In: *Plasma Sources Science and Technology* 8.1 (1999), R1.

[77] Albert Simon. “Ambipolar diffusion in a magnetic field”. In: *Physical Review* 98.2 (1955), p. 317.

[78] Davide Curreli and Francis F Chen. “Cross-field diffusion in low-temperature plasma discharges of finite length”. In: *Plasma Sources Science and Technology* 23.6 (2014), p. 064001.

[79] D Eremin. “Electromagnetic Effects in Capacitively Coupled Plasmas”. In: *arXiv preprint arXiv:1510.02970* (2015).

[80] GD Conway and JA Elliott. “Evidence of Kelvin Helmholtz instabilities in the UMIST linear quadrupole”. In: *Plasma physics and controlled fusion* 29.7 (1987), p. 807.

[81] Christiane Schröder et al. “Mode selective control of drift wave turbulence”. In: *Physical review letters* 86.25 (2001), p. 5711.

[82] KH Burrell. “Effects of E× B velocity shear and magnetic shear on turbulence and transport in magnetic confinement devices”. In: *Physics of Plasmas* 4.5 (1997), pp. 1499–1518.

[83] Jan Gerard Bannenberg. *Design and characteristics of a rotating plasma device.* Tech. rep. Technische Hogeschool, Delft (Netherlands), 1971.

[84] Dirk Van Eester, Kristel Crombé, and Volodymyr Kyrytsya. “Connection coefficients for cold plasma wave propagation near metallic surfaces”. In: *Plasma Physics and Controlled Fusion* 55.5 (2013), p. 055001.

[85] Nobuyuki Asakura, ITPA SOL, and Divertor Topical Group. “Understanding the SOL flow in L-mode plasma on divertor tokamaks, and its influence on the plasma transport”. In: *Journal of nuclear materials* 363 (2007), pp. 41–51.

[86] Y Hayashi et al. “Plasma flow in peripheral region of detached plasma in linear plasma device”. In: *Physics of Plasmas* 23.1 (2016), p. 012511.

[87] H Grote et al. “Comparison of chemical sputtering yields for different graphites at high ion flux densities”. In: *Journal of nuclear materials* 241 (1997), pp. 1152–1155.

[88] Jason A Kenney, Shahid Rauf, and Ken Collins. “Effect of azimuthally asymmetric reactor components on a parallel plate capacitively coupled plasma”. In: *Journal of Applied Physics* 106.10 (2009), p. 103302.

Appendix

M2

Material

A perminvar NiZn ferrite designed for high frequency applications (up to 50 MHz) including broadband transformers, antennas and high frequency, high Q inductors.

Specifications

Property	Unit	Symbol	Standard Test Conditions	Value
Initial Permeability		μ_i	Frequency=10 kHz; B<10 gauss	40 ± 20%
Saturation Flux Density	gauss	B_S	H=20 oersted	≈ 2300
Residual Flux Density	gauss	B_r		≈ 800
Coercive Force	oersted	H_C		≈ 4
Loss Factor	10^{-6}	$\tan\delta/\mu_i$	Frequency=50 MHz; B=1 gauss	≤ 150
Temperature Coefficient of Initial Permeability (20-70°C)	%/°C			≤ 0.05
Volume Resistivity	Ω cm	ρ		≈ 10^7
Curie Temperature	°C	T_C		≥ 450

Note: values are typical and based on measurements of a standard toroid at 25 °C

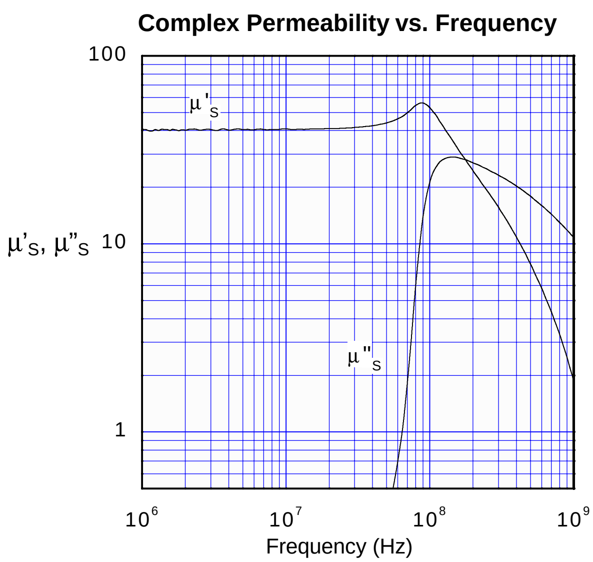

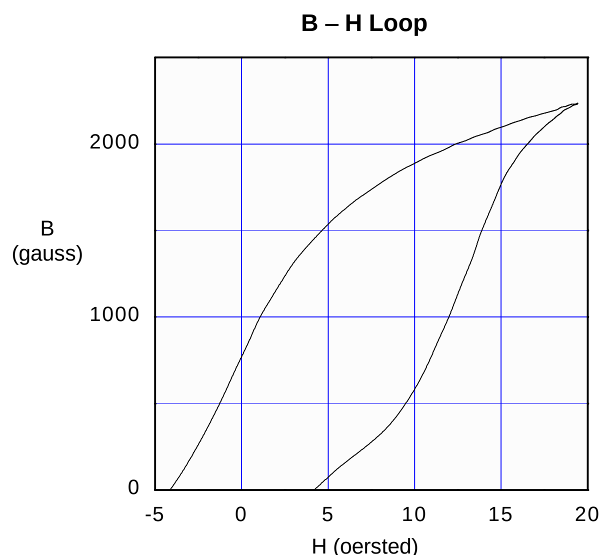

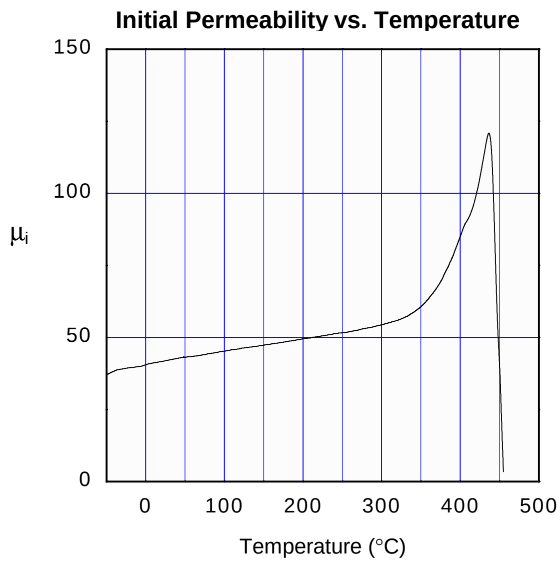

1210 WIN DR.
BETHLEHEM, PA 18017-7061
TEL: 610-867-7600 • FAX: 610-867-0200 • EMAIL: sales@magneticsgroup.com

PASTERNACK®
THE ENGINEER'S RF SOURCE

Flexible RG213 Coax Cable Single Shielded with Black PVC Jacket

TECHNICAL DATA SHEET RG213/U

Configuration

Inner Conductor Material and Plating	Copper
Dielectric Type	PE
Shield Materials	Copper Braid
Jacket Material and Color	PVC, Black

Electrical Specifications

Impedance, Ohms	50
Velocity of Propagation, %	66
Maximum Operating Frequency, MHz	1000
Capacitance, pF/ft [pF/m]	30.8 [101.05]

Electrical Specifications by Frequency

Frequency 1

Frequency, MHz	100
Attenuation, dB/100ft [dB/100m]	2.1 [6.89]

Frequency 2

Frequency, MHz	400
Attenuation, dB/100ft [dB/100m]	4.8 [15.75]

Frequency 3

Frequency, MHz	1000
Attenuation, dB/100ft [dB/100m]	8 [26.25]

Mechanical Specifications

Inner Conductor

Number of Strands	7
Material	Copper
Diameter, in [mm]	0.09 [2.29]

Dielectric:

Type	PE
Diameter, in [mm]	0.285 [7.24]

Shield:

Number of	1
Material 1	Copper Braid
Diameter, in [mm]	0.314 [7.98]

Click the following link (or enter part number in “SEARCH” on website) to obtain additional part information including price, inventory and certifications: Flexible RG213 Coax Cable Single Shielded with Black PVC Jacket RG213/U

Pasternack Enterprises, Inc. • P.O. Box 16759, Irvine, CA 92623
Phone: (866) 727-8376 or (949) 261-1920 • **Fax:** (949) 261-7451
Sales@Pasternack.com • Techsupport@Pasternack.com

PASTERNACK®
THE ENGINEER'S RF SOURCE

Flexible RG213 Coax Cable Single Shielded with Black PVC Jacket

TECHNICAL DATA SHEET RG213/U

Jacket:

Material	PVC
Diameter, in [mm]	0.405 [10.29]
Color	Black
Weight, lbs/ft [Kg/m]	0.115 [0.17]

Compliance Certifications (visit www.Pasternack.com for current document)

RoHS Compliant	
REACH Compliant	06/18/2012

Plotted and Other Data

Notes:
- Values at +25 °C, sea level
- Max. Operating Voltage(VRMS): 5000

Flexible RG213 Coax Cable Single Shielded with Black PVC Jacket from Pasternack Enterprises has same day shipment for domestic and International orders. Our RF, microwave and millimeter wave products maintain a 99% availability and are part of the broadest selection in the industry.

Click the following link (or enter part number in "SEARCH" on website) to obtain additional part information including price, inventory and certifications: Flexible RG213 Coax Cable Single Shielded with Black PVC Jacket RG213/U

URL: http://www.pasternack.com/flexible-0.405-rg213-50-ohm-coax-cable-pvc-jacket-rg213-u-p.aspx

The information contained in this document is accurate to the best of our knowledge and representative of the part described herein. It may be necessary to make modifications to the part and/or the documentation of the part, in order to implement improvements. Pasternack reserves the right to make such changes as required. Unless otherwise stated, all specifications are nominal. Pasternack does not make any representation or warranty regarding the suitability of the part described herein for any particular purpose, and Pasternack does not assume any liability arising out of the use of any part or documentation.

Pasternack Enterprises, Inc. • P.O. Box 16759, Irvine, CA 92623
Phone: (866) 727-8376 or (949) 261-1920 • **Fax:** (949) 261-7451
Sales@Pasternack.com • Techsupport@Pasternack.com

RG213/U CAD Drawing

Flexible RG213 Coax Cable Single Shielded with Black PVC Jacket